

UTILIZING SMART INVERTER CAPABILITIES FOR MANAGEMENT OF HIGH
PENETRATION RENEWABLE DISTRIBUTED GENERATION INTEGRATION IN
ACTIVE DISTRIBUTION NETWORKS

by

Manohar Chamana

A dissertation submitted to the faculty of
The University of North Carolina at Charlotte
in partial fulfillment of the requirements
for the degree of Doctor of Philosophy in
Electrical Engineering

Charlotte

2016

Approved by:

Dr. Badrul H. Chowdhury

Dr. Babak Parkhideh

Dr. Valentina Cecchi

Dr. Brett Q. Tempest

©2016
Manohar Chamana
ALL RIGHTS RESERVED

ABSTRACT

MANOHAR CHAMANA. Utilizing smart inverter capabilities for management of high penetration renewable distributed generation integration in active distribution networks.
(Under the direction of DR. BADRUL H. CHOWDHURY)

With a strong indication of high renewable distributed generation (DG) penetration increase in the near future, distribution system operators (DSOs) are burdened with challenges to manage their operation while also trying to solve the power quality issues emerging due to reverse power flow and their stochastic behavior. This work focuses on both distributed control as well as centralized control techniques while utilizing the capability of the smart inverter that controls the power flow as well as provides power quality services. In order to signify the importance of smart inverter capability while integrating renewable DGs on active distribution networks, applications are proposed for distribution networks that are either connected to the main grid or operates as a standalone microgrid that requires both power quality as well as power flow control to perform economic operation.

This dissertation work begins with presenting the negative impacts of high scale distributed generation on the grid specifically during high ramp rate events. Initial results show the inability of either the conventional voltage regulators as well as the dynamic reactive power support from a smart inverter to maintain node voltages within a desired band. A passive ramp rate control is presented that depends solely on the battery state of charge (SoC) and does not take into consideration the system modeling. Next, a distributed voltage control (DVC) scheme is proposed on the same active distribution network (ADN) in the presence of high penetration photovoltaic (PV) generation to

mitigate high ramp-rate issues actively based on a sensitivity tool strategy. Multiple voltage regulating devices, are coordinated in various ways based on a distributed coordination management scheme. This work presents the relationship of the active and reactive power outputs of a PV plant in the presence of the conventional voltage regulating devices, and proposes a distributed control strategy to coordinate the SVRs with the PV inverter's capability to improve power quality. In order to plan the PV penetration ahead of time, a zone based multistage time graded operation of the cascaded load-tap changing (LTC) transformers and capacitor banks (CBs) is developed. The objective of the proposed centralized optimization algorithm is to regulate the voltage in a medium voltage (MV) unbalanced distribution system while trying to relax the tap operations of voltage regulators that are cascaded in series, and thereby, minimize the curtailment of PV output when necessary. A technique for changing Mixed-integer nonlinear programming (MINLP) to nonlinear programming (NLP) and then to binary-MINLP optimization is suggested to meet the different objectives at successive stages. The first stage is associated with the on-load tap changing (OLTC) transformer taps and capacitor bank operations. The second, third and fourth stages deal with the step voltage regulator (SVR) operations in their respective zones. A week long simulation was performed for various scenarios of PV and load profile variations.

Finally a microgrid system is tested with a hybrid DG/battery system to prove its ability to dispatch based on set-points from a secondary level. A multi-stage power regulation scheme for different Distributed Energy Resources (DERs) in a standalone microgrid is proposed. During the on-peak period for islanded mode, a two stage operation based on cost optimization and frequency regulation is proposed. In the

standalone mode, a microgrid energy management system (M-EMS) aims to sustain the loads while performing an economic generation scheduling based on an optimization control strategy with the help of several droop enabled sources that includes two hybrid distributed generator (DG)/battery systems. In addition when the load demand is low, a multi-objective optimization strategy is proposed to charge the batteries back to their nominal values while the other dispatchable sources operate in droop mode with economical operation. Numerical results from the 33 bus distribution system, when operated as a microgrid, show the effectiveness of the strategy.

ACKNOWLEDGMENTS

I express my sincere gratitude to my advisor Dr. Badrul H. Chowdhury for his guidance, encouragement, and constant support throughout my graduate studies and providing an environment to pursue my research interests. I am grateful to the Electrical and Computer Engineering (ECE) department and Energy Production and Infrastructure Center (EPIC) at UNC Charlotte for its continued financial support through the duration of this work. I am also grateful to my graduate supervisory committee, comprising of Dr. Babak Parkhideh, Dr. Valentina Cecchi and Dr. Brett Tempest for their time and insightful comments to improve my work. I also take this opportunity to thank the faculty of the power engineering program at EPIC, UNC Charlotte, for their many contributions towards my comprehensive growth over the period of my education here. I also appreciate the help from my lab mates and friends throughout my doctoral studies. I am grateful for my family, my parents Capt. (Retired) C. V. M Rao and Mrs. Ajanta Rao.

TABLE OF CONTENTS

LIST OF FIGURES	xi
LIST OF TABLES	xv
CHAPTER 1 : MOTIVATION AND PROBLEM OVERVIEW	1
1.1. Motivation	1
1.2. Effect of DGs on Active Distribution Networks (ADNs)	2
1.3. Smart Inverter Capability	5
1.3.1. Reactive Power Capability	6
1.3.2. Active Power Control/Curtailment	8
1.3.3. Storage Integration with Bi-Directional Charging/Discharging Capabilities	9
1.3.4. Interaction between Active and Reactive Power Support	11
1.3.5. Price-Based Operation of DERs	12
1.4. Different Control Strategies to Accommodate DG Penetration	13
1.5. Microgrid: Hierarchical Control Levels	16
1.5.1. Challenges to Meet Reliable and Economical Operation	18
1.6. Case Studies Performed on DG Penetration that Motivates this Research	19
1.6.1. Colorado State University (CSU) Foothills Campus, Fort Collins, Colorado	19
1.6.2. 2 MW Plant in Fontana, California	20
1.6.3. Hybrid Standalone Microgrid System in Isle of Eigg (Scotland)	21
1.7. Solutions and Dissertation Layout	22

	viii
CHAPTER 2 : DYNAMIC RAMP RATE CONTROL BASED ON LOCAL CONTROL STRATEGIES FOR VOLTAGE REGULATION IN DISTRIBUTION SYSTEMS WITH HIGH PENETRATION PHOTOVOLTAIC PLANT	24
2.1. Introduction	24
2.2. Communication-Free Ramp Rate Control Based on Local Measurements	25
2.3. Distribution Feeder	30
2.4. Case Studies	31
2.4.1. Without Ramp Rate Control	32
2.4.2. With Ramp Rate Control	32
2.5. Summary	35
CHAPTER 3 : DISTRIBUTED CONTROL OF VOLTAGE REGULATING DEVICES IN THE PRESENCE OF HIGH PV PENETRATION TO MITIGATE RAMP-RATE ISSUES	37
3.1. Introduction	37
3.2. Literature Review	38
3.3. Theory and Proposed Solution	42
3.3.1. Power Sensitivity Calculation	42
3.3.2. SVR Tap Operation	46
3.3.3. Capacitor Bank Reactive Power Control	50
3.3.4. Inverter Reactive Power Control	51
3.3.5. Inverter Active Power Control	53
3.4. Overall Control and Coordination Scheme	59
3.5. Case Studies	63
3.6. Summary	70

	ix
CHAPTER 4 : OPTIMAL VOLTAGE REGULATION OF DISTRIBUTION NETWORKS WITH CASCADED VOLTAGE REGULATORS IN THE PRESENCE OF HIGH PV PENETRATION	73
4.1. Introduction	73
4.2. Literature Review	74
4.3. Theory and Proposed Solution	77
4.3.1. Objective Functions	77
4.3.2. Inequality and Equality Constraints	79
4.3.3. Solution Methodology	84
4.4. Case Studies	88
4.5. Summary	92
CHAPTER 5 : HYBRID SYSTEM OPERATION IN MICROGRID	94
5.1. Introduction	94
5.2. Droop Controller Concept	96
5.3. Controller Design	100
5.3.1. PV Array Control	100
5.3.2. Inverter Side Control	101
5.3.3. Battery Side Control	103
5.4. Microgrid Implementation	105
5.5. Results	106
5.5.1. BESS Discharging Case	106
5.6. Summary	110
CHAPTER 6 : MULTI-STAGE OPERATION OF DISTRIBUTED ENERGY RESOURCES IN A STANDALONE MICROGRID CONSIDERING COST AND FREQUENCY DEVIATION MINIMIZATION	112

	x
6.1. Introduction	112
6.2. Control Hierarchy for the Microgrid Test System	114
6.3. Cost of Generation and Operation of DERs	115
6.4. Literature Review	116
6.5. Theory and Proposed Solution	117
6.5.1. Islanded Operation	118
6.5.2. Modified Droop Operation	119
6.6. Microgrid Operation Constraints	120
6.6.1. Droop Constraints	121
6.6.2. Battery Constraints	124
6.6.3. Power Flow	127
6.7. Multi-Period Optimization Procedure	128
6.7.1. On-Peak Period Regulation	128
6.7.2. Off-Peak Period Regulation	129
6.8. Case Studies	130
6.8.1. On-Peak Period Operation	133
6.8.2. Off-Peak Period Operation	137
6.9. Summary	141
CHAPTER 7 : FINAL CONCLUSIONS, CONTRIBUTIONS AND FUTURE WORK	143
7.1. Concluding Remarks	143
7.2. Directions for Future Work	146
REFERENCES	148

LIST OF FIGURES

FIGURE 1.1: (a) Two bus system example with PV connected (b) Forward and reverse power flow effect on voltages.	3
FIGURE 1.2: Reverse power flow effect on voltage regulators [2].	4
FIGURE 1.3: Impact of high ramp-rate events on the system voltage [3].	5
FIGURE 1.4: Reactive power capability curve of an inverter.	7
FIGURE 1.5: Desired Volt-VAr behavior [4].	8
FIGURE 1.6: VAr output varying inversely with watt output [4].	8
FIGURE 1.7: Maximum watts vs. voltage [4].	9
FIGURE 1.8: Maximum watts absorbed vs. voltage [4].	11
FIGURE 1.9: Inverter output with PV panel output (a) 100% and (b) 80% [4].	12
FIGURE 1.10: Different control architectures	15
FIGURE 1.11: Hierarchical control levels: primary control, secondary control, and tertiary control.	16
FIGURE 1.12: Simplified circuit diagram of the Fontana, California [10].	20
FIGURE 1.13: (a) Standalone microgrid components from top left: PV arrays, wind turbines, battery bank, diesel generator, inverters system, 6 kW hydro turbine, (b) Standalone microgrid system configuration [11].	22
FIGURE 2.1: Effect of cloud movement and sun blocking on a solar panel.	25
FIGURE 2.2: Sliding window with width Δt .	27
FIGURE 2.3: Dynamic ramp threshold determination based on current SOC levels.	28
FIGURE 2.4: Ramp rate control algorithm	29
FIGURE 2.5: Reduced MV distribution feeder with PV as DG	31
FIGURE 2.6: Ramp-up event: solar irradiance during sunrise and ramp-down even due to cloud covering	31

FIGURE 2.7: (a) PV active and reactive power, (b) PV node rms voltage	32
FIGURE 2.8: (a) DVC reactive power output, (b) DVC node rms voltage	33
FIGURE 2.9: (a) Phase tap ratios in pu for SVR 1 (b) Phase tap ratios in pu for SVR 3.	33
FIGURE 2.10: (a) PV active and reactive power, (b) Battery power, (c) Battery SoC and (d) PV node rms voltage	34
FIGURE 2.11: (a) DVC reactive power output, (b) DVC node rms voltage	35
FIGURE 2.12: (a) Phase tap ratios in pu for SVR 1 (b) Phase tap ratios in pu for SVR 3	35
FIGURE 3.1: 3-phase line segment model	43
FIGURE 3.2: Voltage-power sensitivity calculation	46
FIGURE 3.3: Tap operation condition (a) Voltage with bandwidth consideration (b) Activate signal activation (c) Actuation trigger time (d) Tap operation with time delay.	48
FIGURE 3.4: Closed delta-connected regulators [28].	50
FIGURE 3.5: Capacitor bank model [28].	51
FIGURE 3.6: Reactive power capability of the inverter.	53
FIGURE. 3.7: Voltage dependence on active power output at the PV bus (a) Voltage (b) PV active power output.	55
FIGURE. 3.8: Scaling factor estimation based on SoC of battery and supercapacitor.	57
FIGURE 3.9: (a) Voltage-based droop control for inverter interfaced source (b) Voltage-based droop control for synchronous based generators.	59
FIGURE. 3.10: Coordinated distributed control between SVR and the PV system for voltage control.	61
FIGURE 3.11: Flowchart of DVC	63
FIGURE 3.12: MV feeder located in a California utility.	65
FIGURE 3.13: Cumulative load factor variation with time.	65

FIGURE 3.14: Feeder results for Case I (a) PV system power outputs, (b) PV terminals voltage, (c) SCB units switch on/off status, (d) SVR 2 tap positions, (e) SVR 3 tap positions and (f) SVR 4 tap positions.	67
FIGURE 3.15: Feeder results for Case II (a) PV system power outputs, (b) PV terminals voltage, (c) SCB units switch on/off status, (d) SVR 2 tap positions, (e) SVR 3 tap positions and (f) SVR 4 tap positions.	68
FIGURE 3.16: Feeder results for Case III (a) PV system power outputs, (b) Battery output, (c) Battery SoC, (d) PV terminals voltage, (e) SCB units switch on/off status, (f) SVR 2 tap positions, (g) SVR 3 tap positions and (h) SVR 4 tap positions.	70
FIGURE 4.1: Three-phase line segment model [28].	80
FIGURE 4.2: The LTC conventional local controller.	83
FIGURE 4.3: Conversion of one optimization form to another.	86
FIGURE 4.4: Multistage coordination scheme of the proposed voltage regulation.	87
FIGURE 4.5: MV feeder located in a California utility separated into 4 zones based on SVR target nodes.	88
FIGURE 4.6: (a) Available and extracted PV plant power, (b) Reactive power support by PV plant, (c) Load profiles by class.	90
FIGURE 4.7: (a-e) Conventional voltage regulators taps/switch operation.	91
FIGURE 4.8: (a-e) Regulator target bus voltage profiles.	91
FIGURE 5.1: Power flow study circuit	97
FIGURE 5.2: Voltage and frequency droops based on inductive network mode.	99
FIGURE 5.3: Inverter side control system.	103
FIGURE 5.4: Battery side control system.	104
FIGURE 5.5: Microgrid architecture.	105
FIGURE 5.6: Active power outputs of 4 inverters.	107
FIGURE 5.7: Reactive power outputs of 4 inverters.	108

FIGURE 5.8: (a) PV systems internal measurements during battery discharging (b) BESS charging condition and (c) DC bus voltages.	108
FIGURE 5.9: PV/BESS system measurement during battery charging condition	110
FIGURE 6.1: (a) Voltage-based droop control for inverter interfaced source (b) Voltage-based droop control for synchronous based generators.	120
FIGURE 6.2: On-peak optimization routine flowchart.	129
FIGURE 6.3: Off-peak optimization routine flowchart.	130
FIGURE 6.4: 33-bus test system operating as a microgrid in both grid-connected and islanded mode (Data about system loads and line impedances can be found in [74]).	132
FIGURE 6.5: (a) Solar and wind source profiles, (b) Load profiles.	133
FIGURE 6.6: On-peak period operation (a) Active power outputs (b) Voltages at the source nodes (c) PV and wind maximum power point outputs (d) SoCs of the batteries (e) Reactive power outputs and (f) Frequency comparison of uncontrolled and controlled operation.	137
FIGURE 6.7: Off-peak period operation (a) Active power outputs (b) Voltages at the source nodes (c) PV and wind maximum power point outputs (d) SoCs of the batteries (e) Reactive power outputs and (f) Frequency comparison of uncontrolled and controlled operation.	141

LIST OF TABLES

TABLE 1.1: Differentiating the three different control techniques.	15
TABLE 1.2: State of the art of Primary and Secondary control in microgrids	17
TABLE 3.1: Total number of SVRs taps operations for case I	67
TABLE 3.2: Total number of SVRs taps operations for case II	68
TABLE 3.3: Total number of SVRs taps operations for case III	70
TABLE 4.1: Subsystem specifications for the PV plant	92
TABLE 4.2: Daily performance parameter comparison	92
TABLE 6.1: Droop-Controlled DDGs: locations, ratings and cost of operation	133
TABLE 6.2: Droop-Controlled RDG/battery hybrid systems: locations, type, ratings, and battery unit cost.	133

CHAPTER 1 : MOTIVATION AND PROBLEM OVERVIEW

1.1. Motivation

The focus of the dissertation is to work towards solving a few negative effects and accommodate high renewable distributed generators (DGs) integration on distribution systems and microgrids. A few management techniques by utilizing the smart inverter capabilities along with conventional regulating devices is suggested in this work. Typically photovoltaics (PVs) are being utilized as distributed generators that require an interfacing medium to convert DC to AC (50/60 Hz). In the US, a number of utilities have implemented and have plans to further increase their renewable footprint to meet the aggressive renewable portfolio standard (RPS) targets mandated by their respective state governments to reduce CO₂ emissions from fossil fuels based generators. In return, the utilities receive benefits in the form of feed-in tariffs, investment tax credits, and green certificates, among others. Apart from the direct connection to the grid where the substation of the feeder acts as a voltage source and the DG behaves as a current source, they could participate in the power sharing control strategy when connected in a microgrid during islanded period. Microgrid has been defined as a collection of distributed energy resources (DERs), which includes both DGs and storage energy resources along with loads contained within a physical boundary to operate either in grid-connected or islanded mode operation. Microgrids could be formed within an existing

feeder by demarcating a geographical portion, which consists of DERs that have the ability to act as a source of frequency and voltage.

1.2. Effect of DGs on Active Distribution Networks (ADNs)

The stochastic/intermittent nature of high penetration DGs on the distribution systems causes some undesirable effects. DGs can cause a voltage increase or decrease along the feeder depending on the DG type, control method, its delivered power, feeder parameters and loading conditions. The issue with renewable DGs, specifically photovoltaic (PV) sources are their highly unpredictable output due to weather changes caused by cloud movement, temperature changes, shading, PV panel soiling and performance deterioration with time [1]. High penetration of DG cause increased switching operations of line regulators, tap changers, switched capacitor banks which eventually reduces their lifetime. Sudden changes in real power generation from DGs cause flicker due to rapidly fluctuating voltage. It causes a transient voltage changes on a sudden trip of PV generation system, especially if the system is actively participating in voltage regulation. Harmonics generated by the PV inverters are also a concern along with resonant interactions of inverters with the distribution system. Conductor and equipment get loaded due to reverse power flows resulting from the introduction of high DG penetration in the distribution system.

In the case of a microgrid with many inverter based DGs, the lack of inertia in the grid is high due to a lack of rotating mass which is usually coupled with the frequency of the grid. This would cause issues of high-frequency excursion with a change in load, as the system is unable to arrest the high-frequency change for a short period of time.

The distribution operators are concerned with utilizing DGs in the voltage regulating services as they conflict with the existing conventional voltage regulating devices to regulate the voltage at the same bus which could lead to maloperation. DGs inject power in the reverse direction, which can cause PV bus voltages, V_{PV} to go above ANSI C84.1 standards ($0.95 < V_{bus} < 1.05$). Voltage drop along feeder as shown in Figure 1.1(a) is given by (1.1).

$$V_{drop} \approx I_R \cdot R + I_X \cdot X \quad (1.1)$$

where V_{drop} is the voltage drop along the feeder, R is the line resistance, X is the line reactance, I_R is the line current due to active power flow (negative for reverse power flow) and I_X is the line current due to reactive power (negative for capacitive power flow). As shown in the reverse power flow causes V_{drop} to change direction hence increasing the length of the vector, V_{PV} above the ANSI C84.1 standards. It gets worse when X/R ratios of cable lines in the feeder are low. The vector representation of forward and reverse power flow is shown in Figure 1.1(b).

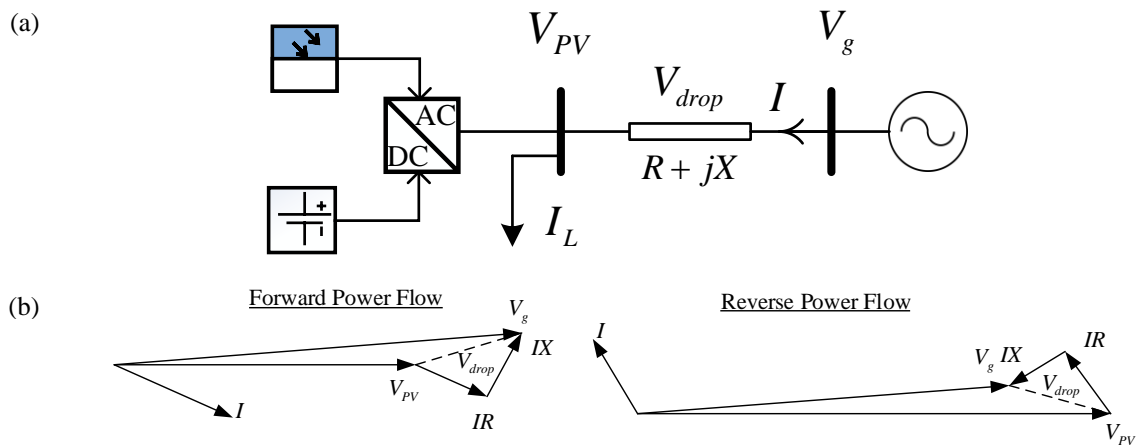


Figure 1.1: (a) Two bus system example with PV connected (b) Forward and reverse power flow effect on voltages.

High reverse Power flow causes the bidirectional regulator to regulate in the opposite direction. DGs (especially PV) cause unwanted interaction with regulators (SVR, OLTC, capacitor banks). A DG that is present in the downstream as shown in Figure 1.2, causes the regulator to assume that the source direction has changed and begins to regulate the voltage at the substation end, hence causing the tap to change in the opposite steps than expected which leads to raise the voltage at the DG end much higher. Feeders with high PV penetration require a tool to use a directional setting for bidirectional regulators depending on the direction of current flow.

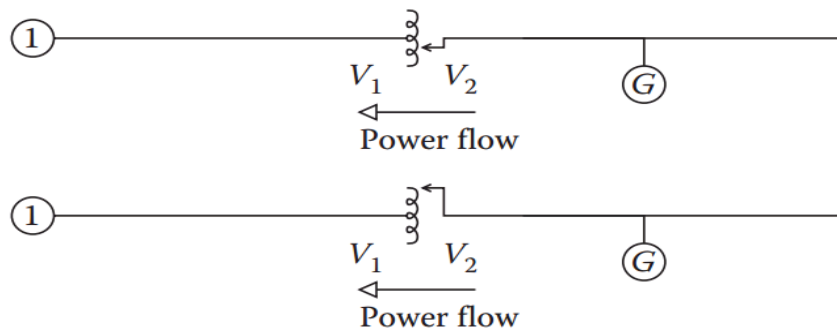


Figure 1.2: Reverse power flow effect on voltage regulators [2].

Measurements of PV output at Fontana in California show that there were around 37 severe events (higher than 50% of PV system rated output per minute) per year with the most severe one at 2.20 MW per minute, or 75% of the system's rated output caused by a departing cloud. Although the passing of clouds causes severe fluctuations in the PV output, the sunlight intensity change is not strong enough to cause severe flicker. Cloud passing may cause rapid variations of voltage, hence causing variations in lighting and interrupts operation of electronics. Figure 1.3 shows real field data of voltage changes due to changes in PV power output during ram-rate events.

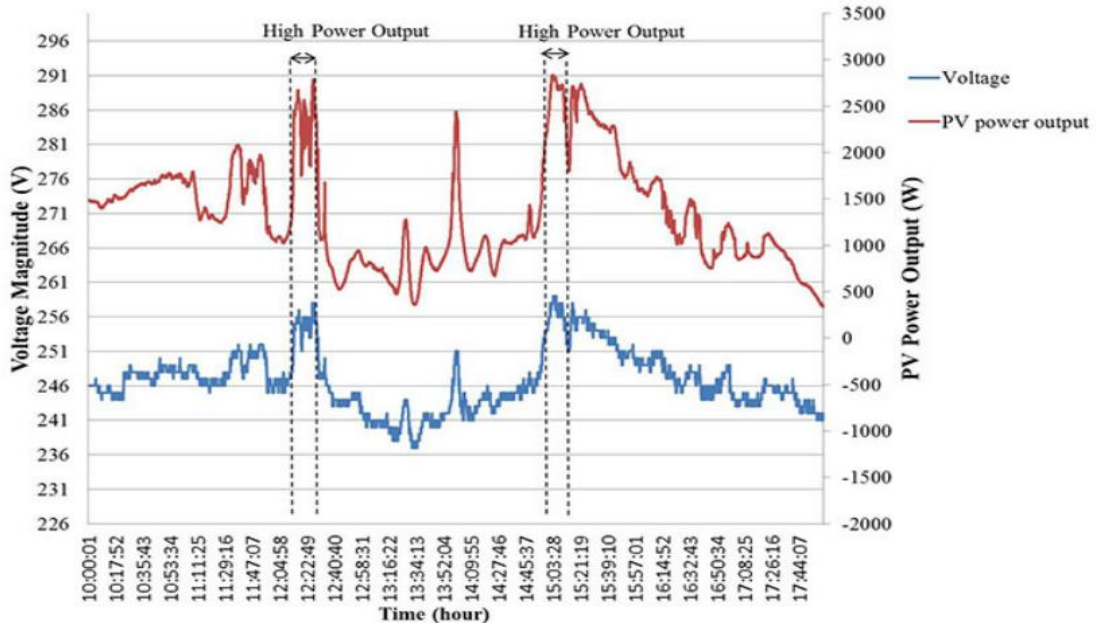


Figure 1.3: Impact of high ramp-rate events on the system voltage [3].

1.3. Smart Inverter Capability

Nowadays voltage regulation by DGs is permissible if a mutual agreement between the utility and DG owner exists [4]. In order to do so, the smart inverter capabilities of DGs must be applied so as to modify the operation needed to operate in a distribution system. The inverter provides flexibility when integrating renewables into the grid as the output can be modified/regulated through this medium. When integrating DGs through inverters certain standards need to be considered that are dictated by the IEEE Std. 1547. Though conservative, these standards need to be further modified to accommodate high scale penetration of DGs while providing ancillary services to the grid. Inverters have the capability to operate in islanded mode or islanded mode to support loads within a territory, or may be tied to the grid as a current source by operating at its maximum power point (MPP) and supply the loads in the vicinity. A DG could be tied to an energy storage device, such as a battery to store energy for a later use or supply power in order to meet demand when DG output is low [4].

1.3.1. Reactive Power Capability

Inverters have the capability to provide dynamic reactive power support similar to synchronous machines (within a cycle), to voltage variations and transient events supports caused by short-circuits, switching surges etc. The unique characteristic of utilizing inverters for reactive power support is its fast dynamic response in sub-seconds scale to meet various requirements. Reactive power support can be used to mitigate the voltage rise during high PV active power output and low load conditions. During this period the inverter needs to absorb reactive power to mitigate the overvoltage conditions. Similarly, when the PV output is low or nil and loads are high this could lead to low voltage conditions which might require the inverter to supply reactive power. Reactive power support during a microgrid islanding operation becomes essential as the voltage is regulated based on a Voltage vs Reactive Power (V/Q) or Voltage vs Active Power (V/P) droop curve to sustain the loads. Reactive power support from DGs is also useful for reducing losses as reactive power support helps in reducing the active power flow in the grid. Figure 1.4, shows the reactive power capability based on a specific active power output level. Reactive power output depends on the nominal apparent power capability of an inverter. Reactive power supply or absorption could be increased by increasing the size of the inverter which has implication on the cost of the inverter. If the size of the inverter is fixed and nearer to the rated output of the DG source then reactive power output depends much on the active power flow through the inverter.

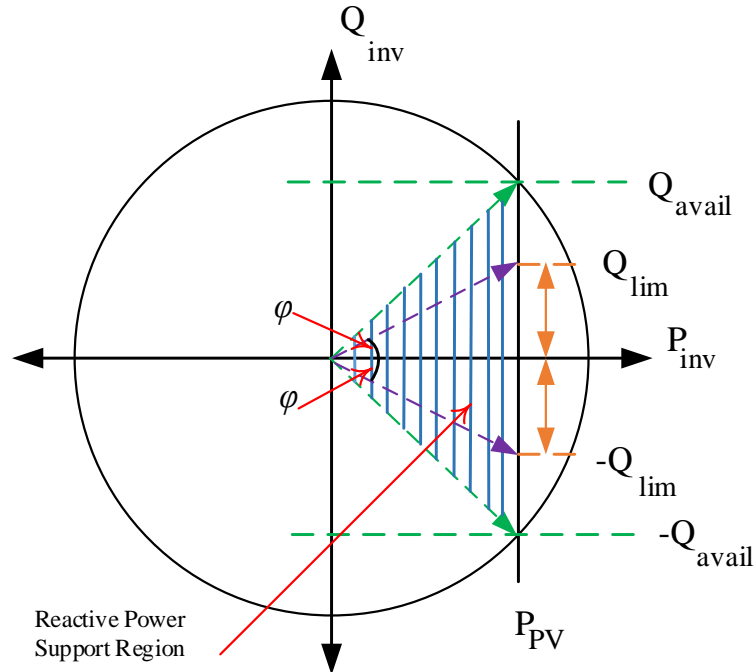


Figure 1.4: Reactive power capability curve of an inverter.

Intelligent Volt-VAr function: This function aids in providing VAr output in response to the local service voltage. Figure 1.5 shows a piece-wise linear curve of the desired Volt-VAr behavior. For a certain voltage bandwidth, no reactive power output is desired which is also known as voltage dead-band as it is within a safe voltage range. For a given % voltage change, a proportion % reactive power is either supplied or absorbed. After a certain voltage point, the reactive power output gets saturated and supplies the maximum VAr.

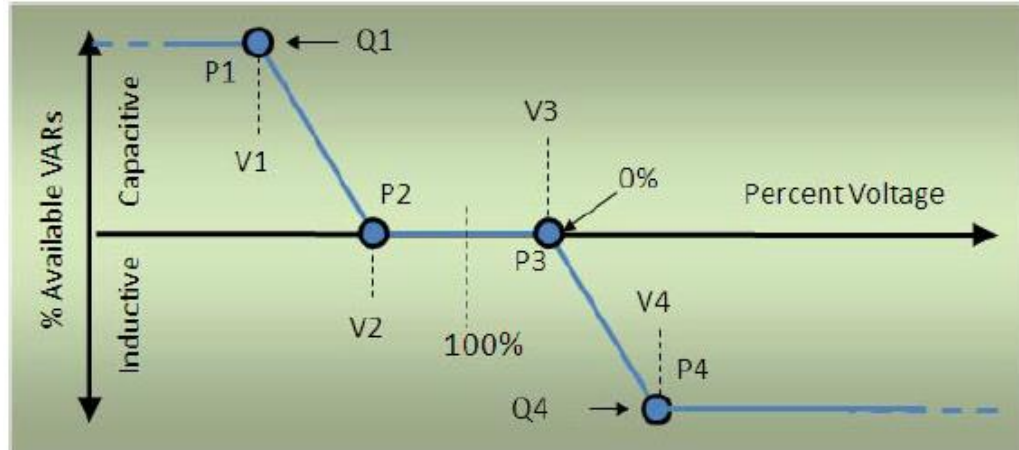


Figure 1.5: Desired Volt-VAR behavior [4].

Figure 1.6 shows the available VARs for an inverter for the Volt-VAR settings without compromising the active power output which takes precedence. When the irradiance is high the reactive power capability of the inverter reduces which effects the capability of VARs to aid in the voltage support.

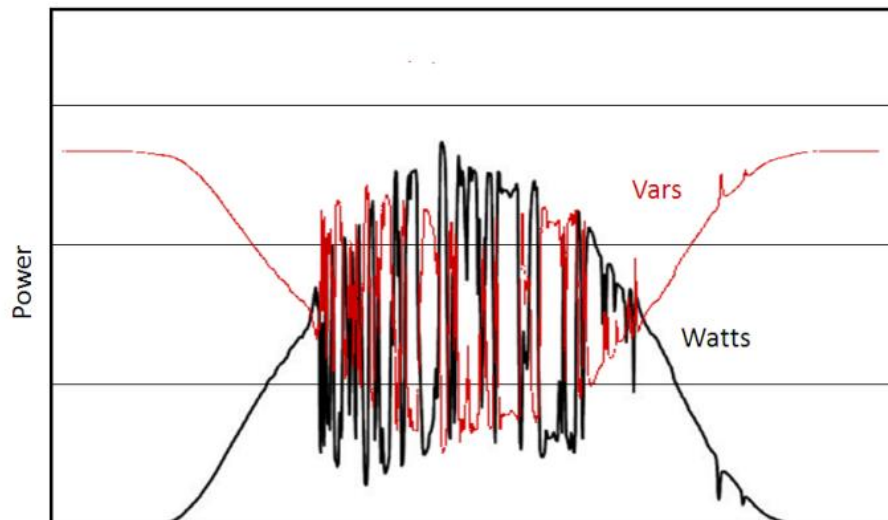


Figure 1.6: VAR output varying inversely with watt output [4].

1.3.2. Active Power Control/Curtailment

Active power control is a feature of an inverter to react to different situations to either control the active power based on frequency or voltage control. In the case of high PV penetration to a strong grid, overvoltage is a common phenomenon as the reverse power

flow might cause the voltage to drop high enough in the opposite direction to cause the voltage to drift above the ANSI standards. In the case of a microgrid when the inverter is now a source of frequency in the islanded grid, the frequency is regulated based on a frequency vs active power (f/P) or frequency vs reactive power (f/Q) droop curve.

With high PV penetration on the distribution side of the grid, the voltages are driven to high levels caused due to lighter loading during certain times and line parameters that are more resistive in nature than inductive. Figure 1.7 shows a piece-wise linear curve that sets an upper limit on active power output from an inverter as a function of the local bus voltage. As the voltages start increasing due to high active power output, a proportional decrease in active power output is set-up so as to counter the high rise in voltage at the local node.

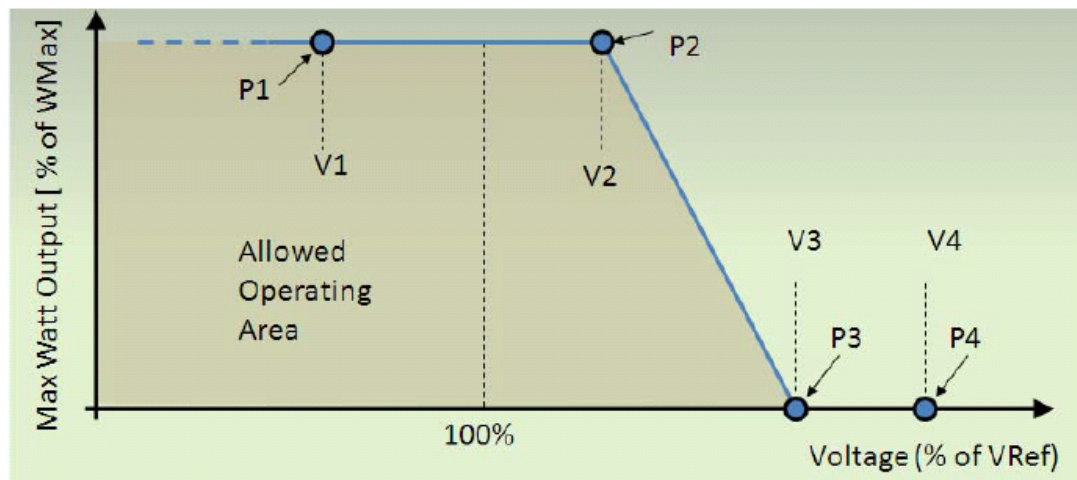


Figure 1.7: Maximum watts vs. voltage [4].

1.3.3. Storage Integration with Bi-Directional Charging/Discharging Capabilities

Current energy storage devices used in the grid are batteries, flywheels, ultra-capacitors and superconducting energy storage systems. To solve the issues caused by intermittent DGs, batteries and ultra-capacitors are found to be reliable due their fast dynamic response. Batteries could be integrated with DGs at the DC link of the inverter,

at the PV integration terminals with a separate inverter or at another point in the distribution grid to solve the issues arising from DG integration. Stationary storage devices are made up of different chemistries and have different depths of discharge. Care needs to be taken when dealing with high utilization of batteries/increased number of cycles, as it reduces their lifetime. Energy Storage System (ESS) needs to be utilized both conservatively and optimally to maximize their benefits. Batteries could be charged by either the DG sources or from the grid. Ultra-capacitors are useful in solving issues of DGs that require rapid response to solve issues arising from cloud transient movement for PV and wind gusts in the case of wind turbines by facilitating power ramping. Batteries have found to store high amounts of energy but are incapable of meeting high power need for less time, which makes them useful to aid in frequency/voltage regulation.

When applying storage devices to curtail the active power or in other words absorb active power by utilizing a storage device a Volt-Watt function curve can be used as shown in Figure 1.8.

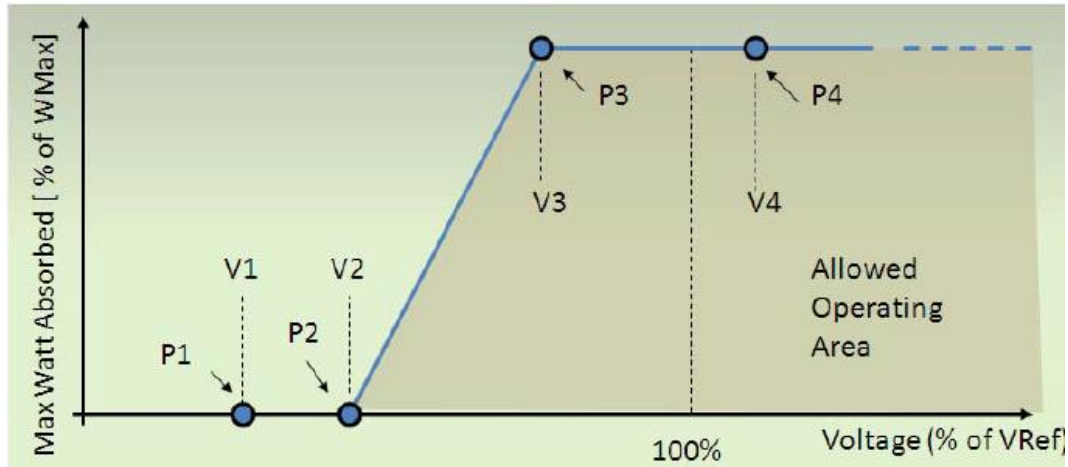


Figure 1.8: Maximum watts absorbed vs. voltage [4].

1.3.4. Interaction between Active and Reactive Power Support

Both Volt-VAr and Watt-Volt functions can be used, to mitigate voltage rises. An inverter is limited by the VA capacity and as active power is given higher priority as soon as voltage increased beyond a limit the active power output can be reduced making more VAr capability to be available to implement the Volt-VAr function and produce VArS even at conditions when the PV is able to produce active power to the full potential of an inverter. Figure 1.9 shows different settings for Volt-VAr and Volt-Watt Modes. For (a) when the active power output is equal to VA capacity of the inverter it cannot support the VAr output but as the voltage increases beyond a limit, the active power is decreased giving the ability to regulate voltage by reactive power support. Similarly for (b) if the active power is limited to 80% of the VA capacity of the inverter, it allows a maximum of 60% reactive power support from the inverter to regulate the voltage until the active power reduces to a point from where the VAr capability increases to 100%. For both cases as the voltage is beyond 105%, it causes the active power to fall also increasing the VAr capability of the inverter.

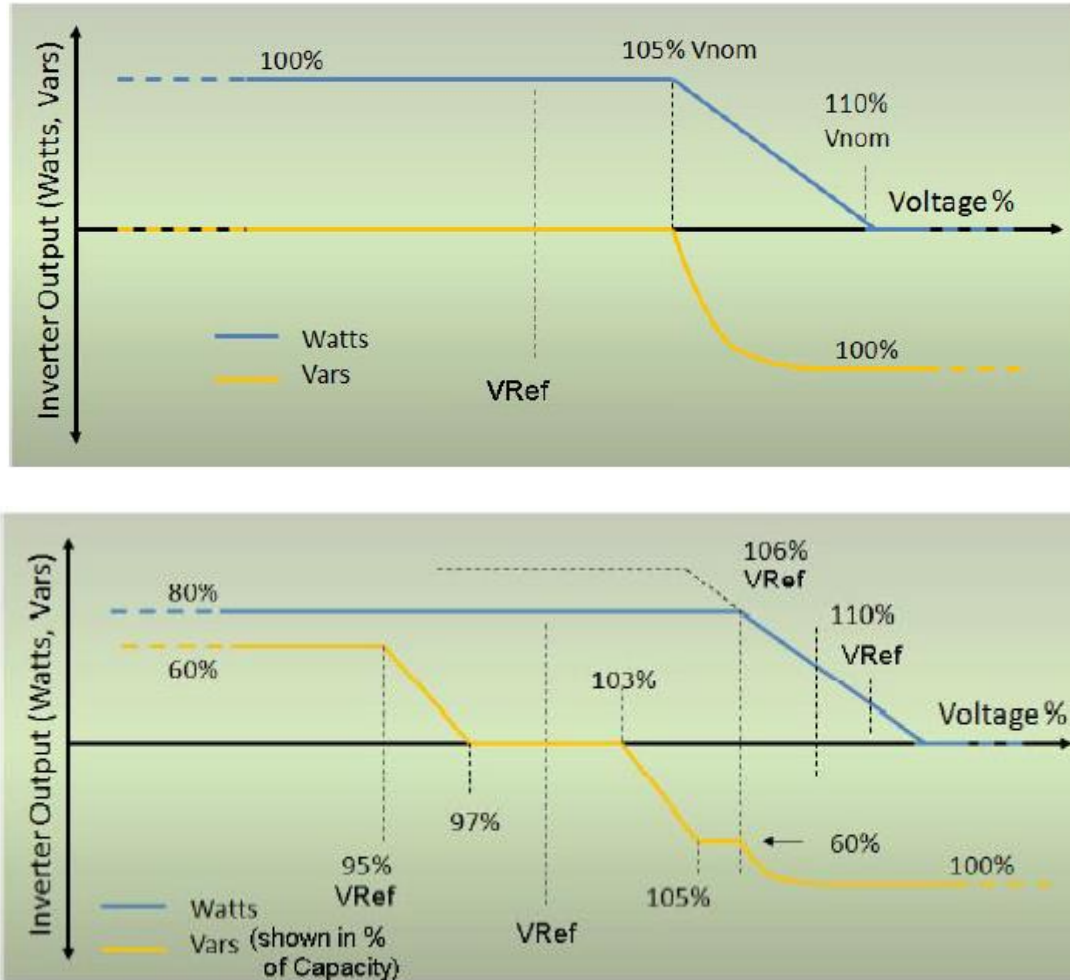


Figure 1.9: Inverter output with PV panel output (a) 100% and (b) 80% [4].

1.3.5. Price-Based Operation of DERs

For the utility owned DERs cost of operation is important while dispatching them for maximizing the profits. The renewable DGs have no fuel cost but covers capital costs, fixed and variable operations and maintenance (O&M) costs, financing costs, and an assumed utilization rate for each renewable type based on environmental conditions. Levelized cost of electricity (LCOE) is a measure to compare the different generators based on the ratio of the average total cost of installation and operation to the total power output over its lifetime. Recent studies have found that the price of rooftop PV is falling as low as 4 cents/kWh, utility-scale solar to around the same level, and solar thermal with

storage to as low as 6.4 cents/kWh, assuming that the capital costs were 8%, which is a major factor in bringing down the price of PV. When a battery is connected in parallel with the DG, a smart inverter has the ability to respond to the price signals by either charging or discharging to control the active power output. Battery energy storage is expensive and not cost competitive which hinders its large scale implementation but it is estimated that the “LCOE” of the future generation mature battery technologies would decline quickly with costs going as low as 40 % by 2017 due to reduction in capital costs, operation and maintenance cost and improved efficiency [5].

1.4. Different Control Strategies to Accommodate DG Penetration

In order to handle overvoltage issues due to high PV penetration voltage regulation by regulating devices such as capacitor bank, step voltage regulators, OLTC, dynamic VAR compensators are required at various points, especially on long feeders. To accommodate high DG generators, they must be allowed/required to participate in voltage regulation automatically, or on the basis of reactive power dispatch or scheduling. If autonomous local automatic voltage control is allowed, the stable operation could be expected when multiple PV generators are involved on the same feeder.

Without proper coordination there is an unwanted interaction between the voltage regulators and fluctuating DG that could be avoided by increasing the bandwidth settings of the regulator and increasing the time delay of tap changes. In literature and practice, quite a number of strategies have been introduced to deal with the integration of DG into the distribution grid. Broadly they can be categorized into centralized and decentralized control. Again, as the DGs are operated differently when tied either as a current or a voltage source their control strategies in the distribution system varies. The centralized

control could be performed either based on system model or model free strategy. A centralized management system gathers data and performs an optimization based on different objective functions, the system model parameters and constraints to come up with the set-points for the devices within the entity. The center-free strategies are classified into decentralized or distributed controls. Distributed methods use local information to adjust each device individually with no centralized entity. Decentralized methods utilize a combination of centralized and distributed controller schemes. Decentralized controls often control local issues by following a control law [6]. Figure 1.10, shows the different architectures of control management in distribution and microgrid systems. Center-free techniques are divided into distributed and decentralized control methods which cannot meet global objectives effectively as they deal with local control issues. Centralized control strategies that are based mostly on optimization techniques could meet multiple objectives based on network model details and day ahead planning that heavily depends on accurate forecasting of generation and load output. The centralized optimization is a one way communication while the decentralized techniques are based on a bi-directional communication network that exchanges information back and forth. Table 1.1 provides a summary of the differences among the three control techniques.

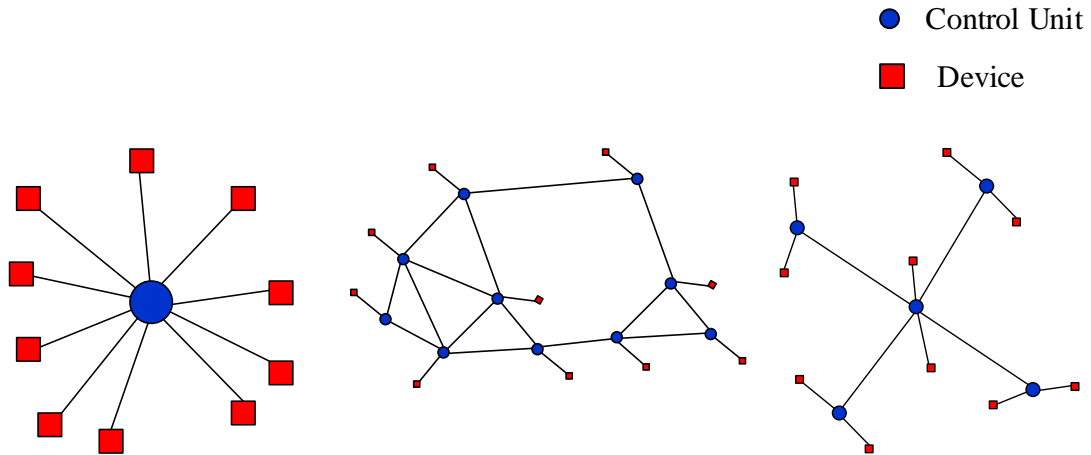


Figure 1.10: Different control architectures.

Table 1.1: Differentiating the three different control techniques.

Centralized	Distributed	Decentralized
Centralized Control- global objective	Distributed techniques- local objective	Combination of centralized and distributed techniques – both global and local objective
Global information to central control units	Local information to local control units	Local controllers and centralized entity to compute control law
Model and non- model based	Model free	Model free
Large unidirectional communication network	Large bi-directional communication	Less bi-directional communication

1.5. Microgrid: Hierarchical Control Levels

An overview of the different control levels from the standpoint of microgrids is given below [7]:

Primary Control: It is a local control strategy with the fastest response. It is heavily reliant on local measurements while requiring no communications. It is responsible for

the control action to provide power sharing while regulating voltage and frequency. For synchronous distributed generators the output control

Secondary Control: It is also referred as the Microgrid Energy Management system which is responsible for the reliability, security and economic operation.

Tertiary Control: It is at the highest level and is responsible for the coordinated operation of multiple microgrids. It is a part of the main grid control systems that controls optimal set-points for different microgrids.

The architectural structure of the different hierarchical control levels is shown in Figure 1.11.

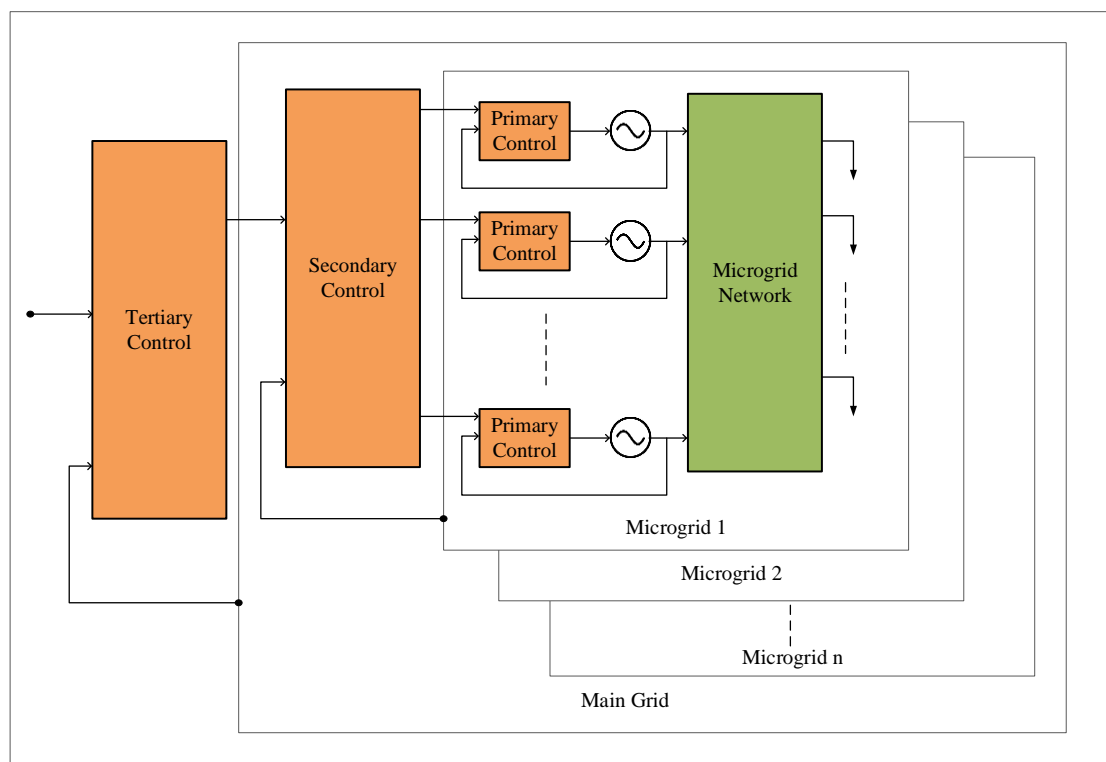


Figure 1.11: Hierarchical control levels: primary control, secondary control, and tertiary control.

Table 1.2 provides a summary of the state of the art in the primary and secondary control strategies in microgrid technologies.

Table 1.2: State of the art of primary and secondary control in microgrids.

Primary Control
<ul style="list-style-type: none"> ❑ Inverter Output Control <ul style="list-style-type: none"> ○ Mimic a synchronous generator using outer and inner control loops with PI controllers. ❑ Power Sharing Control <ul style="list-style-type: none"> ○ Droop Based: Communication free and based on local measurements. <ul style="list-style-type: none"> ▪ Conventional: Active power/frequency and Reactive power/voltage ▪ Modified: Active power/voltage and Reactive power/frequency, virtual output impedance, resistance etc. ○ Non-Droop based <ul style="list-style-type: none"> ▪ Master/follower control strategy ▪ Centralized controller with communication for reference set-points
Secondary Control
<ul style="list-style-type: none"> ❑ Centralized Approach <ul style="list-style-type: none"> ○ <i>Optimal Dispatch</i>: Cost functions, technical characteristics/limitations, network parameters and modes of operation ○ <i>Bidding</i>: Active participation of generators and customers by allowing them to bid their power production and consumption ○ <i>Non-Model-Based Approach</i>: Fuzzy controllers and ANN ○ <i>ESS Considerations</i>: Day ahead planning made feasible, Makes DG dispatchable, Aids in peak-shifting

- *Model Predictive Control*: Solution to optimal control problem solved over certain pre-defined horizon using the current state of the system as the initial state.
 - *Communications*: IEC 61850 standard, implemented over TCP/IP networks, abstract data models can be mapped to several protocols such as Generic Object Oriented Substation Events (GOOSE).
- **Decentralized Approach**
- Multi-Agent based*: Multiple intelligent agents interact with each other to achieve multiple global and local objectives.

1.5.1. Challenges to Meet Reliable and Economical Operation

When operating a microgrid the expected features to meet reliable and economical are given below [7]:

Output control: The ideal feature for DGs to track set-points and damp oscillations.

Power balance: In order to keep the frequency and voltage deviations within limits under uncertainty an islanded microgrid must balance active and reactive powers between generation and loads.

Demand Side Management (DSM): In the case of inadequacy in the generation, a portion of the load could be controlled or deferred to a different time period. Also, DSM might be important to maintain frequency in islanded mode with high renewable generation.

Economic dispatch: Particularly in a standalone microgrid to reduce the operating costs, or increase the profit DERs must be scheduled while maintaining reliability.

Transition between modes of operation: As microgrids have the ability to operate in both grid-connected as well as islanded conditions a smooth transition between grid-connected and islanded modes and vice versa is required along with high-speed islanding detection.

1.6. Case Studies Performed on DG Penetration that Motivates this Research

A few of the following real implementation of DER on active distribution networks is presented below that motivates the current research. The current practices to solve the issues occurring due to high DG penetration is discussed briefly.

1.6.1. Colorado State University (CSU) Foothills Campus, Fort Collins, Colorado

The CSU PV system was built in two phases, with a total peak rating of 5.2 MW by Xcel Energy. Their primary concern was with maintaining the voltage within ANSI C84.1 (range A) standards. The utility was concerned with regards to the high fluctuations in voltages which in turn would cause excessive load-tap changer (LTC) operations.

In order to mitigate the overvoltage issue, the utility has planned to follow 4 steps that include adjusting the voltage regulators to stabilize the voltage levels, then configuring the inverters (10 in total) to absorb 100 kVAr each followed by absorbing 150 kVAr each if necessary. The installed inverters must have the ability to absorb or supply VARs in accordance to the IEEE 1547 and UL 1741. In the worst case, the operator has planned to disconnect a part or the whole PV system if necessary along with installing a dynamic VAr compensator (DVC) or an additional power factor controller [8].

1.6.2. 2 MW Plant in Fontana, California

A 2 MW rooftop-mounted PV system was installed in Fontana, California in the Southern California Edison's (SCE) utility territory initially during the start of the project

but later on, a total PV capacity rating of 4.5 MW was interconnected to the circuit. Figure 1.12, shows the general configuration of the Fontana, California, study circuit. Voltage regulation is mainly accomplished by utilizing switched capacitor banks that are placed strategically in the feeder. The time delay setting for the capacitor banks were modified from 2 min to 30 sec to accommodate the high PV penetration. Based on the impact studies for SCEs plan to increase the PV penetration in their service territory, the inverters are planned to enable advanced inverter control features (Volt/VAr control, curtailment, etc.) in order to reduce the impacts of PV system variable generation on the distribution circuit [9]. Case studies proved that the inverter could be operated at off-unity power factor (i.e. any set-point power factor other than 1) which allowed reactive power to be adjusted to regulate the voltage at the interconnection point.

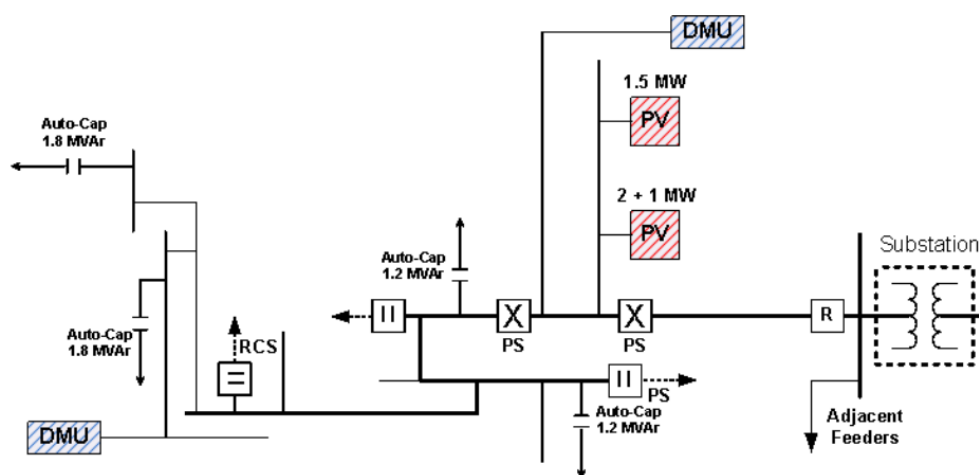


Figure 1.12: Simplified circuit diagram of the Fontana, California [10].

1.6.3. Hybrid Standalone Microgrid System in Isle of Eigg (Scotland)

A hybrid standalone microgrid has successfully been implemented in Isle of Eigg (Scotland) as shown in Figure 1.13 to supply electricity 24/7 to support the power needs of a community. 90% of the power is generated from renewable distributed energy resources along with a backup system used occasionally. The local grid has successfully

reduced its carbon emission from generated power. With a co-operative participation from customers, a demand response program is also implemented to help sustain a standalone microgrid. This model microgrid system could be utilized in developing countries who have much lesser load demands, with a much lower cost of operation to fulfill their needs. For continuous power, a backup power source such as a diesel generator could serve the imbalance. The total rated load is 225 kW for 38 households and 5 commercial properties distributed through 7 miles, but due to load changes and demand management practices, the total generation is able to meet the demand with time. This system proves the reliable power supply for a standalone system but its future implementation in other areas would be difficult without substantial subsidies on the initial capital investment [11].

(a)



(b)

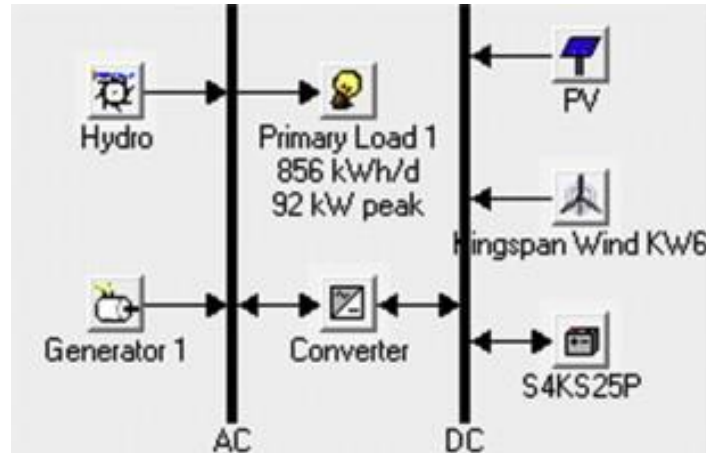


Figure 1.13: (a) Standalone microgrid components from top left: PV arrays, wind turbines, battery bank, diesel generator, inverters system, 6 kW hydro turbine, (b) Standalone microgrid system configuration [11].

1.7. Solutions and Dissertation Layout

Power quality in smart grid is of the utmost importance in the presence of highly stochastic renewable DGs and a barrier to wide-scale implementation in the distribution system. The dissertation is aimed at solving a few issues resulting from the high scale DG penetration by applying different control strategies.

Chapter 2 presents a communication free local control strategy to deal with the high ramp rates caused due to transient cloud movements.

Chapter 3 works towards a distributed voltage control strategy to deal with the high ramp rates caused due to transient cloud movements.

Chapter 4 deals with a centralized optimization strategy to schedule the utility scale PV system in a distribution system with cascaded voltage regulators

Chapter 5 covers the strategy of connecting hybrid PV/battery in a microgrid system to make them dispatchable.

Chapter 6 proposes a control strategy to operate DERs in the presence of fuel based dispatchable DGs and hybrid renewable DG/battery using a centralized controller for standalone microgrid operation.

CHAPTER 2 : DYNAMIC RAMP RATE CONTROL BASED ON LOCAL CONTROL STRATEGIES FOR VOLTAGE REGULATION IN DISTRIBUTION SYSTEMS WITH HIGH PENETRATION PHOTOVOLTAIC PLANT

2.1. Introduction

Multiple voltage regulating devices, such as on-load tap changer (OLTC), step voltage regulators (SVRs), switching capacitors banks work towards regulating the voltage in the distribution network. These conventional devices are based on Volt/VAr control strategies that work in a time coordinated strategy. However, in the case of distribution systems with Photovoltaic (PV) generations, a dynamically responsive voltage regulating device is required. Intermittency of PV output is a concern when injecting power into the grid. Most of the intermittency issues are not a high concern as they do not cause many problems to the power quality. If any power quality issues occur, they are taken care by the voltage regulating devices on the grid. At times during high PV outputs when the irradiance from the sun is high, cloud movements as shown in Figure 2.1 could cause a large change in power output in a short time duration. Case studies are performed to investigate the voltage regulation at the PV bus during ramp up/down case. All the control devices operate on local measurement and control techniques and do not communicate and coordinate with each other. The system is tested with a local reactive power support to mitigate the issues occurring from high ramp-up cases. An alternate method using an energy storage device to regulate the target PV bus voltage during the ramp up/down of PV power is proposed. A novel ramp rate control algorithm based on

the current state of charge is also discussed. A benchmark MV distribution network model is developed and simulated in PSCAD/EMTD environment and the results validate the proposed coordinated voltage control strategy.

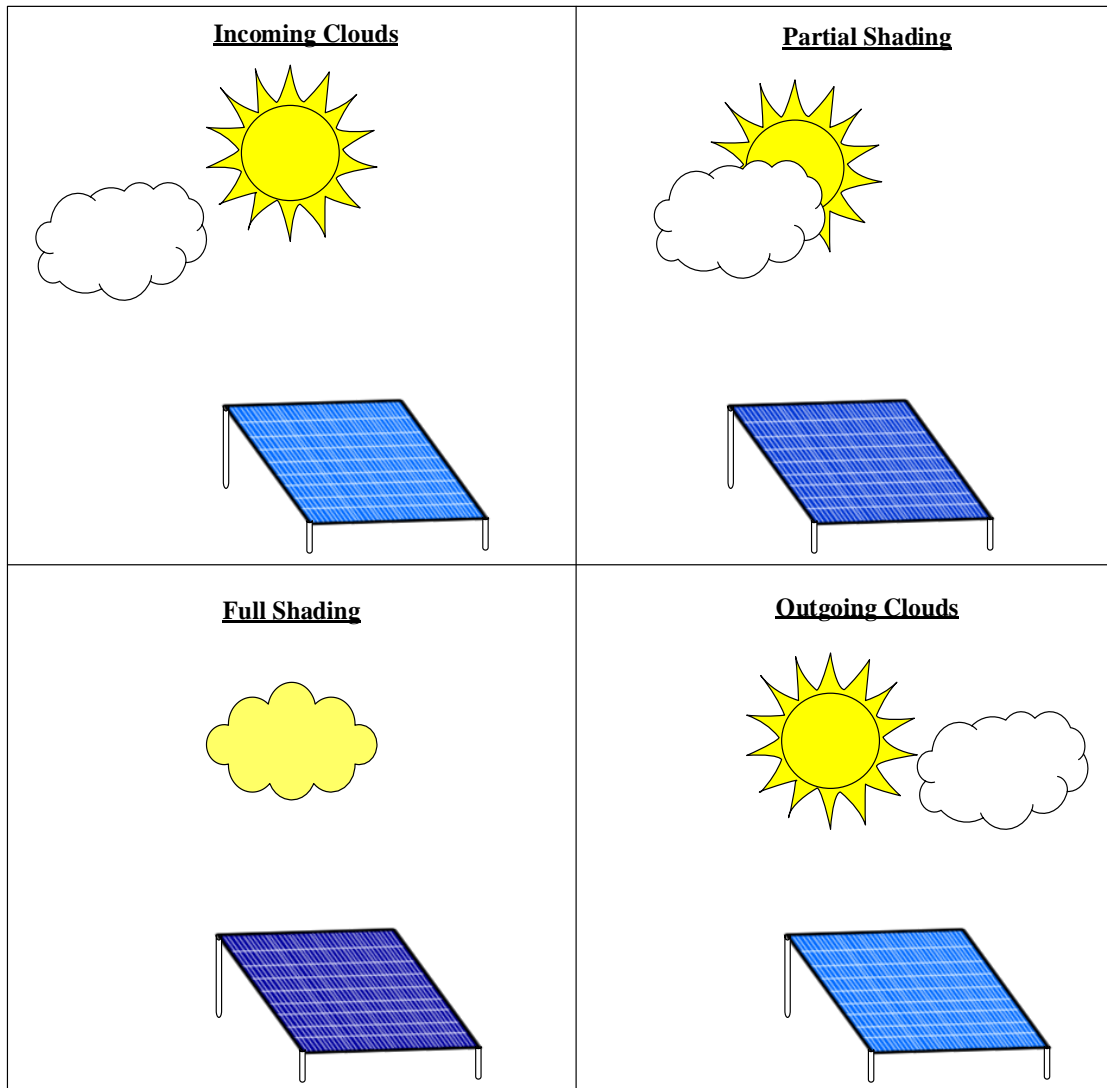


Figure 2.1: Effect of cloud movement and sun blocking on a solar panel.

2.2. Communication-Free Ramp Rate Control Based on Local Measurements

A novel algorithm for ramp rate control based on the BESS State of Charge (SoC) is designed to reduce the impact on local voltages due to PV output rise/fall in a short duration. The purpose of the BESS is to provide power to the PV plant in the ramp-down mode or absorb power from the PV plant in the ramp-up mode. In other words, by

changing the ramp rate of PV power variations, the BESS prevents sudden changes in solar power injection levels, which can make the system operation difficult for distributed generators when the PV penetration is high. The BESS behaves as a power smoothing device which could provide backup power to the grid while the generators ramp up and down, reducing the long-term wear and tear of the static voltage regulating devices. In order to do that, the change in power with respect to time becomes an important factor. If a decrease or increase in power with time beyond the limits is detected, the BESS would have to respond to the change much quicker. A sudden decrease in PV power is associated with a negative slope; therefore the BESS needs to supply ramped power with a positive slope to reduce the change in power with time which ultimately smoothens the injected power to the grid [12]. The injected power from the PV/BESS system is given as shown in (2.1).

$$P_{inj}^{smooth} = \eta_{inv} (P_{PV} + P_{BESS}) - P_L \quad (2.1)$$

The injected power at the inverter terminals of the PV/BESS system with charge/discharge rate is as given below in (2.2).

$$P_{inj} = -P_L + \eta_{inv} (P_{PV} \pm V_B I_B) \quad (2.2)$$

where P_{inj} is the injected power to the grid from the PV/BESS system, P_L is the load at the system bus, P_{PV} is the power from the PV modules, V_B is the voltage at the battery terminals, I_B is the battery current which could either be the charging rate (CR) or discharging rate (DR) and η_{inv} is the efficiency of the inverter.

By assuming that the change in load power, P_L is not significant for small time instants, the change in injected power with time can be measured by differentiating with respect to

time as shown in (2.3).

$$\frac{dP_{inj}}{dt} = \eta_{inv} \left(\frac{dP_{PV}}{dt} + V_B \frac{dI_B}{dt} \right) \quad (2.3)$$

where dI_B/dt is either positive or negative based on charging or discharging command.

The rate of PV power change with time step is calculated by (2.4).

$$\frac{dP_{PV}(t)}{dt} = \frac{P_{PV}(t) - P_{PV}(t - \Delta t)}{\Delta t} \quad (2.4)$$

The ramp down and up windows for each time step is shown in Figure 2.2. A slope k^{limit} is also shown in the window which indicates the limit of ramp down/up.

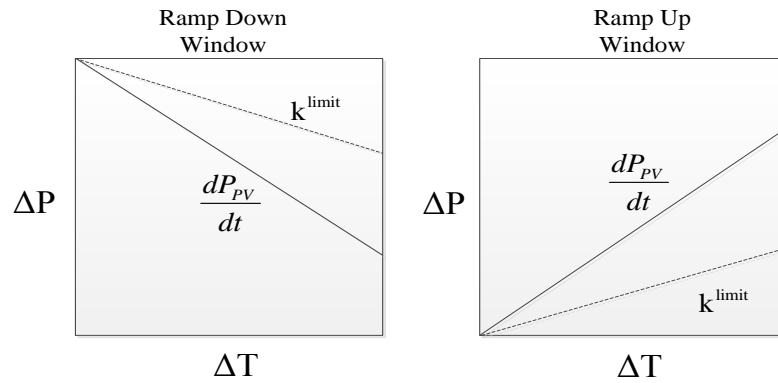


Figure 2.2: Sliding window with width Δt .

For a discharging rate command when $|dP_{PV}/dt| \geq |k^{\text{limit}}|$ the equation can be rewritten as shown in (2.5).

$$\frac{dDR}{dt} = \frac{k^{\text{drop}}}{\eta_{inv} V_B} - \frac{1}{V_B} \frac{dP_{PV}}{dt} \quad (2.5)$$

Where k^{drop} is the slope of the desired rate of change of injected power with respect to time. k^{drop} is the interpolation value between $k^{\text{drop},90\% \text{soc}}$ and $k^{\text{drop},10\% \text{soc}}$. $k^{\text{drop},90\% \text{soc}}$ is the desired injected power slope at 90% SoC which is the maximum limit of the battery while $k^{\text{drop},10\% \text{soc}}$ is the desired injected power slope at 10% SoC which is the minimum

limit of the battery. $k^{\text{drop},90\% \text{ soc}}$ could be a zero slope line in order to inject power without any change with time, while $k^{\text{drop},10\% \text{ soc}}$ could be the k^{limit} .

Similarly for the ramp up case, if the rate of change of increase in power, $|dP_{PV}/dt| \geq |k^{\text{limit}}|$, the equation for charging rate is given as below in (2.6).

$$\frac{dCR}{dt} = \frac{1}{V_B} \frac{dP_{PV}}{dt} - \frac{k^{\text{rise}}}{\eta_{\text{inv}} V_B} \quad (2.6)$$

where k^{rise} is the slope of the desired rate of change of injected power with respect to time. k^{rise} is the interpolation value between $k^{\text{drop},90\% \text{ soc}}$ and $k^{\text{drop},10\% \text{ soc}}$. $k^{\text{drop},90\% \text{ soc}}$ is the desired injected power slope at 90% state of charge (SOC) which is the maximum limit of the battery while $k^{\text{drop},10\% \text{ soc}}$ is the desired injected power slope at 10% state of charge (SOC) which is the minimum limit of the battery. $k^{\text{drop},90\% \text{ soc}}$ could be k^{limit} while $k^{\text{drop},10\% \text{ soc}}$ could a zero slope line in order to inject power without any change with time. The dynamic ramp threshold determination based on current SOC levels is shown in Figure 2.3. The overall design of the ramp rate control is shown in Figure 2.4 [13].

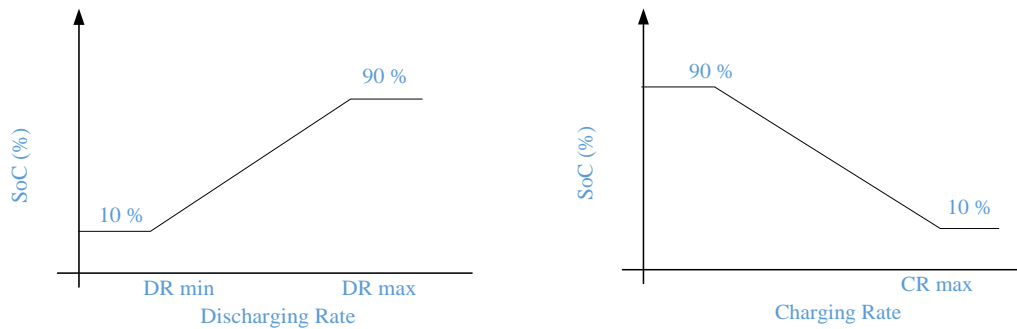


Figure 2.3: Dynamic ramp threshold determination based on current SOC levels.

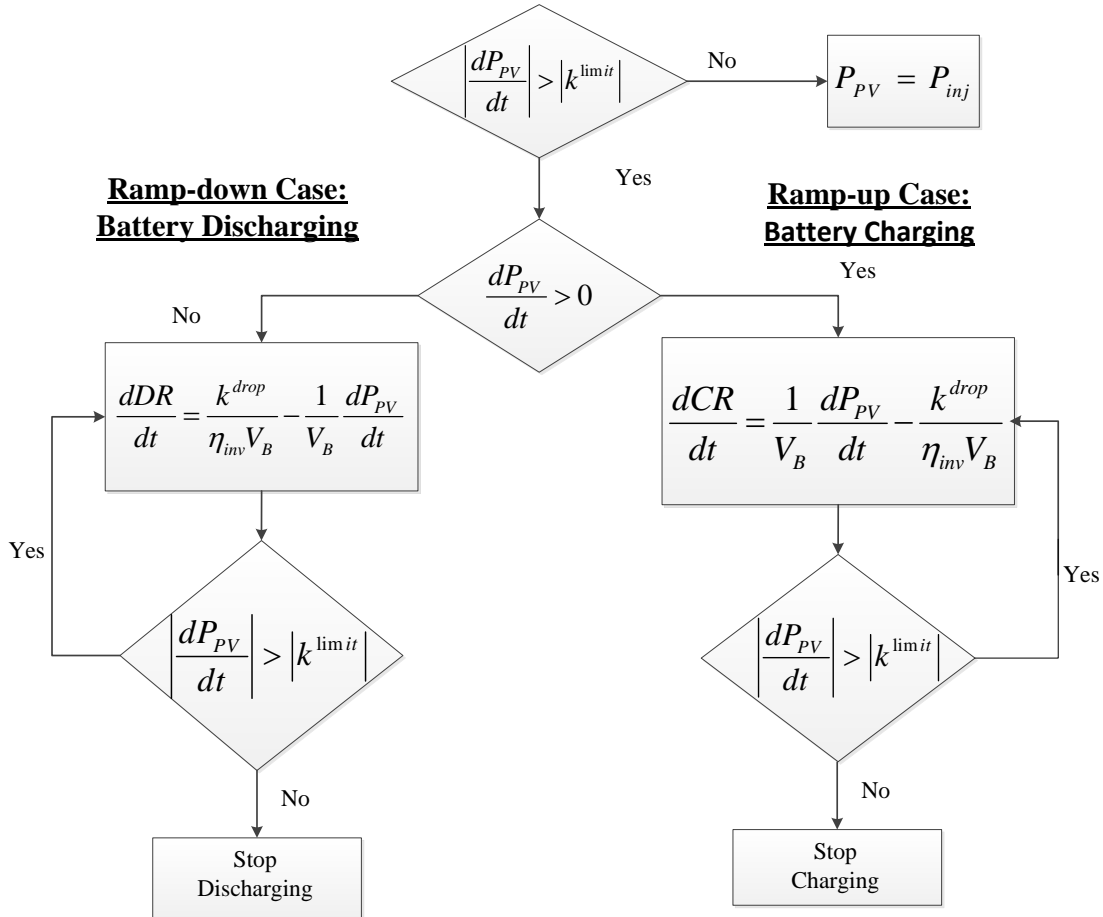


Figure 2.4: Ramp rate control algorithm.

The required ramp rate usually depends on the system control delays but always limited to the battery capacity. The size of the battery can be calculated based on the equation shown below in (2.7) [5].

$$\Delta E = \frac{1}{2} P_{PV,max} T_{ramp,max} \quad (2.7)$$

where $P_{PV,max}$ is the rated PV output, $T_{ramp,max}$ is the maximum desired time taken to either drop from $P_{PV,max}$ to 0 or rise from 0 to $P_{PV,max}$. The slope of such a ramp is associated with ramp limit $|k^{limit}|$. In this case, the maximum ramp rate limit is $|P_{PV,max}/T_{ramp,max}|$. ΔE is the maximum discharge/charge energy which can be used to

size the battery. For example, if $P_{PV,max} = 2$ MW and $T_{ramp,max} = 10$ min, the battery can be sized to 0.333 MWhr.

2.3. Distribution Feeder

The system used for the simulation purpose was a medium-voltage (MV) distribution substation feeder belonging to Pacific Gas and Electric (PG&E) located in California, with regular voltage regulation devices that are mostly static in nature. The system is shown in Figure 2.5. The feeder is at 12 kV base. The transformer is rated at 15 MVA. At the feeder side, an on-load tap changing (OLTC) transformer is used. Step voltage regulators (SVR) are located at various locations on the distribution system. The highest stress would be on voltage regulators SVR 1 and 3 which are directly in radial line with the PV. These static devices take around 1~1.5 min to respond to a voltage violation case initially and 15 sec delay for the next steps. A switching capacitor rated at 1.2 MVAR, is used at a specific location on the feeder. A Dynamic VAR Compensator (DVC) is utilized nearer to the PV location that behaves similarly as a STATCOM [5]. There is some distance between the DVC and PV which would create different voltage profiles. It takes around 3 sec for a DVC to respond to any voltage violation case. The DVC voltage is regulated at 1.019 pu, with a bandwidth set at $+/- 0.002$ p.u. The DVC is around 1.47 miles away from the PV point of interconnection (POI). A PV is connected far away from the feeder and operated with unity power factor. In the first case study, the PV is connected directly at the POI without considering a battery and hence without any ramp rate control. In the second case study the battery is connected inside the PV to perform the ramp rate control as mentioned in the previous section. Both charging and discharging processes would be discussed in the ramp rate control process.

2.4. Case Studies

Simulations were performed using real feeder data from a California Utility. During sunrise, the solar irradiance increases with a high ramp rate from $t=4$ min, and within a few minutes, reaches its rated value as shown in Figure 2.6. The irradiance value drops to a low value suddenly at $t=16$ min. The solar radiation profile is from North California (a cloudy day) in the summer.

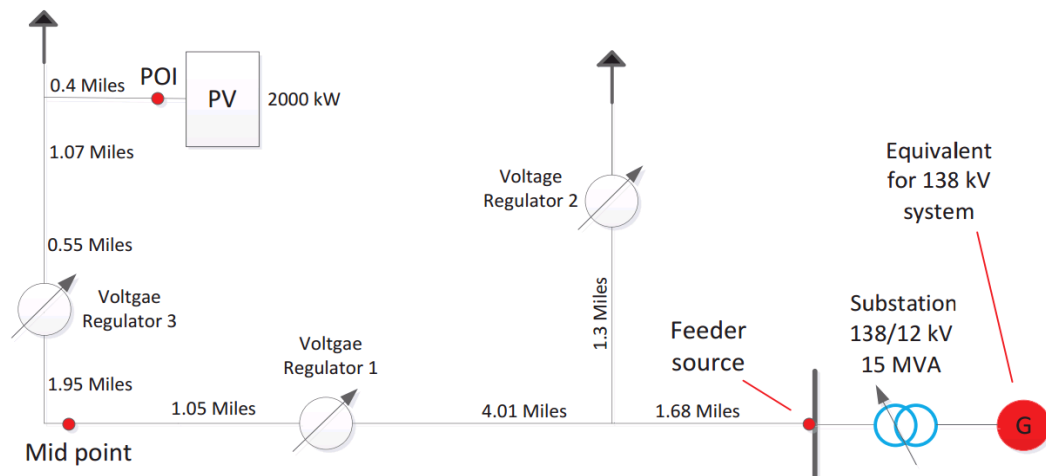


Figure 2.5: Reduced MV distribution feeder with PV as DG.

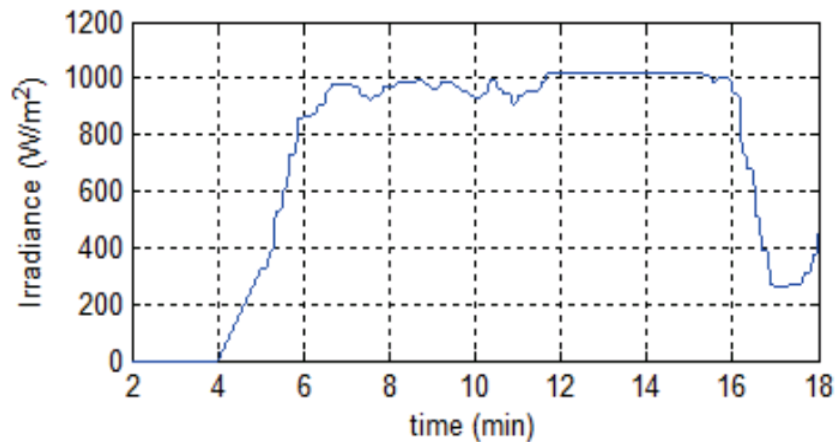


Figure 2.6: Ramp-up event: Solar Irradiance during sunrise and ramp-down even due to cloud covering.

2.4.1. Without Ramp Rate Control

During the increase in solar irradiance, the active power from the PV array increases as expected and the reactive power output remains near zero. As the PV power increases, the active power flow through the feeder decreases since the local load is fed by the PV array instead of the grid. Simulation results of PV power flows are shown in Figure 2.7(a). As the PV power keeps increasing, at around time $t = 5.1$ min, the voltage hits the upper limit of 1.05 pu as shown in Figure 2.7(b) which causes the SVR 1 and 3 to change its tap ratios to a lower value. The voltage at the PV terminals reaches around 1.07 pu.

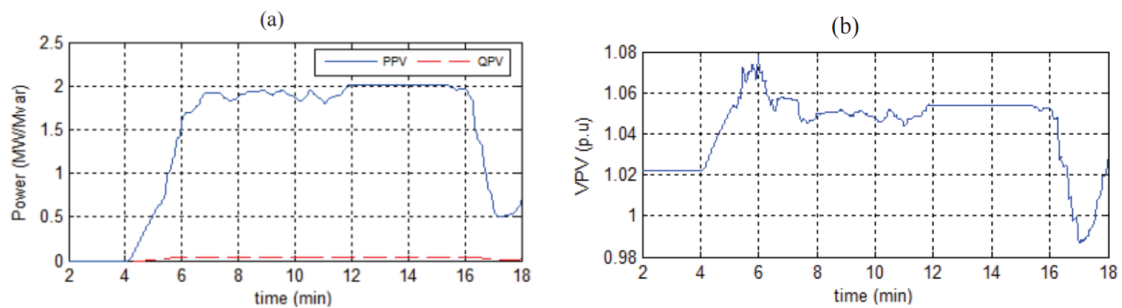


Figure 2.7: (a) PV active and reactive power, (b) PV node rms voltage.

The DVC as mentioned earlier, is the closest voltage regulating device with the fastest response time. The DVC operates in order to reduce the reactive power injection when the PV active power increases. The reactive power absorbed by the DVC during this operation is shown in Figure 2.8(a). The DVC target bus voltage is shown in Figure 2.8(b).

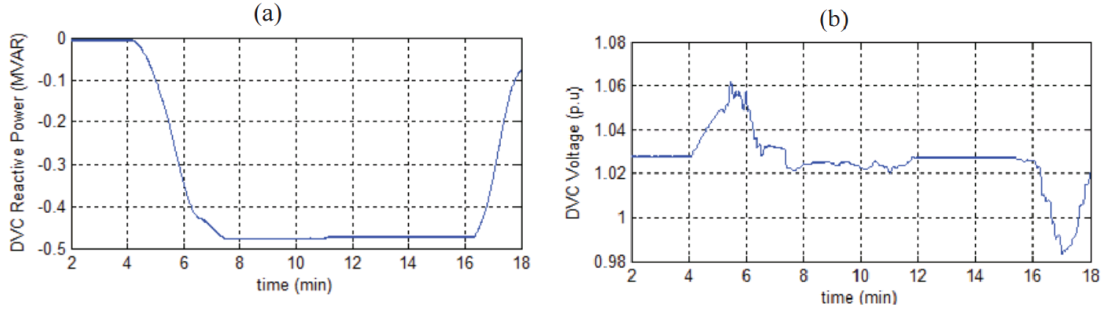


Figure 2.8: (a) DVC reactive power output, (b) DVC node rms voltage.

The tap setting change for SVR 1 is shown in Figure 2.9(a) and for SVR 3 in Figure 2.9(b). It can be seen that as the PV output increases in the time frame, the voltage at the nearby buses increases, not giving enough time for the SVRs to respond to the change.

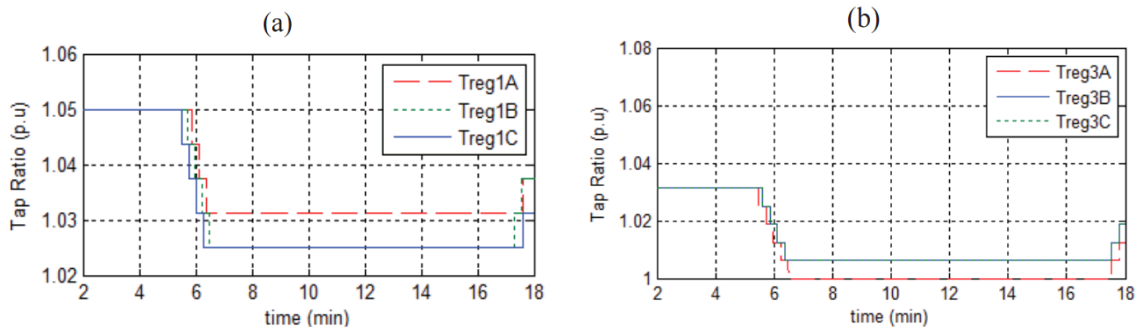


Figure 2.9: (a) Phase tap ratios in pu for SVR 1 (b) Phase tap ratios in pu for SVR 3.

2.4.2. With Ramp Rate Control

In this case, the change in the solar irradiance is the same as in the previous section for the case with no ramp rate control. After the ramp-rate control is applied to the PV, the rise in PV power at the terminals takes longer to reach its rated value. Similarly, when the irradiance drops at 16 min, the drop in PV terminal power is delayed. Figure 2.10(a) shows the power flow at the PV terminals. Due to the delayed ramp rate increase, the battery charges or absorbs power, whereas the delayed ramp rate decrease leads to the battery discharging or releasing power, which can be seen in the Figure 2.10(b). The state of charge during the simulation period is shown in Figure 2.10(c). As can be seen from

Figure 2.10(d), the voltage at the PV bus, V_{PV} rises slowly, which gives time for the SVR 1 and 3 to respond with its delay settings. The ramp rate is 0.166 MW/min and the results show negligible voltage violation (0.005 pu) in the worst case.

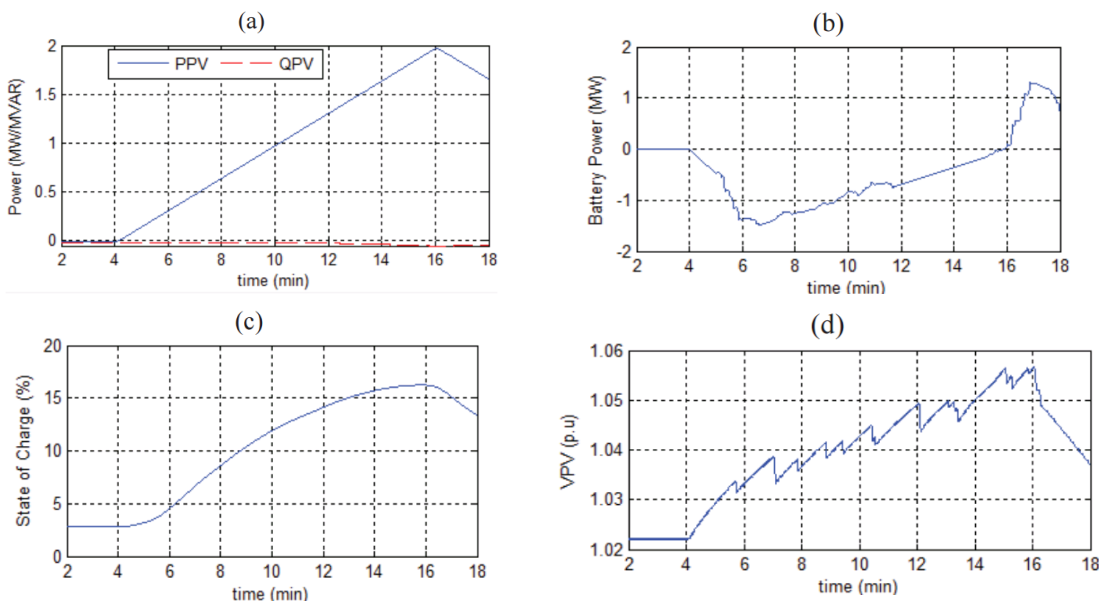


Figure 2.10: (a) PV active and reactive power, (b) Battery power, (c) Battery SoC and (d) PV node rms voltage.

The DVC responds to the voltage rise by changing its reactive power based on the settings. Comparatively, the DVC delays its reactive support due to the delay in PV output. The change in the reactive power is shown in Figure 2.11(a). Figure 2.11(b) shows the voltage profile at the DVC terminals.

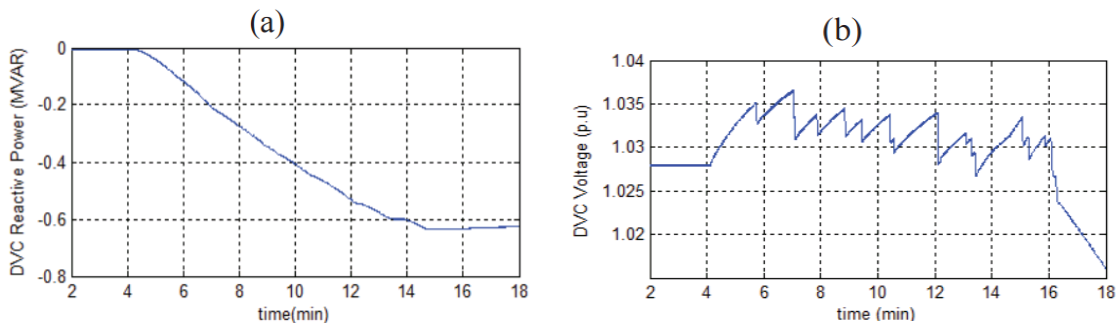


Figure 2.11: (a) DVC Reactive Power Output, (b) DVC node RMS voltage

The tap setting changes for SVR 1 and SVR 3 are shown in Figure 2.12(a) and (b) respectively. Due to the delay in the rise in power, the voltage regulating devices were able to respond to the voltage increase prior to the voltage violation

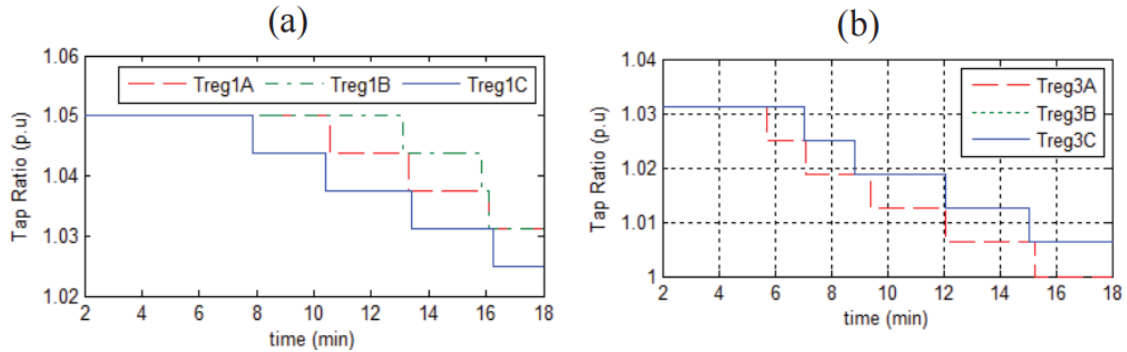


Figure 2.12: (a) Phase tap ratios in pu for SVR 1 (b) Phase tap ratios in pu for SVR 3

2.5. Summary

A case study was performed on an actual MV distribution feeder with conventional voltage regulating devices. A dynamic compensator was also installed near the PV but proved unsatisfactory as reactive control was not enough. In many cases, like the example in this work, ramp rate control with BESS would be an ideal method to mitigate a PV plant's impact on voltage violations. Slowing down the rate of change in a PV plant's MW output may let other voltage controlling equipment in the system have enough time to react properly, and also save energy in comparison to other similar mitigation methods. There would be less wear and tear in the static voltage regulating devices as they would not have to respond to fast increase in voltage which causes an increase in the tap changing steps. Ideally, ramp rate control would be done by fast battery storage inside of the PV system. Ramp up and down control with the help of a battery can prove to be beneficial as a result of the transfer of power from one period to

another. The advantage of ramp rate control is also on reducing the range of voltage variation as well as improving the maximum and minimum voltages.

CHAPTER 3 : DISTRIBUTED CONTROL OF VOLTAGE REGULATING DEVICES IN THE PRESENCE OF HIGH PV PENETRATION TO MITIGATE RAMP-RATE ISSUES

3.1. Introduction

Large scale PV plants are becoming a norm on many distribution utility feeders, especially to provide electrical support to large commercial customers that intend to reduce their electricity bill. Power generated by PV panels depend on the sun's irradiance that is available only when the sun is shining. Cloud movements that block direct sunlight frequently, are the major cause for high ramp up/down events as they increase/decrease the power output from PV panels in a short time duration. Utilities need to know the negative impacts that will be caused by reverse power changes from large-scale PV installation when a cloud's shadow passes over a large PV system. Such short duration events cannot be predicted ahead of time as it is difficult to forecast the PV variation due to cloud movement. Therefore an online estimation and control operation is needed to take fast actions when there is a high change in power output from PV plants. In this chapter first, a basic control operation utilizing reactive power support and active power control using a battery from a smart inverter based on local measurements and without any communications between regulating devices is proposed. Next, a distributed voltage control (DVC) scheme is proposed in an active distribution network (ADN) in the presence of high penetration photovoltaic (PV) generation to mitigate high ramp-rate issues. Multiple voltage regulating devices such as on-load tap changers (OLTC), step

voltage regulators (SVRs), and switched capacitors banks (SCBs) are controlled in various ways based on either a centralized or a distributed coordination management scheme. This work presents the relationship of the active and reactive power outputs of a PV plant in the presence of the conventional voltage regulating devices, and proposes a distributed control strategy to coordinate the SVRs with the PV inverter's capability to improve power quality. In order to estimate and predict the impact of active and reactive power injection by the PV system on the node voltages, a sensitivity tool is utilized for predicting the impacts and perform control actions ahead of time. The distributed voltage control schemes are tested on an unbalanced medium voltage (MV) feeder located in a California utility service territory with the PV integrated at the far end of the feeder.

3.2. Literature Review

The injection of megawatt (MW) scale renewable power generations into the medium-voltage (MV) grid poses various power quality issues in the distribution system. With the high penetration of distributed solar photovoltaic (PV) power plants connected to a strong grid, there are more issues with voltage stability/violations locally than with frequency stability. The stochastic nature of the PV plant output needs to be countered with the help of regulating devices on the distribution system. Most of the present voltage regulating devices on the distribution system are passive in nature and take several minutes to respond to the fast rise and drop in power which result from the variability in the solar irradiance.

Whenever the active power changes rapidly after shading event resulting from clouds passing over the panels, it causes severe fluctuations in voltages sometimes leading to over voltage situations for a period of time [14]. The step voltage regulating devices

might not be enough to mitigate the rapid changes as the tap changers are a function of time delay. In order to mitigate the rapid changes in PV output, a smart inverter needs to be implemented that is able to adapt to the varying conditions in a given day. A smart inverter, in this case can be supported by energy storage devices that are able to absorb and deliver power to the system. Another function of a smart inverter is to absorb and release reactive power to mitigate the impact of voltage fluctuations. Reactive power support by an inverter is dependent upon the active power output from the PV system [4].

In case there is a fast change due to cloud passing, the power from the PV system either falls or rises at a higher ramp rate, which needs to be countered by smart inverter functionalities with the help of conventional regulating devices. Usually while forecasting the PV profile for the next day, some uncertainties such as cloud movement, partial shading etc. are not considered or predicted accurately. A number of works have dealt with the ramp rate control that includes both reactive power support as well as active power curtailment. In [15], reactive power absorption based on the rate of change of the PV panel output was suggested. In [16], active power curtailment was suggested based on the rate of change of voltage at the PV bus terminals. In this work the smart inverter functionality is suggested along with the SVR based on a center-free communication layer. The effectiveness of reactive power support from the DGs to regulate voltage is heavily dependent on the network characteristics. In case the X/R ratio of the network is low, the active power flow in the reverse direction causes a higher voltage drop in the opposite direction causing the voltage to go higher than the ANSI C84.1 standards [17].

In [18], a ramp rate control based on inverse ramp rate measurements and assisted by energy storage was introduced to mitigate the fluctuations of PV output that have an adverse effect on the power quality of the system. A BESS would be charged during ramp-up case and discharged during the ramp-down case which would be economically beneficial as compared to the costly ancillary services provided by the conventional generators [19]. In [20], a hybrid storage system that included a supercapacitor in parallel with a battery was connected to the DC link of a permanent magnet synchronous generator (PMSG) in order to take care of the voltage and frequency regulation during an islanded condition. In order to regulate voltage on the distribution system, the distribution system operator (DSO) can adopt either a centralized or distributed control scheme. An uncoordinated control scheme was introduced to regulate the voltage in a microgrid by reactive power support from DG based on sensitivity analysis in [21]. In [22], a centralized controller was developed to schedule the OLTC, SVRs, SCBs in order to optimally control the voltage. In cases where optimal management of regulating devices to meet multiple objectives (e.g., loss minimization, tap changes reduction, battery cycles reduction etc.), a centralized controller proves effective but would fail to coordinate well between the local regulating devices that are meant to regulate voltage at a critical bus due to lack of plug and play characteristics. A centralized controller is expensive and unreliable for long distance communications, and thus it is ineffective for local control actions. Decentralized control schemes have proved effective to coordinate well between the DGs and other regulating devices as they regulate voltages based on control laws which require continuous communications. In [23], a summary of decentralized voltage control techniques were discussed. In [24], a power threshold value was determined by

optimization technique to trigger an energy storage charging to prevent overvoltage conditions occurring in LV grid due to high PV penetration. In [25], a decentralized coordinated voltage control scheme between DG and OLTC was introduced to exchange the roles of a master and follower based on dynamically varying situation in order to regulate the voltage at the critical bus by only reactive power support. In [26], a new optimal control law for decentralized autonomous control was suggested for large voltage fluctuations caused by varying PV output by utilizing a multi-agent system. In [25], STATCOM and static VAR compensator (SVC) were utilized to mitigate fast voltage changes and help improve voltage and transient stability. Due to high R/X ratios of conductor/cables in a MV grid, reactive power support is not enough and dynamic active control is required to keep the voltages within the required bandwidth [27]. In cases where online control is required for ramp rate control, the centralized and decentralized controller would fail to regulate the voltage effectively due to latency in communications. Distributed control schemes prove effective in that case as regulation is performed based on local signals with minimum communications during voltage violation cases. There is no requirement for network model information when compared with the other schemes. In this work, the interplay between PV smart inverter and voltage regulation devices is investigated in a distribution system with high PV penetration. The issue of response and coordination among the existing devices are discussed via simulations. Active power curtailment might be required in case of high ramp output due to cloud passing which can be performed in coordination with energy storage devices that is able to charge during ramp-up and discharge during ramp-down. Many controls discussed in previous works have not explicitly catered to the ramp rate control action. In this work, a novel method

for investigating the requirement of curtailment based on the voltage estimation at the end of high ramp-up or a ramp-down event is discussed. A DVC scheme is setup so as to involve only local regulating devices, such as the SVR, smart inverter with active and reactive power control capability.

3.3. Theory and Proposed Solution

In DVC, the dead-band comparator receives signals from the PV bus that is connected with a smart meter that could communicate via power line communications [14] or a radio frequency (RF) mesh. The controller sends signals to the time delay controller to begin controlling active and reactive power when required. In case no smart inverter capabilities are applied, the cascaded SVRs operate with a time-graded operation.

3.3.1. Power Sensitivity Calculation

In a simple balanced feeder represented by equivalent resistance R_{eq} and reactance X_{eq} between the source node 0 and DG power source node j the voltage at the DG bus, V_j with respect to the source node voltage, V_0 is given by (1).

$$V_j \approx V_0 + \frac{(P_j R_{eq} + Q_j X_{eq})}{V_j} \quad (3.1)$$

where, P_j and Q_j are the injected active and reactive power, respectively at the node j .

Using the concept of cascaded ABCD parameters (a, b, c, d matrices of size 3×3) in an unbalanced system, that characterize the line and load modeling between two nodes, the relationship between source node and DG bus voltage and current injection is derived as follows. The detailed modeling of the unbalanced system could be found in [28]. In the case of unbalanced distribution feeders, the power-flow solution is obtained through

forward sweep/backward sweep iterations where each component is modeled using ABCD parameters.

Firstly, for a 3-phase line segment as shown in Figure 3.1, the equations representing the relationship of phase voltages and currents with respect to two nodes, input *Node n* and output *Node m* are presented as shown in (3.2).

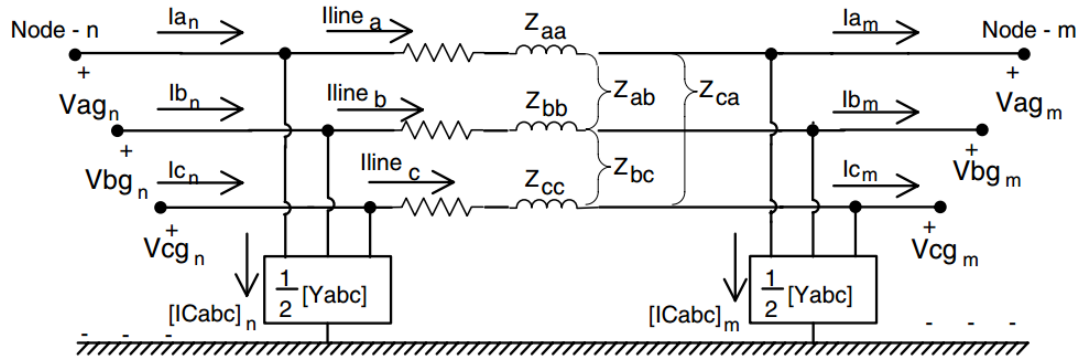


Figure 3.1: 3-phase line segment model.

By applying Kirchhoff's current law at Node *m*.

$$\begin{bmatrix} Iline_a \\ Iline_b \\ Iline_c \end{bmatrix} = \begin{bmatrix} I_a \\ I_b \\ I_c \end{bmatrix}_m + \frac{1}{2} \begin{bmatrix} Y_{aa} & Y_{ab} & Y_{ac} \\ Y_{ba} & Y_{bb} & Y_{bc} \\ Y_{ca} & Y_{cb} & Y_{cc} \end{bmatrix} \cdot \begin{bmatrix} Vag \\ Vbg \\ Vcg \end{bmatrix}_m \quad (3.2)$$

Rewriting (3.2) in a condensed form as shown in (3.3)

$$[Iline_{abc}] = [I_{abc}]_m + \frac{1}{2} [Y_{abc}] \cdot [VLG_{abc}]_m \quad (3.3)$$

By applying Kirchhoff's voltage law to the model gives the relationship between the voltages at buses *m* and *n* with the current flow as shown in (3.4).

$$\begin{bmatrix} Vag \\ Vbg \\ Vcg \end{bmatrix}_n = \begin{bmatrix} Vag \\ Vbg \\ Vcg \end{bmatrix}_m + \begin{bmatrix} Z_{aa} & Z_{ab} & Z_{ac} \\ Z_{ba} & Z_{bb} & Z_{bc} \\ Z_{ca} & Z_{cb} & Z_{cc} \end{bmatrix} \cdot \begin{bmatrix} Iline_a \\ Iline_b \\ Iline_c \end{bmatrix} \quad (3.4)$$

Rewriting (3.4) in a condensed form gives (3.5).

$$[VLG_{abc}]_n = [VLG_{abc}]_m + [Z_{abc}] \cdot [Iline_{abc}]_m \quad (3.5)$$

By substituting (3.2) in (3.4), the following equation (3.6) can be obtained.

$$\begin{aligned} [VLG_{abc}]_n &= [a] \cdot [VLG_{abc}]_m + [b] \cdot [I_{abc}]_m \\ \text{where} \quad [a] &= [U] + \frac{1}{2} \cdot [Z_{abc}] \cdot [Y_{abc}] \\ [b] &= [Z_{abc}] \\ [U] &= \begin{bmatrix} 1 & 0 & 0 \\ 0 & 1 & 0 \\ 0 & 0 & 1 \end{bmatrix} \end{aligned} \quad (3.6)$$

The input current at *Node n* is given by (3.7).

$$\begin{bmatrix} I_a \\ I_b \\ I_c \end{bmatrix}_n = \begin{bmatrix} Iline_a \\ Iline_b \\ Iline_c \end{bmatrix} + \frac{1}{2} \begin{bmatrix} Y_{aa} & Y_{ab} & Y_{ac} \\ Y_{ba} & Y_{bb} & Y_{bc} \\ Y_{ca} & Y_{cb} & Y_{cc} \end{bmatrix} \cdot \begin{bmatrix} Vag \\ Vbg \\ Vcg \end{bmatrix}_n \quad (3.7)$$

Rewriting (3.7) in a condensed form is shown in (3.8).

$$[I_{abc}]_n = [Iline_{abc}]_m + \frac{1}{2} [Y_{abc}] \cdot [VLG_{abc}]_n \quad (3.8)$$

By substituting (3.8) in (3.3), the following equation (3.9) can be obtained.

$$\begin{aligned} [I_{abc}]_n &= [c] \cdot [VLG_{abc}]_m + [d] \cdot [I_{abc}]_{nm} \\ \text{where} \quad [c] &= [Y_{abc}] + \frac{1}{4} \cdot [Y_{abc}] \cdot [Z_{abc}] \cdot [Y_{abc}] \\ [d] &= [U] + \frac{1}{2} \cdot [Z_{abc}] \cdot [Y_{abc}] \\ [U] &= \begin{bmatrix} 1 & 0 & 0 \\ 0 & 1 & 0 \\ 0 & 0 & 1 \end{bmatrix} \end{aligned} \quad (3.9)$$

Finally, the two port system relating the input voltages and currents to the output voltages and currents can be written in the form that represents a backward sweep as shown in (3.10).

$$\begin{bmatrix} [VLG_{abc}]_n \\ [I_{abc}]_n \end{bmatrix} = \begin{bmatrix} [a] & [b] \\ [c] & [d] \end{bmatrix} \cdot \begin{bmatrix} [VLG_{abc}]_m \\ [I_{abc}]_m \end{bmatrix} \quad (3.10)$$

For simplicity, the phase index is removed and only the voltages and currents at each node are represented as vectors. From (3.10), the backward sweep equation from node i to DG bus j can be written as shown in (3.11).

$$\begin{aligned} V_i &= a_{i \rightarrow j} V_j + b_{i \rightarrow j} I_j \\ I_i &= c_{i \rightarrow j} V_j + d_{i \rightarrow j} I_j \end{aligned} \quad (3.11)$$

where the equivalent ABCD parameters between any node i and DG bus j is calculated as shown in (3.12).

$$\begin{bmatrix} a_{i \rightarrow j} & b_{i \rightarrow j} \\ c_{i \rightarrow j} & d_{i \rightarrow j} \end{bmatrix} = \prod_{g \in \Psi} \begin{bmatrix} a_g & b_g \\ c_g & d_g \end{bmatrix} \quad (3.12)$$

where Ψ is the set of series components forming a path between the node i and node j .

Similarly, the backward sweep equation from source node 0 to DG bus j can be written as shown in (3.13).

$$\begin{aligned} V_0 &= a_j V_j + b_j I_j \\ I_0 &= c_j V_j + d_j I_j \end{aligned} \quad (3.13)$$

In the forward sweep, the voltage at the DG bus node j can be written as (3.14).

$$V_j = A_j V_0 + B_j I_j, \quad \text{where } A_j = a_j^{-1}, B_j = -a_j^{-1} b_j \quad (3.14)$$

Equating (3.1) with (3.14) and performing partial differentiation, sensitivities of the voltage at the node j to the injected active and reactive power at the same node is given by (3.15).

$$\frac{\partial V_j}{\partial P_j} = \frac{R_{eq}}{V_j}, \quad \frac{\partial V_j}{\partial Q_j} = \frac{X_{eq}}{V_j} \quad (3.15)$$

where equivalent resistance and reactance can be rewritten as shown in **Error!**

Reference source not found.

$$R_{eq} = -\text{Re}([B_j]) \text{ and } X_{eq} = -\text{Im}([B_j]) \quad (3.16)$$

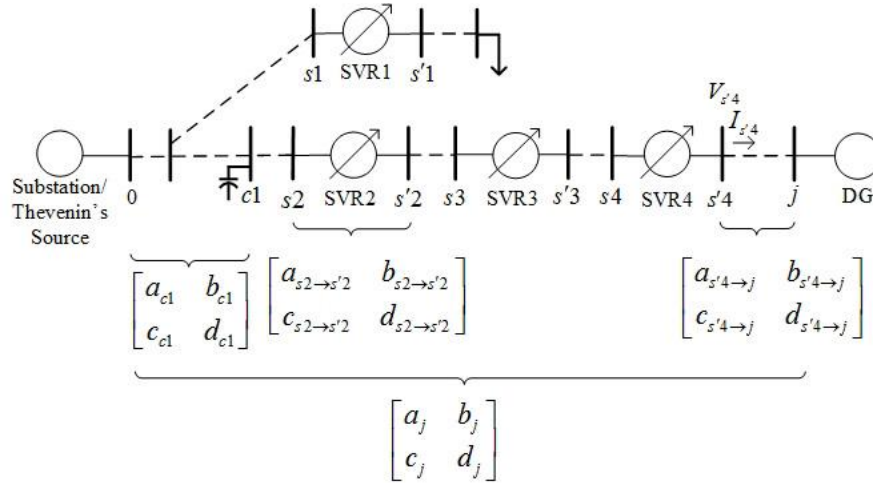


Figure 3.2: Voltage-power sensitivity calculation.

By utilizing the superposition principle, the total change in voltage due to changes in active and reactive power at the node j is given by (3.17).

$$\Delta V_j = \Delta P_j \frac{\partial V_j}{\partial P_j} + \Delta Q_j \frac{\partial V_j}{\partial Q_j} \quad (3.17)$$

3.3.2. SVR Tap Operation

In previous work, it has been proved that by including large scale PV on a MV distribution system the number of tap changes of both the OLTC and SVR would be high [29]. It was shown that by controlling the reactive power output from the PV system, the number of scheduled tap changes in a given day can be reduced significantly.

SVRs are usually installed to regulate the voltage at the adjacent bus, or at the far end load bus by utilizing a line drop compensator (LDC). Instead of utilizing an LDC to estimate the voltage, a communication network based system is proposed that

communicates any bandwidth violations to the SVR controller to actuate a motor whenever necessary. A similar technique was utilized in previously published work to utilize remote bus measurements where either a maximum or minimum voltage is expected [30], [31]. The advantage of using a communication network for remote measurements is that it avoids unnecessary tap settings due to reverse power flow action caused by DGs even though there are a few economic implications. The rest of the section deals with the operation of SVRs with a DG accompanied by remote measurements.

A function $Activate(k)$ is triggered whenever the PV voltage, $V_j(k)$ goes beyond the bandwidth, BW as shown in (3.18). In this case, a higher bandwidth is assumed as the voltage variations are high at the PV bus due to high PV ramp rates. A lower bandwidth would keep triggering the $Activate(k)$ function frequently. The BW is set to 0.033 pu and set-point voltage, V_{set} is 1.01 pu in this case. All time samples are based on the k^{th} time step size. As soon as the voltage strays beyond the dead-band, a control timer starts with subintervals, $m \in \{1, 2, \dots, \tau_d/k\}$.

$$Activate(k) = \begin{cases} 1, & \text{if } (V_j(k) > V_{set} + 0.5 \cdot BW \text{ or } V_{UL}) \\ 0, & \text{otherwise} \\ -1, & \text{if } (V_j(k) < V_{set} - 0.5 \cdot BW \text{ or } V_{LL}) \end{cases} \quad (3.18)$$

When the function $Activate(k)$ is triggered, the signal is transferred to the time delay block of the SVR 1. The SVR closest to the substation (i.e. SVR 3) is set with the lowest time delay to respond first and regulate the voltages in the system. If SVR 3 is able to regulate the voltage at the critical bus, SVR 1 which covers the area where the PV system is located need not respond. The cascaded banks of regulators with a time-delay setting difference of at least 15 s between two consecutive regulators in series, is shown in

Figure 3.3. The actuation trigger time $t_{act}(k)$ for a motor drive marks the time instant t_x when the voltage crosses V_{UL} and then waits for τ_d and marks t_y when the taps need to change.

$$t_{act}(k) = \begin{cases} t_x, & \text{for } Activate(k+1) = 1 \text{ or } -1 \\ 0, & \text{for } Activate(k+1) = 0 \end{cases} \quad (3.19)$$

The tap variation, T_{SVR} for both upper voltage level, V_{UL} and lower level voltage, V_{LL} violation conditions is shown in (3.20). The step change occurs after the timer reaches the time delay mark of t_y .

$$T_{SVR}(mk+k) = \begin{cases} T_{SVR}(mk)+1, & \text{if } (t_y - t_x > \tau_d \text{ s}) \text{ and } (V_j > V_{UL}) \\ T_{SVR}(mk)-1, & \text{if } (t_y - t_x > \tau_d \text{ s}) \text{ and } (V_j < V_{LL}) \end{cases} \quad (3.20)$$

The SVR triggering action due to voltage violation above V_{UL} because of a high PV ramp-up output is shown in Figure 3.3. A similar action can be assumed for violation below V_{LL} due to a high PV ramp-down event.

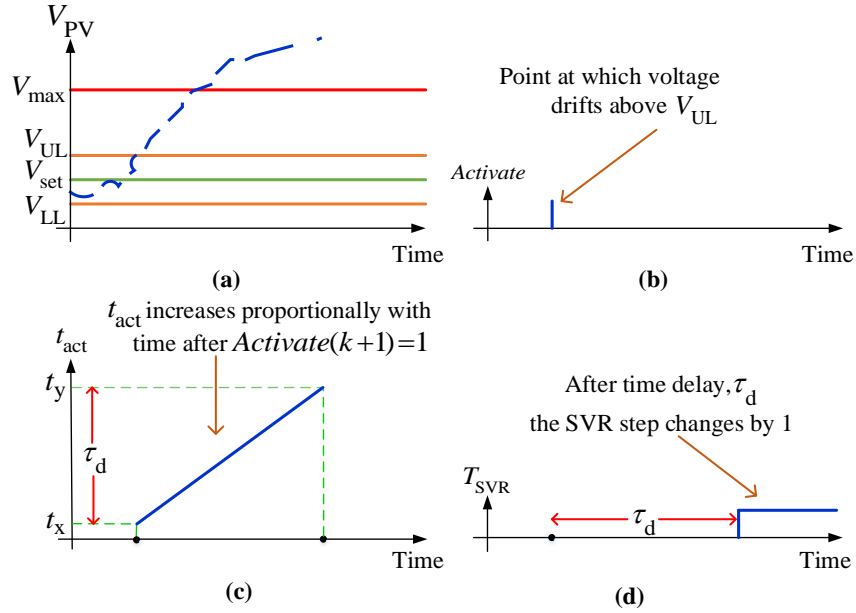


Figure 3.3: Tap operation condition (a) Voltage with bandwidth consideration (b) Activate signal activation (c) Actuation trigger time (d) Tap operation with time delay.

When there is a switching in a step voltage regulator, the information is transferred to the PV control database center to update the forward sweep coefficients as it affects the voltage change due to power injection. In the test system, the three single-phase Type B SVRs are connected in a closed delta as shown in Figure 3.4. The closed delta connection is typically used to balance the voltages due to unbalanced loading.

By applying Kirchhoff's voltage law around the closed loop, starting with the line-to-line voltage between phases A and B on the source side, the following equation (3.21) is obtained [28]:

$$V_{AB} + V_{Bb} + V_{ba} + V_{aA} = 0 \quad (3.21)$$

But as the individual terms in (3.21) can be rewritten as shown in (3.22), (3.23) and (3.24).

$$V_{Bb} = -\frac{N_2}{N_1} \cdot V_{bc} \quad (3.22)$$

$$V_{aA} = \frac{N_2}{N_1} \cdot V_{ab} \quad (3.23)$$

$$V_{ba} = -V_{ab} \quad (3.24)$$

Substituting (3.22), (3.23), (3.24) into (3.21) we obtain (3.25).

$$V_{AB} = \left(1 - \frac{N_2}{N_1}\right) \cdot V_{ab} + \frac{N_2}{N_1} \cdot V_{bc} = a_{Rab} \cdot V_{ab} + (1 - a_{Rbc}) \cdot V_{bc} \quad (3.25)$$

Other equation with reference to the line-to-line voltages can be obtained similarly.

The final three-phase equation in a matrix form is represented as shown in (3.26).

$$\begin{bmatrix} V_{AB} \\ V_{BC} \\ V_{CA} \end{bmatrix} = \begin{bmatrix} a_{Rab} & 1 - a_{Rbc} & 0 \\ 0 & a_{Rbc} & 1 - a_{Rca} \\ 1 - a_{Rab} & 0 & a_{Rca} \end{bmatrix} \cdot \begin{bmatrix} V_{ab} \\ V_{bc} \\ V_{ca} \end{bmatrix} \quad (3.26)$$

In a generalized form (3.26) can be written as **Error! Reference source not found.**

$$[VLL_{ABC}] = [a] \cdot [VLL_{abc}] + [b] \cdot [I_{abc}] \quad (3.27)$$

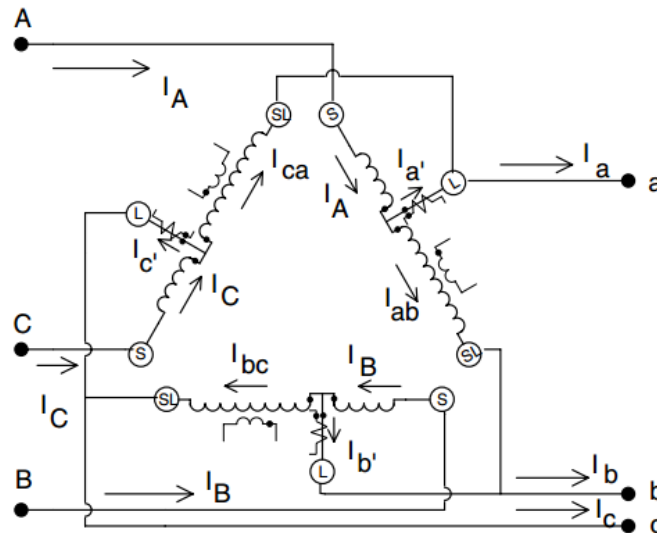


Figure 3.4: Closed delta-connected regulators [28].

3.3.3. Capacitor Bank Reactive Power Control

Capacitor banks are modeled similar to loads, in shunt with the line for each phase ($p \in a, b, c$) as shown in Figure 3.5. They inject reactive power, $Q_{cap,p}$ into the bus and can be controlled in steps, $\Delta Q_{cap,p}$ to control the reactive power injection. The step changes are similar to a step voltage regulator as discussed in section 3.3.2. where the voltage is measured at the local bus, $V_{cap,p}$ and based on a dead band operation either increases or decreases the number of units, $N_{cap,p}$ to switch on/off.

$$V_{cap,p} = X_{cap,p} I_{cap,p} \quad \forall p \quad (3.28)$$

$$jX_{cap,p} = j \frac{V_{cap,p}^2}{Q_{cap,p}} \quad \forall p \quad (3.29)$$

$$Q_{cap,p} = N_{cap,p} \Delta Q_{cap,p} \quad \forall p \quad (3.30)$$

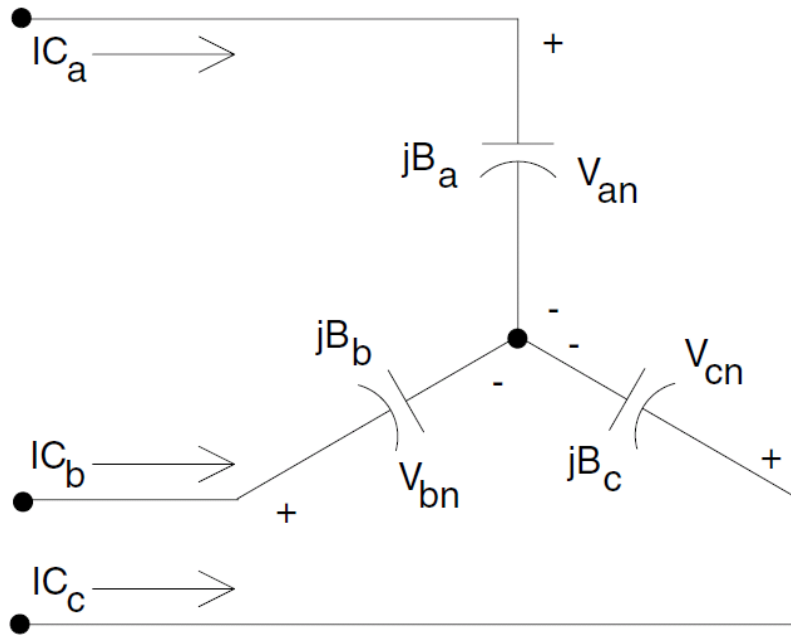


Figure 3.5: Capacitor bank model [28].

3.3.4. Inverter Reactive Power Control

The reactive power control is unnecessary until there is a voltage violation. As soon as the voltage at the PV terminal bus exceeds V_{UL} at the t_x time instant, the inverter begins to absorb reactive power. On the other hand, it starts to dissipate reactive power as soon as the voltage falls below V_{LL} . In order to limit the voltages within the ANSI standard limits (i.e. 0.95-1.05 pu), the desired rate of change based on the SVR 4 time delay τ_d plus a safety factor 10% of τ_d , $\Delta\tau_d$, is given by (3.31). As soon as the voltage strays beyond the dead-band, a reactive control timer starts with subintervals $m \in \{1, 2, \dots, \tau_d / k\}$.

$$\frac{\Delta V_q^c}{\Delta t} = \frac{V_{\max} - V_j(mk)}{\tau_d + \Delta\tau_d - mk} \quad (3.31)$$

By considering a high ramp PV output, P_{PV}^{mppt} with an MPPT based operation, the desired reactive power change ΔQ_{inv}^c is given by (3.32).

$$\frac{\Delta Q_{inv}^c}{\Delta t} = \left(\frac{\Delta V_q^c}{\Delta t} - \frac{\Delta P_{PV}^{mppt}}{\Delta t} \cdot \frac{\partial V_j}{\partial P_j} \right) \bigg/ \frac{\partial V_j}{\partial Q_j} \quad (3.32)$$

The reactive power support for small time steps is given by (3.33).

$$Q_{inv}^c(mk + k) = Q_{inv}^c(mk) + \frac{\Delta Q_{inv}^c}{\Delta t} \quad (3.33)$$

where $Q_{inv}^c(k)$ is the desired sample-based controlled reactive power output.

Ideally, the active power output of the inverter must be equal to P_{PV}^{mppt} for maximum benefit. It can be seen from (3.33), that the controlled reactive power support depends on the slope of the active power change with time, and the required reactive power support is

in the opposite direction, i.e., if the active power increases with positive slope, the reactive power support to mitigate the voltage rise must follow the active power with a negative slope. Power factor ($\cos \phi$) limits are applied at the inverter bus for reactive power limits, Q_{lim} . Figure 3.6 shows the reactive power capability of an inverter. In the Figure 3.6, $Q_{ainv}(k)$ is the available reactive power at the k^{th} time instant.

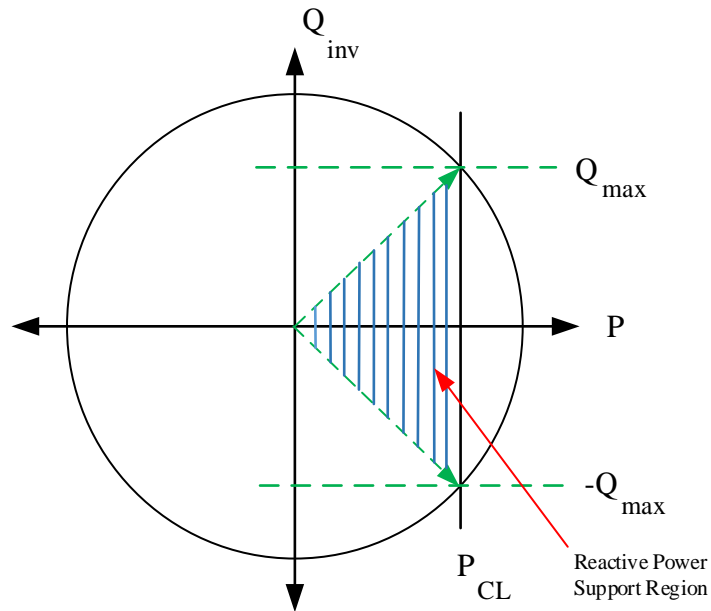


Figure 3.6: Reactive power capability of the inverter.

3.3.5. Inverter Active Power Control

In [14], an online overvoltage prevention scheme was introduced to reduce the voltage at the point of interconnection during both clear and cloudy conditions by curtailing active power from the PV.

Active power curtailment might be required in case of high ramp output due to cloud passing. For curtailment of active power, energy storage is utilized. The advantage of using a battery to slow down the increment in PV generation with a time window is to allow the voltage regulating devices to react in time.

In this work the PV and storage device are connected in parallel to the DC link capacitor of the three-phase inverter. The PV is connected through a boost converter and the energy storage devices i.e., battery and supercapacitor are connected through two separate dc-dc buck-boost converters, so that when they are charging, the converter acts in the buck mode, and when discharging the converter acts in the boost mode. There are three separate controllers for the three converters [29].

The minimum time required to delay the increase in voltage from V_{LL} to V_{max} should be more than the time delay setting of the SVR to make a change in the tap settings. Therefore it is important to estimate the time it takes to reach V_{max} from the time V_{UL} is reached. It is a fair assumption to consider that the voltage at the PV terminals, V_j , is proportional to the active power changes as shown in Figure. 3.7. The variation of V_j with active power change following the PV plant MPP, P_{PV}^{mpp} for a time step is given by (3.34) [32].

$$\frac{\Delta V_p^c}{\Delta t} = \frac{\Delta P_{inv}}{\Delta t} \cdot \frac{\partial V_j}{\partial P_j} \quad (3.34)$$

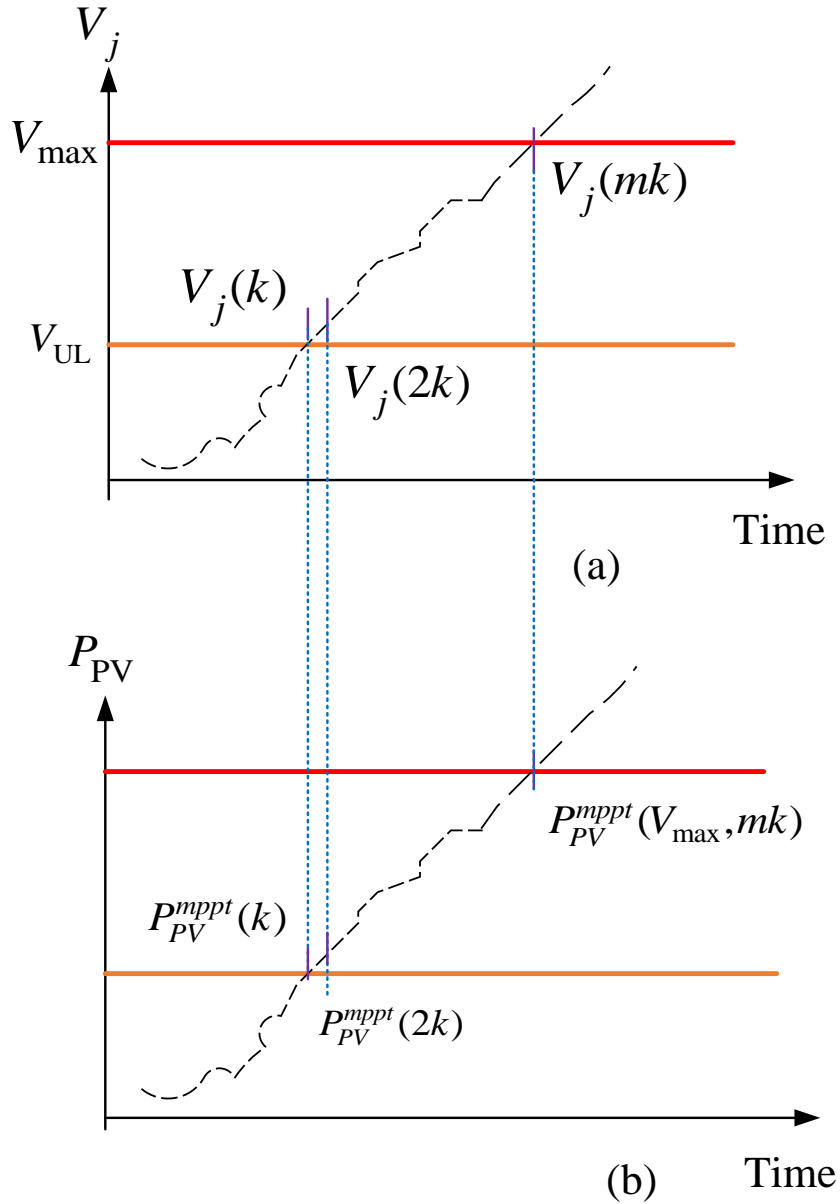


Figure. 3.7: Voltage dependence on active power output at the PV bus (a) Voltage (b) PV active power output.

The active power at the point where V_{\max} occurs can be estimated in real time by applying an online estimation technique. To estimate this point, i.e., $P_{PV,est}^{m ppt}(V_{\max}, k)$, calculations can be made by assuming a droop characteristic between V_j and $P_{PV}^{m ppt}$, as (3.35).

$$P_{PV,est}^{mpp} (V_{\max}, k) = P_{PV}^{mpp} (k) + (V_{\max} - V_{PV}(k)) \frac{\partial P_{PV}^{mpp} (k)}{\partial V_{PV}(k)} \quad (3.35)$$

If the DG inverter output is based on P_{PV}^{mpp} , the time Δx to reach V_{\max} is given by (3.36).

$$\begin{aligned} \frac{V_{\max} - V_j(mk)}{\Delta x} &= \frac{\partial V_j}{\partial P_j} \cdot \frac{\Delta P_{PV}^{mpp}}{\Delta t} \\ \Delta x &= \frac{V_{\max} - V_j(mk)}{\frac{\partial V_j}{\partial P_j} \frac{\Delta P_{PV}^{mpp}}{\Delta t}} \end{aligned} \quad (3.36)$$

If Δx is more than the time delay τ_d of the SVR, then the voltage regulation is left for the SVR 4, but in case Δt is less than the time delay τ_d , the scaling factor is adjusted to Ω , where Ω is a function of the current state of charge (SOC) of the battery. The inverter follows the slope from the time instant, t_x , the point at which the PV system terminal voltage exceeds the upper limit, i.e., $V_j > V_{UL}$.

As the time duration for a high-rate ramping is small, the amount of power to be used for ramp-rate control is high for the short duration which cannot be taken care of by a battery system all the time. Among different kinds of batteries with different chemistries, vanadium redox batteries (VRB) are the most suitable for PV operation as they have a slow chemical aging process which increases its service life. It could also be scaled for high scale PV penetration due to the independence between its energy and power ratings [33].

The controlled inverter power output, P_{inv} is given by (3.37).

$$P_{inv}^c (mk) = P_{Bat} (mk) + P_{PV}^{mpp} (mk) \quad (3.37)$$

P_{Bat} is the power support provided by the battery energy storage system (BESS). The controlled inverter output ΔP_{inv}^c is given by (3.38) and (3.39).

$$\frac{\Delta P_{inv}^c}{\Delta t} = \frac{P_{PV,est}^{mpp} (V_{max}, mk) - P_{PV}^{mpp} (mk)}{\Omega(mk) - mk} \quad (3.38)$$

$$P_{inv}^c (mk + k) = P_{inv}^c (mk) + \frac{\Delta P_{inv}^c}{\Delta t} \quad (3.39)$$

The equation for ramp rate control scaling factor can be explained by Figure. 3.8 for both charging and discharging cases. The scaling factor Ω at any time instant is given by (3.40).

$$\Omega(mk) = (\tau_d + \Delta\tau_d) - \Delta\tau_d \cdot \frac{SOC_{act}^{Bat}(k) - SOC_{min}}{SOC_{max} - SOC_{min}} \quad (3.40)$$

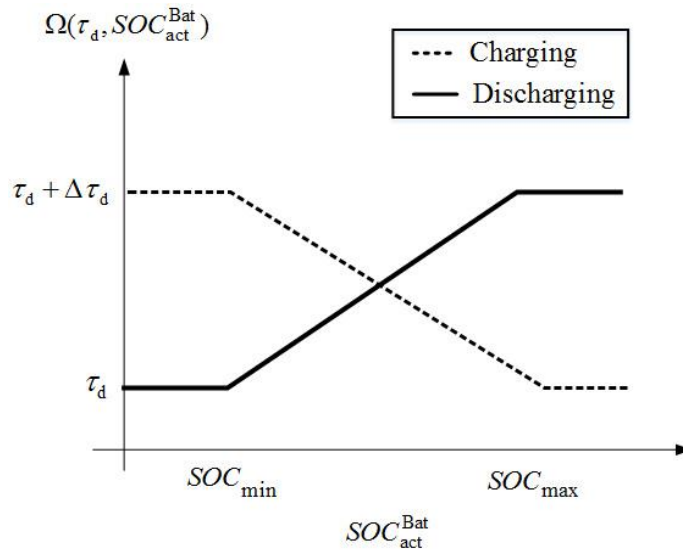


Figure. 3.8: Scaling factor estimation based on SoC of battery and supercapacitor.

In the case of charging, if SOC_{act}^{Bat} is low, the PV system can be ramped-up at a lower rate; similarly if SOC_{act}^{Bat} is high, the PV system can be ramped-down at a lower rate.

The SVR, in this case, is controlled based on a local distributed communication actuator signal which controls the motor for step changes. The dead-band comparator

receives signals from the PV bus that is connected with a smart meter. The controller sends signals to the time delay controller as well as the PV inverter to begin controlling active and reactive powers based on the algorithm discussed above. After the active power output of the inverter is determined, the required change in reactive power is given by (3.41) and (3.42).

$$\frac{\Delta Q_{inv}^c}{\Delta t} = \left(\frac{\Delta V_q^c}{\Delta t} - \frac{\Delta P_{inv}^c}{\Delta t} \cdot \frac{\partial V_j}{\partial P_j} \right) \bigg/ \frac{\partial V_j}{\partial Q_j} \quad (3.41)$$

$$Q_{inv}^c(mk + k) = Q_{inv}^c(mk) + \frac{\Delta Q_{inv}^c}{\Delta t} \quad (3.42)$$

The configuration of PV connected in parallel with a battery at the DC link of an inverter is shown in Figure 3.9. The PV is connect to the DC link through a boost converter which maintains the PV array DC voltage, V_{PV} at the maximum power point (MPP) to produce DC power, P_{PV} . The battery is connect to the DC link through a buck-boost converter which perform the action of charging or discharging the battery based on the inverter output requirement. The battery supplies the difference, P_{Bat} between the inverter command, P_{inv} and the MPP output of the PV, P_{PV} .

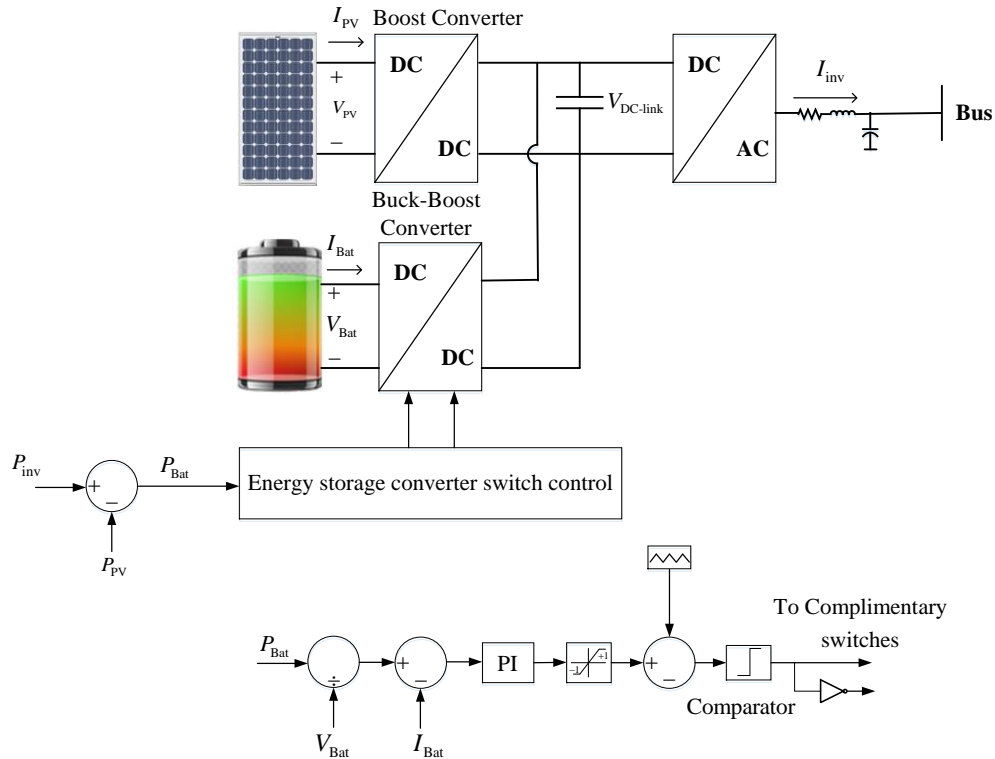


Figure 3.9: (a) Voltage-based droop control for inverter interfaced source (b) Voltage-based droop control for synchronous based generators.

3.4. Overall Control and Coordination Scheme

In accordance with the utility's operating rules, it is preferred that the SVR closest to the substation have the lowest time-delay. For example, the first series SVR from the substation, SVR 2 would have a 45 seconds delay, the second SVR (downstream direction), SVR 3 would have a 1 minute delay, and the third SVR, SVR 4 would have a 75 seconds delay. By setting the time delay of the line regulator higher than that of the substation bank, the substation bank responds first and regulates the voltage to its best ability. If the substation regulation is insufficient, then the downstream line regulators (SVRs) will need to operate. The suggested minimum time-delay difference between banks of line regulators is 15 seconds. The SVR 4, in this case, is controlled based on a local distributed communication actuator signal which controls the motor for step changes as shown in Figure. 3.10. The dead-band comparator receives signals from the

PV bus that is connected to a smart meter. The controller sends signals to the time delay controller as well as the PV inverter to begin controlling active and reactive powers based on the algorithm discussed previously. The target node for SVR 4, i.e. node 117, is far away. The voltage at bus 99, V_{bus99} can be measured locally on the secondary side of the SVR. The load bus currents I_{L_n} (where $n = 1, 2, 3, \dots, \text{and } 117$) can be estimated using state estimation and forecasting techniques. The line impedance Z_n are constants and can be obtained using characteristics and length of the lines between two buses. Using (3.43), the target bus voltage, V_{bus117} / V_j can be estimated to make the necessary changes. But with high variations of large scale PV, it becomes difficult to estimate the load currents, thus failing to properly estimate the target bus voltage, $V_{\text{bus117,est}}$. The problem can be solved by sending real time load currents directly to the LDC or using a smart meter to send the real time voltage at the inverter node directly to the dead band comparator using a communication network. The latter solution is more accurate and cost-effective, especially for the real time voltage regulation scheme using a smart inverter and conventional voltage regulating devices.

$$V_{\text{bus117,est}} = V_{\text{bus99}} - Z_{99} \cdot I_{L100} - (Z_{99} + Z_{100}) \cdot I_{L100} \dots - (Z_{99} + Z_{100} \dots + Z_{117}) \cdot (I_{L117} + I_{\text{inv}}) \quad (3.43)$$

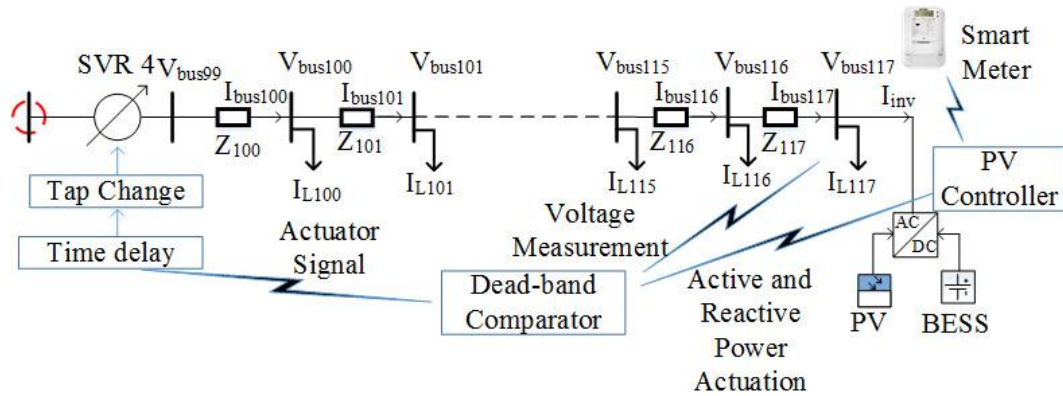


Figure. 3.10: Coordinated distributed control between SVR and the PV system for voltage control.

The SCB at Bus 68 of the feeder is a combination of shunt capacitor units that can be switched on or off based on the voltage bandwidth similar to an SVR. The SCB is composed of two capacitor units that can be switched on/off individually in a discrete manner with increments/decrements based on time delays and voltage levels. Based on a control logic similar to an SVR controller, a counter for time delay is introduced to close the capacitor units when the target bus voltage is below the low-voltage threshold and conversely begins a counter to trip energized capacitor banks when the target bus voltage is above the high-voltage threshold. During high PV penetration and low loading conditions, the voltages could drift above the upper limit threshold, causing the capacitor units to trip discretely in steps until the voltage at its target bus is within the dead band. The overall flowchart of the proposed distributed voltage control strategy is shown in Figure 3.11. In order to perform the proposed distributed voltage control algorithm in practice, there would be a requirement of only two control centers, one at the PV farm/plant and the other at the SVR 4 location, which coordinates with the inverter control center through a bi-directional communication link. Within the PV farm/plant control center, there would be a requirement of a data archival system to measure PV

farm maximum power point outputs and the current state of the battery, smart meter at the grid integration terminals and weather sensors. Besides the bidirectional communication link, there is a requirement for unidirectional communicational links to transfer the information of any switching operations of the rest of the regulating devices on the feeder to the PV farm/plant control center to account for the system changes on the network, which in turn affects the sensitivity of the voltage change due to power injection at the PV farm.

To improve the robustness of the system against a communication failure, two scenarios could be implemented with the distributed voltage control algorithm. The majority of substation devices in a distribution utility network are telemetered. The SCADA system primarily relies on circuit breaker relaying and reclosers to provide current, voltage, active and reactive power information. These devices provide the majority of the data points to calculate power flow on the system. They also have line sensors with wireless telemetry on feeders where reclosers are not telemetered. They obtain On-Load Tap Changers (OLTCs) and voltage regulator current tap setting and their high side/load side voltage and current readings through SCADA telemetry. To summarize, utilities now have multiple levels of communication: SCADA telemetry, wireless (e.g., 3G/GPRS), Advanced Metering Infrastructure (AMI), etc. to improve the robustness of the system against communication failure.

Alternatively, in case there is no backup communication layer, the local controller at the PV system could operate the inverter based on the sensitivity analysis and local measurements. As the dead-band controller loses its communication capability to convey the PV plant voltage signals along with the dead-band range information, the SVR 4

devices in Matlab/Simulink environment. In the DVC scheme, the regulating devices considered are the smart inverter with reactive power capability, active power control based on energy storage control and a tap changing SVR. In these case studies, the aim is to observe the power quality effects due to the PV output and the comparison of the three cases in mitigating the power quality issues on the feeder. Observations are made for the ANSI C84.1 standards and the voltage fluctuations at the PV system terminals. A realistic PV output profile was used in this study for a cloudy period. The loads are mainly commercial and residential [15]. The total time for simulation is 1000 seconds to observe the tap changes for this extreme case when 3 high ramp rate changes occur, and the loads are 75-80% of the base values in the feeder. This is typical when the clouds have completely covered the solar array and after a short period of time moves away to expose a clear sky for high solar irradiance. Studies have shown that at 2 sites in California, PV ramp rates of 75% and 93% of their rating/minute were observed [34]. Even though the cloud movement is quick, which causes the irradiance to fall rather quickly, the area covered by the PV plant is quite large. After the high ramp rate events, there were short periods considered when the power variations were not high for a certain time period. These high ramp rate events are quite abnormal and do not occur frequently in a year.

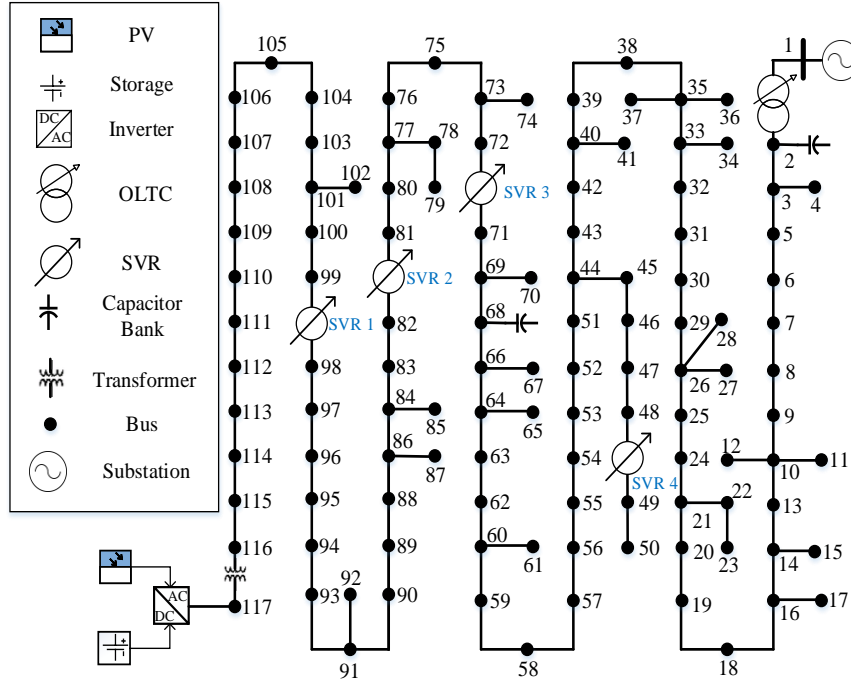


Figure 3.12: MV feeder located in a California utility.

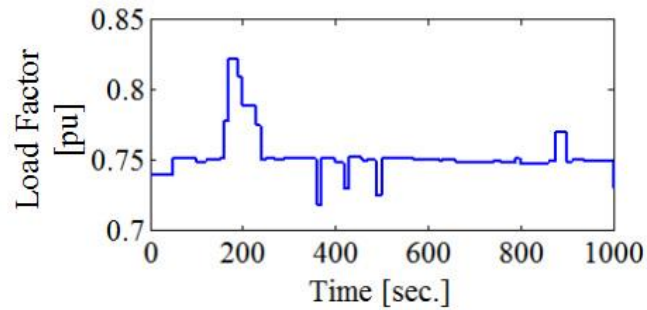


Figure 3.13: Cumulative load factor variation with time.

For Case I, the inverter supplies power to the grid based on the maximum power point (MPP) of the PV array while operating at unity power factor (upf). The output of the inverter when operating at upf is shown in Figure 3.14 (a). The PV power at the terminals continues to vary with time. From around time $t = 50$ s to $t = 150$ s, a high ramp-up even occurs and remains steady with lesser ramp until around time $t = 380$ s. From around $t = 380$ s to $t = 480$ s, the power falls from almost its rated value to almost zero, causing a high ramp-down event. Again, from time $t = 710$ s to $t = 790$ s, a high ramp up of PV power output occurs and remains steady thereafter. These high variations cause the

voltages at the PV system terminals to vary quite significantly. It is observed that three phase voltages have drifted above the maximum voltage limit (i.e. 1.05 pu) of the ANSI C84.1 standard for the first time at around $t = 100$ s. For the remaining period of the simulation, the voltages for phases A, B, and C have drifted above 1.05 pu for quite a long period of time on several occasions. The step voltage regulators were not able to bring the voltage back to its safe band due to the fast variation of PV output. The high variations in voltages can be observed in Figure 3.14 (b). The SCB switch on/off status are shown in Figure 3.14 (c). The SCB units switched off due to high voltages at the SCB bus terminals due to high PV injection and lower loading conditions. The tap changes for the three SVRs in line with the PV system are shown in Figure 3.14 (d), (e) and (f). SVR 4 is the closest to the PV system; hence it comes under the zone of SVR 4 regulation. SVR 2 and SVR 3 are in line with the PV system and regulate the voltages at their terminals. Due to the high scale PV penetration, the change in PV output affects the voltage at the terminals of SVRs 2 and 3. This can cause the SVRs to change the taps to bring the voltage within the safe band. The total number of SVR operations is given in Table 3.1 for Case I. From the simulations in Case I, it can be observed that simply depending on static conventional voltage regulating devices to regulate the voltage due to high PV penetration is unreliable. The voltage could not be maintained within the safe band and the number of tap operations was also significantly high.

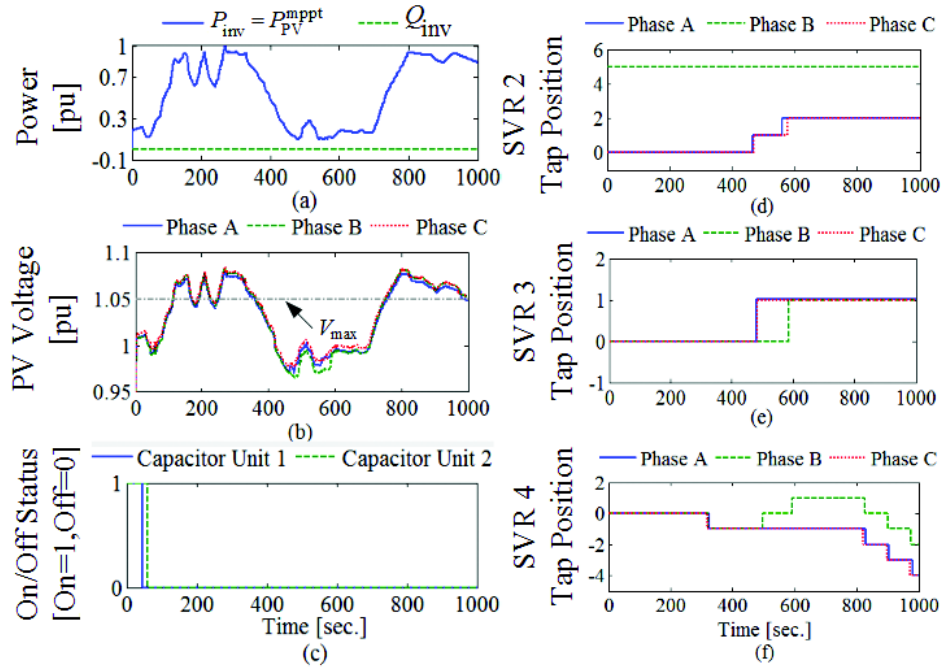


Figure 3.14: Feeder results for Case I (a) PV system power outputs, (b) PV terminals voltage, (c) SCB units switch on/off status, (d) SVR 2 tap positions, (e) SVR 3 tap positions and (f) SVR 4 tap positions.

Table 3.1: Total number of SVRs taps operations for case I

SVR 2	SVR 3	SVR 4
4	3	14

For Case II, the inverter supplies power to the grid based on the maximum power point (MPP) of the PV array while the reactive power support from the inverter is applied. The reactive power operation is discussed in Section II. The sharp increase/decrease in active power output is countered equally by the sharp reactive power absorption/supply. The power outputs of the inverter when operating with variable reactive power support for ramp rate control is shown in Figure 3.15 (a). The voltages at the PV system terminals are shown in Figure 3.15 (b). It can be observed that the voltages have been restricted significantly, but was not enough to limit the voltage below the V_{\max} limit. The voltage drifted above V_{\max} for about 70 seconds starting from time $t = 110$ s to $t = 180$ s approximately and again from time $t = 750$ s to $t = 810$ s. The reactive power as discussed

previously is based on a power factor limit and the available active power. The rise and drop in voltage due to high variations could not be controlled significantly which led to high voltage variations. The SCB unit switch on/off status are shown in Figure 3.15 (c). The number of tap changes was reduced significantly as compared to that in Case I as the voltage was controlled by reactive power support from the inverter when necessary as shown in Figure 3.15 (d), (e) and (f). Table 3.2 gives a summary of the total number of tap changes over the simulation time period.

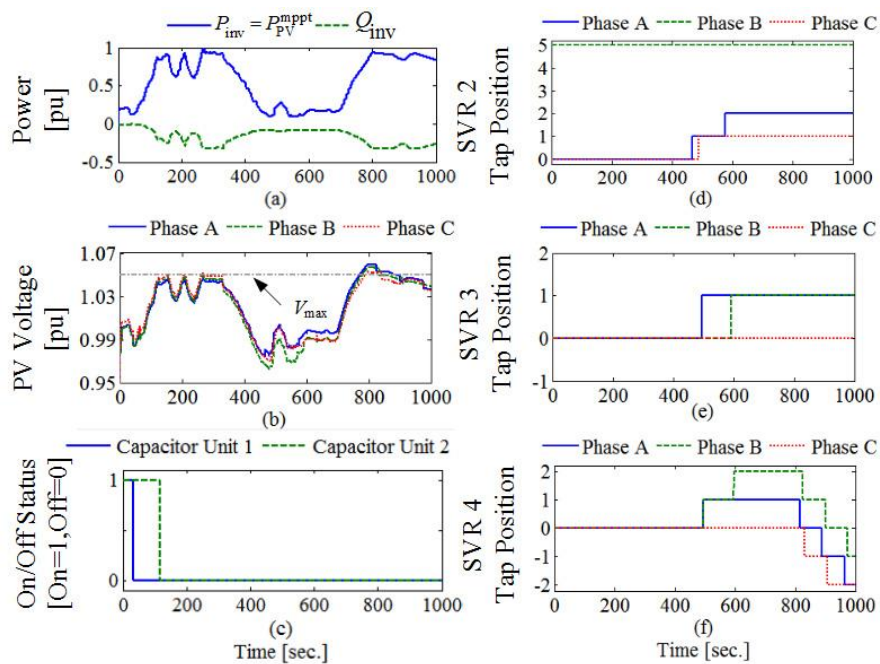


Figure 3.15: Feeder results for Case II (a) PV system power outputs, (b) PV terminals voltage, (c) SCB units switch on/off status, (d) SVR 2 tap positions, (e) SVR 3 tap positions and (f) SVR 4 tap positions.

Table 3.2 Total number of SVRs taps operations for case II

SVR 2	SVR 3	SVR 4
3	3	11

For Case III, both active and reactive powers from the inverter were controlled. The reactive power support is the same as above, but the active power control was performed as discussed in Section II. The active power was controlled by utilizing a BESS

connected in parallel to the DC link of the inverter. It could be observed during high ramp-up case that the active power from the inverter was controlled, compared to the available PV array output. The BESS was able to absorb the excess energy during this period beginning from the instant when the voltages at the PV terminals went above V_{UL} . During the high ramp-down case, in order to slow the ramping down process, the BESS needed to discharge when the voltage went below V_{LL} . The output of the inverter when operating with variable reactive power support for ramp rate control and active power control based on the discussions in Section II is shown in Figure 3.16(a). The power absorbed and supplied by the BESS is shown in Figure 3.16(b). The state of charge comparison is shown in Figure 3.16(c). It is observed that during high ramp rate conditions, the BESS is utilized significantly. For higher SOC_{act}^{Bat} , which indicates higher usage of BESS, the scaling factor Ω is adjusted to reduce the charging of the battery. This leads to reduced cycle of operation for the battery and avoiding high depth of charge/discharge regions. From Figure 3.16(d), it can be observed that the voltages were maintained within the ANSI C84.1 standards throughout the simulation period and the high variations in voltage were suppressed as a result of active and reactive power control of the inverter when compared with just the reactive power support in Case II. The SCB unit switch on/off status are shown in Figure 3.16(e). The total number of tap changes over the simulation period was reduced compared to Cases I and II as shown in Figure 3.16(f), (g) and (h). Due to active power curtailment, the extent of voltage violations in the ADN is reduced which causes the SVR 4 tap changes to reduce significantly. The total number of tap change operations for Case III is shown in Table 1.1. The number of tap changes is less than that for Cases I and II.

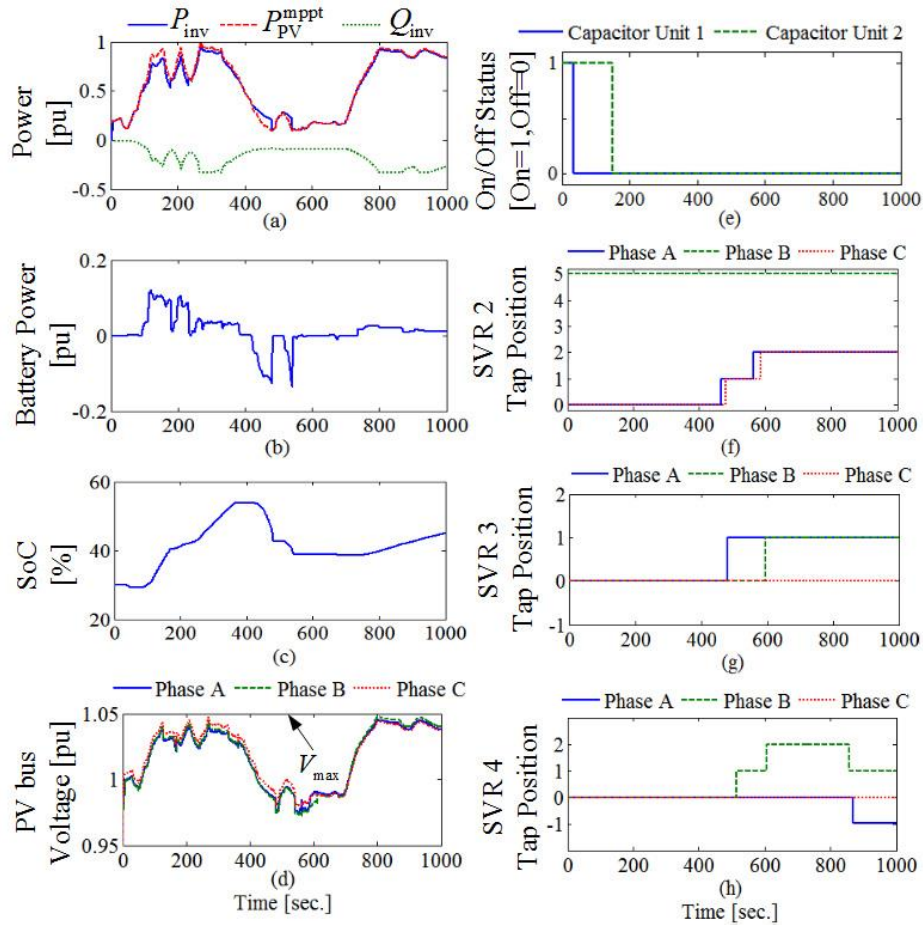


Figure 3.16: Feeder results for Case III (a) PV system power outputs, (b) Battery output, (c) Battery SoC, (d) PV terminals voltage, (e) SCB units switch on/off status, (f) SVR 2 tap positions, (g) SVR 3 tap positions and (h) SVR 4 tap positions.

Table 3.3 Total number of SVRs taps operations for case III

SVR 2	SVR 3	SVR 4
4	2	4

3.6. Summary

In this chapter, a smart distributed voltage control strategy for high scale PV penetration is discussed, especially during cloud transient movement. The high ramp-rate event requires a fast and appropriate level of action from a dynamic regulating device. In this work, the smart inverter is responsible for the control action by communicating with the existing passive regulating devices. There are three different case studies performed

to highlight the benefits of the proposed method. All simulation cases were performed in a MATLAB/Simulink environment which is based on the time domain analysis. For Case I, the PV system is allowed to operate at its MPP while operating at upf. The only regulating devices are the passive SVRs and a SCB that operate with time delays. The power quality standards being observed here are the ANSI C84.1 limits and the voltage fluctuations. The first case proved insufficient to tackle the power quality issues emerging from the high scale PV penetration for the cloud transient movement along with increasing the number of SVR operations. For Case II, the high ramp rate PV output was utilized to develop a fast reactive power support. This proved a far better solution for voltage support, voltage rise mitigation, and fluctuation, but could not stop the phase voltage from drifting above the ANSI C84.1 standards and solving the high voltage fluctuations. The reason is attributed to the high R/X ratios of the lines in the distribution system which prevented the reactive power support from properly regulating the voltages within the required band. For Case III, the active power control from the smart inverter was added to the reactive power support for mitigating the voltage rise and fall due to the high ramp output from the PV. In order to absorb and supply the imbalance of the required PV inverter output and the PV array output, a BESS is utilized. A weighted mean of the current state of charge of the battery dictated the length of the controlled ramp output from the inverter. The coordinated strategy between the smart inverter and the existing regulating devices proves to be an effective solution to maintain good power quality as well as minimize the tap operations that increases its lifetime service operation. It proved to be the best solution for voltage support, voltage rise mitigation, and

fluctuation reduction along with best practice to minimize the overall tap changes during the simulation period.

CHAPTER 4 : OPTIMAL VOLTAGE REGULATION OF DISTRIBUTION NETWORKS WITH CASCADED VOLTAGE REGULATORS IN THE PRESENCE OF HIGH PV PENETRATION

4.1. Introduction

This work proposes a zone based multistage time graded operation of the cascaded load-tap changing (LTC) transformers and capacitor banks (CBs) in the presence of large scale photovoltaic (PV) source. The objective of the suggested centralized optimization algorithm is to regulate the voltage in a medium voltage (MV) unbalanced distribution system while trying to relax the tap operations of voltage regulators that are cascaded in series and minimize the curtailment of PV when necessary. A technique for changing Mixed-integer nonlinear programming (MINLP) to nonlinear programming (NLP) and then to binary-MINLP optimization is suggested to meet the different objectives at successive stages. The first stage is associated with the on-load tap changing (OLTC) transformer taps and capacitor bank operations. The second, third and fourth stages deal with the step voltage regulator (SVR) operations in their respective zones. A week long simulation was performed for various scenarios of PV and load profile variations. High scale PV integration is gaining popularity in the US due to the stringent renewable portfolio standards dictated by a few states. High scale PV act as distributed generation (DG) in the grid and negatively affect the regular operation of the grid and its devices. One of the significant issues caused by these high scale PV generators are the over-voltage issues at the nodes near the PV integration sites, voltage unbalance and flicker.

Flicker has drastic effects on loads that are sensitive to voltage variations which could causes monetary losses. These large scale PV generators have economic implications too as they cause over usage of regulating devices that reduces their lifetime of operation. Voltage dependent loads start consuming excess power that has a drastic impact on the conservation voltage reduction (CVR) factors which is being implemented in many utilities. Many works have suggested overvoltage mitigation techniques based on either centralized or center-free techniques that deal with Volt/VAr control techniques.

4.2. Literature Review

In [35], a distributed control method based on a cooperative control scheme between the DG and LTC agent is suggested to achieve the best compromise between global and self-objectives. For voltage regulation the DG agent participates in reactive power control as well as active power curtailment while LTC agent aims at meeting the global objective of minimizing the voltage deviation as well as meet its self-objective of reducing its tap operations. In [26], a distributed control method is suggested with full autonomy and independence to its control agents while being aware of meeting the global objective of voltage regulation. In this scheme the optimal arrangement of OLTC and SVRs is suggested in the presence of high scale PV penetration. In [36], a hierarchical zoning based Volt/VAR scheme is proposed for optimal usage of voltage regulating devices and better data handling. As the decentralized zones have separate voltage regulating capabilities they coordinate with others to meet the grid-wide solution. The DG regulation scheme only makes use of the reactive support. Voltage sensitivity matrix has been found to be useful while implementing many decentralized voltage control [37].

Centralized control schemes can be divided into model based and model free. Model based mostly utilize the optimization objectives to meet the global goals utilizing the system model parameters and constraints to send set-points to the devices in the system through one-way communications. In [38], an ϵ decomposition method is introduced for voltage regulation by utilizing the network sensitivity matrix for a heavily meshed secondary network distribution systems with high PV penetration. To deal with PV day ahead planning, a centralized optimization to maintain the voltage within acceptable level can be implemented on hourly forecasted PV and load profiles. In [39], the number of tap changes for a day are reduced by using the reactive power support from PV inverters but does not consider the active power curtailment as the size of the PV is relatively smaller and lesser R/X ratios for the lines are considered. OLTCs, substation and feeder capacitors were coordinated with each other to meet the voltage constraints and thus minimizing the total OLTC tap changes in the presence of high DG penetration. In [40], the DGs were made to operate either at constant power factor, constant reactive power support or constant voltage to test the coordination. In [41], the coordinated control between OLTC and static VAR compensator (SVC) for voltage regulation in an unbalanced distribution system was introduced while trying to minimize the tap and SVC operations using a centralized optimization operation. In this work the smart inverter functionality is suggested along with the SVR based on a separate communication layer. Rogers et al. recognized the increase of power electronics interfaced energy resources on residential voltage levels and the possibility to use these for reactive power support to mitigate voltage collapses. A centralized management of the resources was proposed, but this management was also identified as the main challenge as the complexity increases

with the number of devices [42]. In [43], reactive power support from the DGs is utilized to perform voltage regulation, phase imbalance correction and power flow by utilizing sequential convex programming (SCP).

The issue with reactive power support from the DGs is heavily dependence on the network characteristics. In case the X/R ratio of the network is low, the active power flow in the reverse direction causes a higher voltage drop in the opposite direction causing the voltage to go higher than the ANSI C84.1 standards [17]. A comprehensive and accurate modeling of the distribution system is developed in this work. In [44], an active power curtailment is considered. The objective is to minimize the power curtailment of DG which helps relaxing the voltage constraints. Due to the comprehensive modeling of devices and the increased in complexity the number of iterations to arrive to an optimized solution takes time due to the single layer of optimization. In [45], a real time optimal voltage regulation in a balanced distribution system using multistage operation is discussed. Both PV and plug-in electric vehicle combinations are considered and scheduled to meet the multi-objectives in successive stages. In this work however the unbalanced nature of the distribution network is not considered. The network is not big enough to take into consideration the several voltage regulating devices that are in reality based on a time-graded operation and need to co-ordinate properly to meet several objectives in the grid. The motivation behind this study is to suggest a superior solution for PV-related voltage regulation issues as compared to the existing solutions specifically for regulators that are cascaded in series with each other and time-graded devices that cannot be controlled once as Mitigation of voltage unbalance using optimal control of PV inverter active and reactive power was proposed in. In [46], the voltage unbalanced and

magnitude management was dealt with for an unbalanced system with high scale integration of single phase PV using an aggregated single-objective OPF methodology.

4.3. Theory and Proposed Solution

In this work a zone based centralized Volt/VAR optimization technique is proposed by breaking the distribution feeder into several zones and operating in a hierarchical scheme. The zone based centralized optimization scheme ensures reduction of complexity and minimize the use of the regulators due to similar voltage patterns in the feeder due to high PV penetration. By adaptively controlling a regulator in one zone the voltage reduction in other zones could be ensured. In order to co-ordination between cascading banks of regulators that are connected in series along the line, a time delay of at least 15 sec is maintained between them to eliminates unnecessary hunting [47]. The distribution system used for the study is an unbalanced medium voltage (MV) feeder located in a California utility service territory with high PV integrated with 4 zones based on territory controlled by the SVR. SVRs 2, 3 and 4 are in line with PV. A centralized optimization controller that is dictated by the DMS is utilized in this work to schedule the various regulating devices in the MV system. It allows only one way communications that set the regulating devices so as to maintain a stable voltage within the required standards.

4.3.1. Objective Functions

The optimization is performed centrally to schedule the various regulating devices present in the MV system. The objective is to minimize the active power curtailment, tap and capacitor bank deviation from the previous position as much as possible. The various

regulating devices present within the MV system are time graded to meet their respective objectives. The various objective functions are given below.

The first and second sub-objectives are associated with the tap changes for the OLTC and cascaded SVRs between consecutive intervals as given in (4.1) and (4.2).

$$J_{TOLTC} = \sum_{h=1}^{h^{\max}} |Tap_{OLTC}(h) - Tap_{OLTC}(h-1)| \quad (4.1)$$

$$J_{TcSVRg} = \sum_{h=1}^{h^{\max}} \sum_{p=a}^c |Tap_{cSVRg}^p(h) - Tap_{cSVRg}^p(h-1)| \quad \forall g \quad (4.2)$$

where J_{TOLTC} / J_{TcSVRg} is the objective function for OLTC/cSVRg tap changes, Tap_{OLTC} / Tap_{cSVRg} is the tap position of OLTC/cSVRg, the cascaded SVR index is given by $g \in 1, 2, \dots, n$ for total number of cascaded SVRs n , phase index is represented by $p \in a, b, c$, hours index $h=0, 1, 2, \dots, h^{\max}$ for maximum hours for optimization run h^{\max} .

The third sub-objective J_{NCap} is associated with the total number of capacitors switched on in the capacitor bank between consecutive hours as shown in (4.3)

$$J_{NCap} = \sum_{h=1}^{h^{\max}} |N_{Cap}^p(h) - N_{Cap}^p(h-1)| \quad (4.3)$$

where J_{NCap} is the objective function for switched capacitor banks, N_{Cap} is the number of capacitor units switched on in a capacitor bank.

The fourth sub-objective J_{cur} is associated with the curtailment of active power from the PV output as shown in (4.4).

$$J_{Pcur} = \sum_{h=1}^{h^{\max}} P_{curt}(h) \quad (4.4)$$

where P_{curt} is the curtailed active power output from PV.

4.3.2. Inequality and Equality Constraints

The constraints for the objective functions are for the voltage at each bus, tap positions, tap changes at each time interval, number of capacitor banks switched between each interval, active and reactive power output from the inverter.

Power Flow : In order to perform three-phase un-balanced distribution optimal power flow the series components as shown in Figure 4.1, such as the conductors/cables, transformers, LTCs are modeled as ABCD parameters [28]. The relationship between sending and receiving end voltages and currents is given by (4.5).

$$\begin{bmatrix} \bar{V}_s \\ \bar{I}_s \end{bmatrix} = \begin{bmatrix} A & B \\ C & D \end{bmatrix} \begin{bmatrix} \bar{V}_r \\ \bar{I}_r \end{bmatrix} \quad (4.5)$$

where \bar{V} is the three phase voltages vector and \bar{I} is the three phase currents vector, r is the receiving end node index and s is the sending end node index.

Based on Kirchhoff's law, the current injection balance at each node for each phase is given by (4.6).

$$\sum_l I_{l,r_i}^p = \sum_l I_{l,s_i}^p + \sum_L I_{L_i}^p - \sum_C I_{C_i}^p \quad \forall p, \forall i \quad (4.6)$$

where i is the node/bus index, I^p is the line current phasor, L is the set of loads, $L=1,2,\dots,NL$ for total loads NL , l is the set of series line elements, $l=1,2,\dots,Nl$ for total number of series elements Nl and C is the set of controllable capacitor banks, $C=1, 2,\dots, NC$ for total controllable capacitor banks NC .

Any element that is connected to a node has the same voltage as the bus to which it is tied as shown in (4.7). The nodal voltages are the variables that apply to the power

balance equations. The Power balance at each node for Y-connected loads and generation is given by (4.8).

$$V_{l,r_i}^p = V_{l,s_i}^p = V_{L_i}^p = V_{C_i}^p = V_i^p \quad \forall p, \forall i \quad (4.7)$$

$$V_i^p (I_i^p)^* = (P_{L_i}^p + jQ_{L_i}^p) - (P_{G_i}^p + jQ_{G_i}^p) \quad \forall p, \forall i \quad (4.8)$$

where V^p is the line voltage phasor, P_L is the active power load, Q_L is the reactive power load, P_G is the active power generation and Q_G is the reactive power generation.

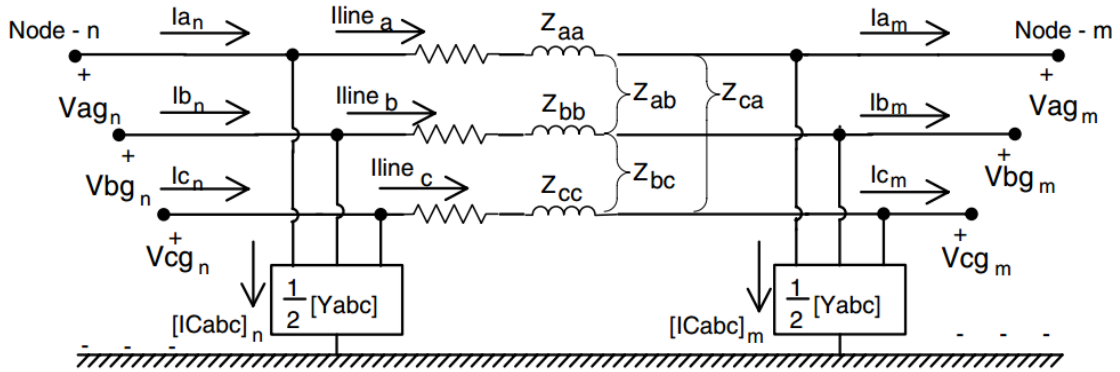


Figure 4.1: Three-phase line segment model [28].

Voltage Constraints: Voltage measurements must be estimated during each optimization run so as to check for voltage violations whenever they occur. The voltages must be maintained within the limits $[V_{\min}, V_{\max}]$ which differ from one country to another as shown in (4.9). Typically in most countries V_{\min} is 0.95 pu. and V_{\max} is 1.05 pu.

$$V_{\min} < V_i^p < V_{\max} \quad (4.9)$$

Active Power Curtailment: The active power curtailment is imposed as a free variable during the optimization run to meet the voltage standards. If R/X ratio of the line are high, the active power and voltage coupling are higher as compared to the coupling between reactive power and voltage which makes active power curtailment more

significant as compared to reactive power support. The active power is limited by the apparent power limit of the inverter as given by (4.10).

$$0 < P_{PV}^{MPPT} - P_{curt} < S_{Invmax} \quad (4.10)$$

where P_{PV}^{MPPT} is the maximum power generation from PV based on irradiance level and S_{Invmax} is the rated apparent capacity of PV inverter.

Reactive Power: The reactive power capability of a smart inverter can be vendor specific or based on the standards. Reactive power is essentially required for voltage regulation but IEEE 1547 prohibits the inverters to actively regulate the voltage based on a feedback controller that changes the reactive output proportionally. The other constraint is to maintain the power factor at each bus within limits. For a system less than 13.8 kV the minimum allowed power factor is 0.95 [48].

If there is an over-voltage issue, reactive power absorption can aid in voltage control whereas in an under-voltage issue, reactive power supply can aid in voltage control within the desired band. Voltage control depends upon the network properties, i.e. the R/X ratio of the line. The reactive power capability is determined by the current active power and the power factor limit at each bus given by (4.11) and (4.12).

$$Q_{Invcap} = \min \begin{cases} \sqrt{S_{Invmax}^2 - (P_{PV}^{MPPT} - P_{curt})^2} \\ S_{Invmax} \tan(\cos^{-1}(pf)) \end{cases} \quad (4.11)$$

$$-Q_{Invcap} < Q_{Inv} < Q_{Invcap} \quad (4.12)$$

where Q_{Invcap} is the reactive power capability of inverter, Q_{Inv} is the reactive power output of inverter and pf is the power factor limit of inverter.

Tap Control: A load tap changing transformer aims at maintaining the voltage either at its output terminals or at a remote bus using a line drop compensator. Based on the IEC6100 standard, the dead-band voltages $[V_{ll}, V_{ul}]$ are preferred to be at least half the tolerance band $[V_{\min}, V_{\max}]$. An intentional time delay, τ_d is included so as to avoid any transient or short time disturbance before the actual tap operation command is given when the voltage drifts beyond the dead band [9]. The time delay tap operation of tap changing regulators are shown in Figure 4.2. T_r is the response time of the motor that operates the tap changes.

The taps of both OLTC and cascaded SVRs tap windings, $Tap_{OLTC} / Tap_{cSVRg}^p$ are considered to have a total of 32 steps (± 16) as shown in (4.13).

$$-Nt / 2 < Tap_{OLTC} / Tap_{cSVRg}^p < Nt / 2 \quad (4.13)$$

where Nt is the total number of controllable tap changes in a regulator, f is the voltage relay output.

In order to minimize the total tap changes on a given day, the tap changes at each intervals must be minimized as much as possible as given by (4.14) and (4.15).

$$|Tap_{OLTC}(h) - Tap_{OLTC}(h-1)| \leq \varphi \quad (4.14)$$

$$|Tap_{SVR,g}^p(h) - Tap_{cSVRg}^p(h-1)| \leq \varphi \quad \forall p, \forall g \quad (4.15)$$

where φ is the limit on number of tap changes for each time interval.

By following this rule, the overall step changes in taps are minimized at the end of the day. The change in voltage at each step is designed to be 0.625%. The taps of both the OLTC and cSVRg is given by (4.16) and (4.17).

$$A_t = ID \begin{bmatrix} 1 + \Delta S_t Tap_{OLTC} \\ 1 + \Delta S_t Tap_{OLTC} \\ 1 + \Delta S_t Tap_{OLTC} \end{bmatrix} \text{ or } ID \begin{bmatrix} 1 + \Delta S_t Tap_{cSVRg}^a \\ 1 + \Delta S_t Tap_{cSVRg}^b \\ 1 + \Delta S_t Tap_{cSVRg}^p \end{bmatrix} \quad (4.16)$$

$$D_t = A_t^{-1} \quad \forall t \quad (4.17)$$

where ID is the identity matrix, t is the set of controllable tap changers $t = -Nt/2, \dots, 0, \dots, Nt/2$, ΔS is the voltage change for change in tap position.

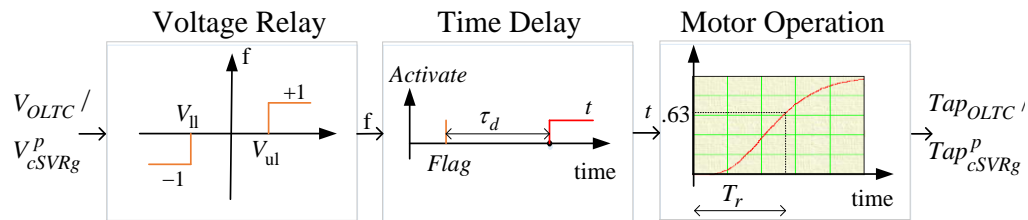


Figure 4.2: The LTC conventional local controller.

Capacitor Bank: Switched capacitor banks have been traditionally used to maintain the reactive power flow at the far ends of the feeder, which in turn aids in maintaining voltage within the ANSI C84.1 standards. A capacitor bank consists of 2-3 units that are controlled discretely. The mathematical models representing the wye connected capacitor bank with N_{Cap} capacitor units are given below.

$$V_C^p = N_C^p I_C^p \quad \forall p \quad (4.18)$$

$$X_C^p = -j(V_{0,C}^p)^2 / Cap_C^p \Delta Q_C^p \quad \forall p \quad (4.19)$$

$$Q_{bank,C}^p = N_C^p \Delta Q_C^p \quad \forall p \quad (4.20)$$

where Cap is the number of capacitor units switched in capacitor banks, X is the reactance of capacitor, V_0 is the nominal voltage, ΔQ is the size of each capacitor unit in capacitor banks and Q_{bank} is the total reactive power support from the capacitor bank.

In order to minimize the switching operation of capacitor units on a given day, the switching operation at each interval must be minimized as much as possible as given by (4.21).

$$\left| N_C^p(h) - N_C^p(h-1) \right| \leq \emptyset \quad \forall p \quad (4.21)$$

where \emptyset is the limit on number of capacitor units switched on/off for each time interval.

4.3.3. Solution Methodology

The objective is to minimize the general function, J_w which is a multi-objective functions for original-MINLP where w is the optimization level index, that is dependent on the change in either tap operation of OLTC, cascaded SVRs, number of capacitors switched on/off or curtailed PV power between two time intervals as given by (4.22).

$$\min \left\{ J_{TOLTC} / J_{TcSVRg} / J_{NCap} / J_{Pcurt} \right\} = \min_{c,d} J_w \quad (4.22)$$

The optimization sub-problems consist of both continuous c , and discrete d variables. The discrete variables are the OLTC and cascaded SVRs tap positions and the number of capacitor banks switched on/off. It is quite difficult to solve the MINLP problem as discussed in the literature.

In this work, we utilize the process of using the two stage method to solve the discrete variables as continuous variables, which make it a NLP problem. After solving the NLP problem that takes far less time as compared to a MINLP, the search space for obtaining the exact solution for discrete variables is reduced to a binary search. A summary of the 2 stage approach is given below.

Step 1. Convert the MINLP problem to a NLP problem by assuming the discrete variables as continuous variables as shown in (4.23). J'_w is the multi-objective functions for relaxed-NLP.

$$\begin{aligned} & \min_c J'_w \\ & \text{Subjected to (4.5)- (4.21)} \end{aligned} \quad (4.23)$$

Step 2. The new discrete variables, d_k^n are utilized to solve the binary MINLP, where d_k^n is the new k^{th} discrete variable. After obtaining the results from solving the NLP problem for the original discrete variables that were solved as continuous variables, they were rounded off to their nearest lower bound. For example, if the SVR tap was found to be either 5.3 or 5.7 the temporary variable t_k^{lb} is 5. Along with d_k^n a binary variable b_k is introduced for each k^{th} discrete variable to solve the binary MINLP. The new variables introduced in solving the binary MINLP follow the rule as given by (4.24).

$$d_k^n = t_k^{lb} + b_k \quad (4.24)$$

Step 3. The binary MINLP problem is solved as shown in (4.25). J'' is the multi-objective functions for binary-MINLP.

$$\begin{aligned} & \min_{c,b} J'' \\ & \text{Subjected to (4.5)- (4.21)} \end{aligned} \quad (4.25)$$

The flowchart summary of converting MINLP to binary-MINLP and solving the optimization is shown in Figure 4.3.

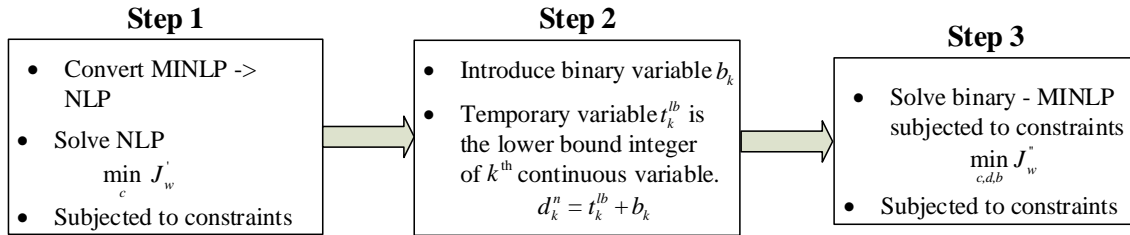


Figure 4.3: Conversion of one optimization form to another.

The load flow analysis is performed at every time step, h for checking any voltage violation case in each zone. The burden of voltage regulation optimization for the entire system is reduced due to zoning of the sections based on the regulating device service territory. The controllers at each stage are set-up to regulate independently while still maintaining the global constraints and updating the memory at each stage. The overall multistage optimization flowchart is shown in Figure 4.4.

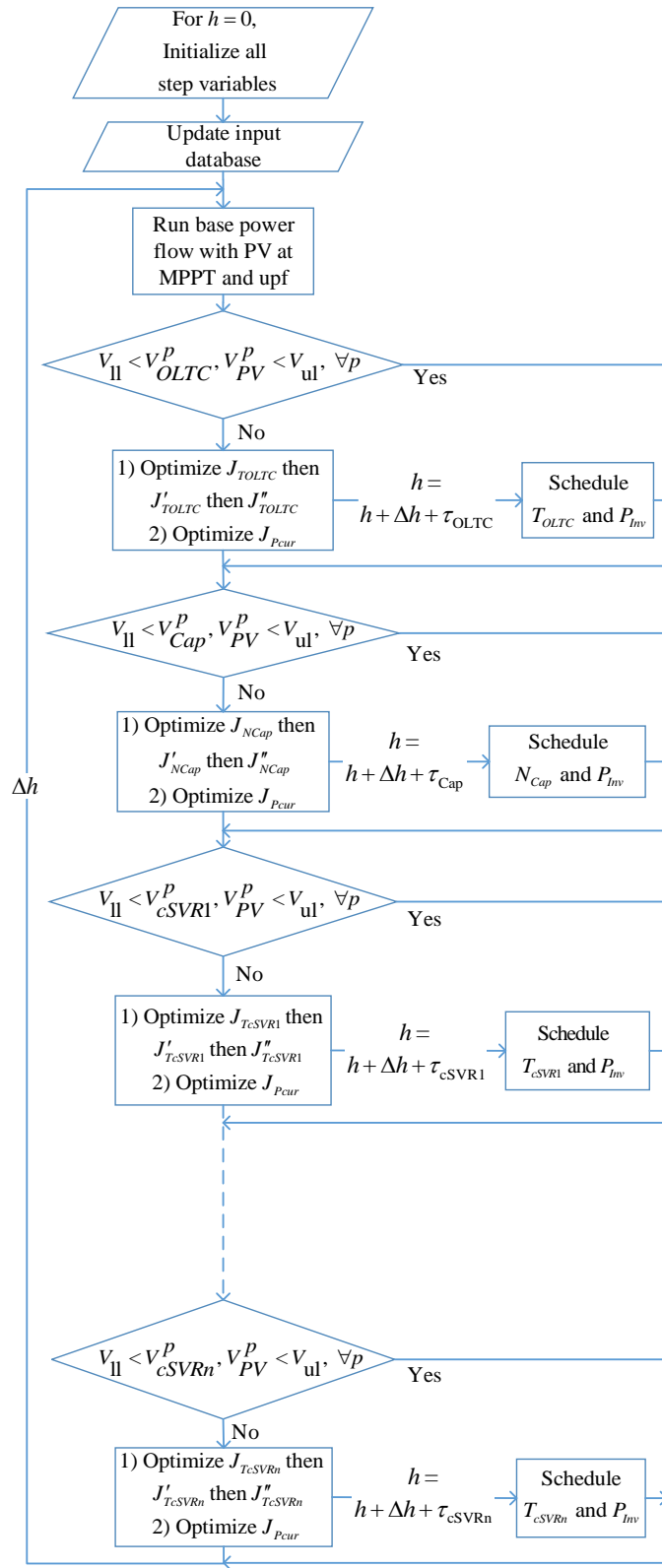


Figure 4.4: Multistage coordination scheme of the proposed voltage regulation.

4.4. Case Studies

The MV unbalanced distribution system utilized in the study has 3 cascaded SVRs along with an OLTC at the substation in line with a high scale PV at the far end of the feeder. There is another SVR (b1SVR) which is placed in a separate branch and does not affect the voltage on the main branch. The SVRs are based on single phase transformers and are time-graded with cSVR1, i.e. nearest to the substation with the least time delay followed by the other regulators that have longer time delays. The MV feeder located in a California utility separated into 4 zones based on SVR target nodes is shown in Figure 4.5.

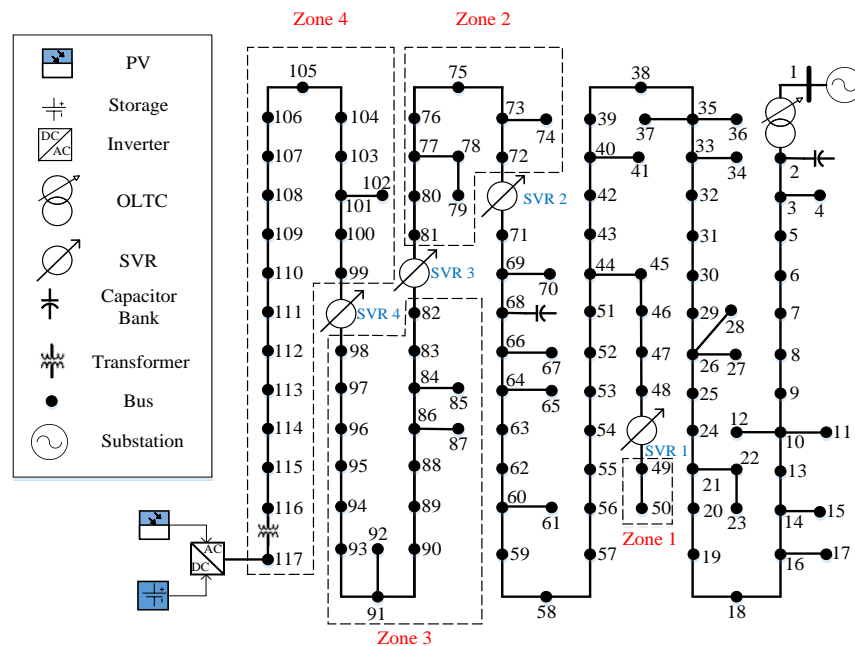


Figure 4.5: MV feeder located in a California utility separated into 4 zones based on SVR target nodes.

Optimization is performed in five conditional stages as discussed previously. Sub-hourly forecasted PV output along with load changes were considered to perform initial load flow analysis to assess the voltage violation conditions. Next, the regulation capability of the extensive regulating devices, as discussed in the previous section, were

utilized to perform centralized optimization. As mentioned previously, the MINLP problem was difficult to solve. Commercially available solvers in GAMS and non-commercial solvers such as BONMIN failed to solve the problem or took hours. But by incorporating the two-stage technique, the time for solving NLP and then binary-MINLP took about 10 min to solve for each stage. All simulation studies have been carried out on a PC with Intel Core i7-4770 @ 3.5-GHz CPU, 8-GB memory, and Windows 7 as the operation system. IPOPT (Interior Point OPTimizer) 3.10.1 was used for solving NLP and BONMIN (Basic Open-source Nonlinear Mixed INteger programming) was used for solving MINLP [49], [50]. MATLAB was used as the modeling language to model the unbalanced system. The large system caused the search space to increase causing the original problem remain unsolved after 1 hour [51]. However, the two-stage approach could solve the formulated MINLP problem in less than 15 min.

Figure 4.6(a) shows the available PV power at the PV plant overlapped with the extracted power as a result of the power curtailment for successful voltage regulation. Active power curtailment was required for 6 days except for day 4 when the PV output was less. Figure 4.6(b) shows the reactive power support required to maintain the voltages within the ANSI standards. Figure 4.6(c) shows the load profiles for the commercial, industrial and residential classes. Typically, all the weekdays follow similar profiles while the weekends follow a different profile, as not many industrial loads are switched on during weekends, while the residential profiles look different as many customers remain home. From the load profiles, it can be seen that the power output was high around noon time during a summer week. Usually at the time when active power output is high, reactive power absorption is required to keep the voltages within limits.

During the morning and evening residential load peaks, reactive power support was required for voltage regulation. On day 4, the PV output was low and hence the reverse power flow was low as well. Reactive power supply from the smart inverter was utilized to keep voltages within the band.

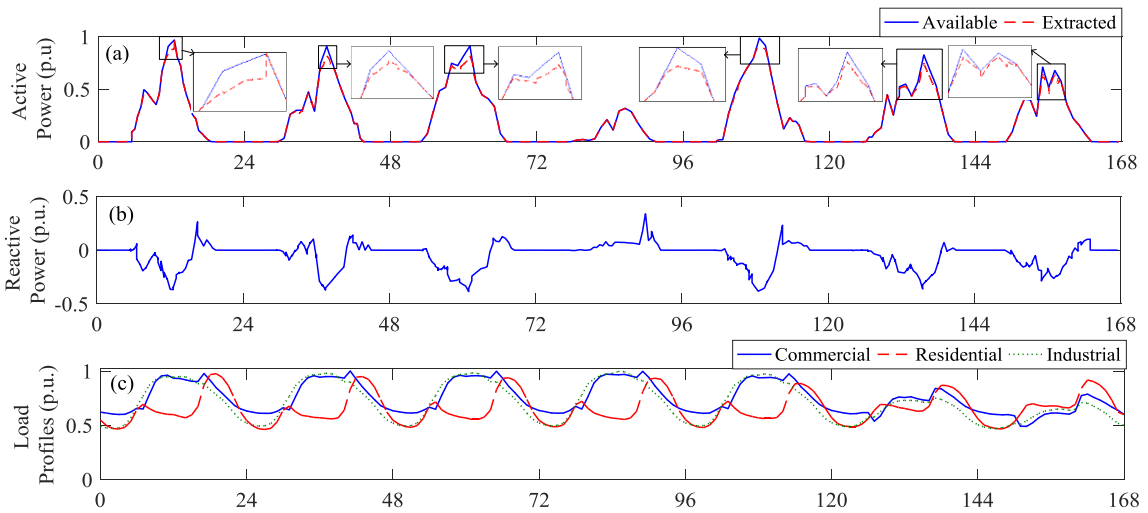


Figure 4.6: (a) Available and extracted PV plant power, (b) Reactive power support by PV plant, (c) Load profiles by class.

Figure 4.7(a-e) shows the tap/switch positions for the different voltage regulating devices on the feeder. All the voltage regulators were utilized except for SVR 4 as the regulators preceding it were used to maintain the voltages within the required band.

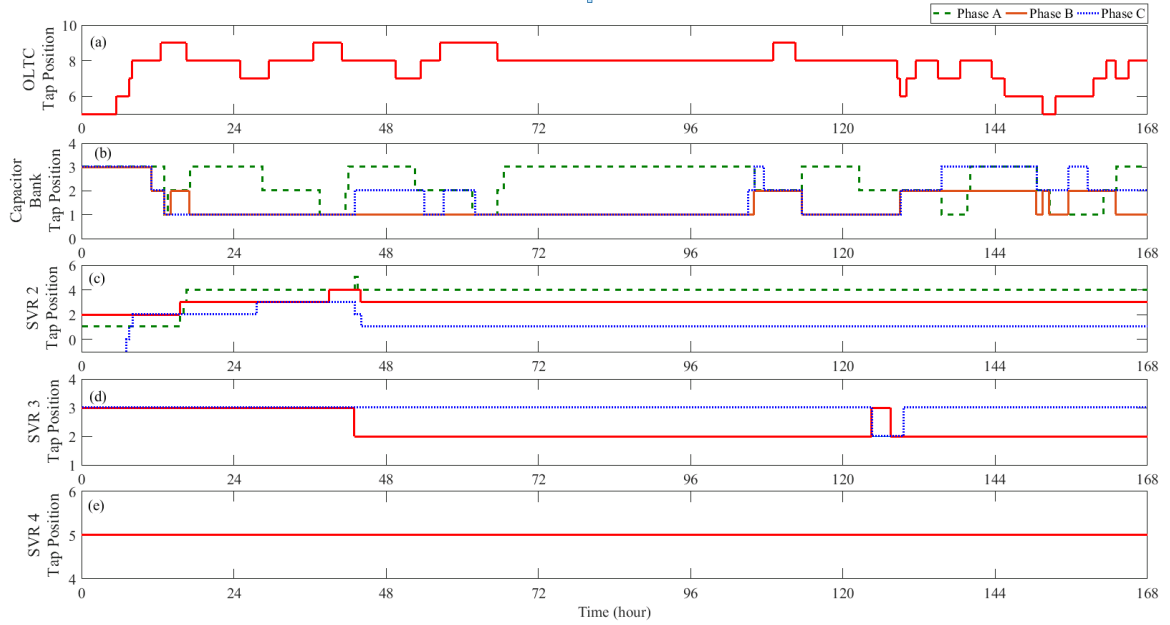


Figure 4.7: (a-e) Convention voltage regulators taps/switch operation.

Figure 4.8 (a-e) show the voltage profiles at the respective voltage regulating device nodes.

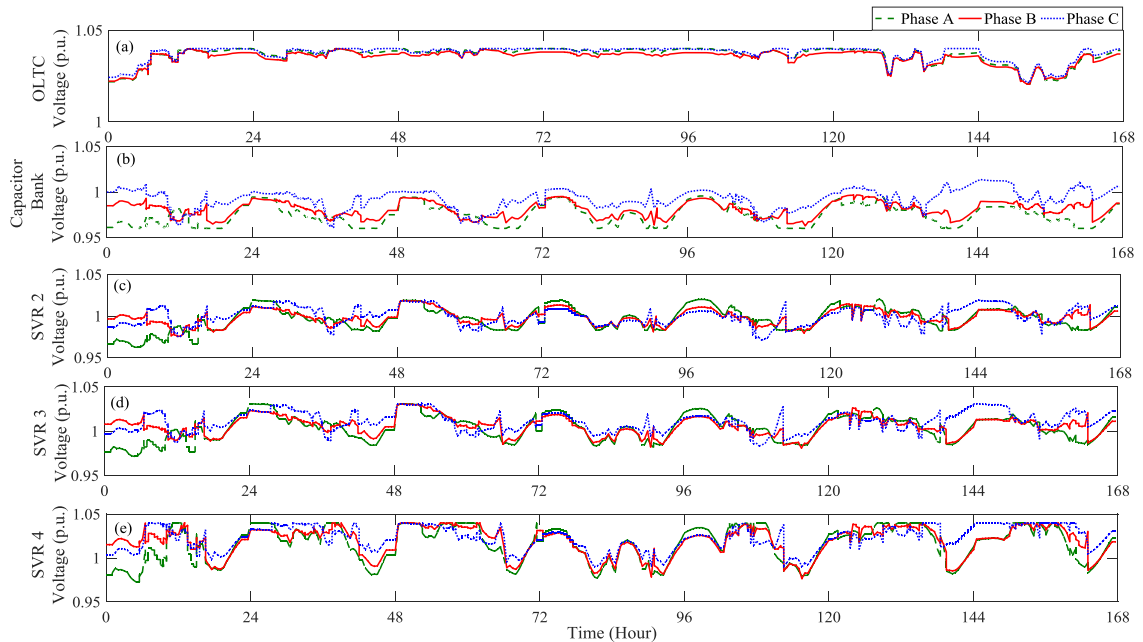


Figure 4.8: (a-e) Regulator target bus voltage profiles.

The voltage magnitude index (VMI) at all the regulator buses is given by (4.26). The

total tap/switch changes (TTSC) for a given day is calculated by (4.27). The percentage energy lost (EL) as a result of active power curtailment is calculated by (4.28).

$$VMI = \sum_{h=1}^{24} |1 - V_{OLTC}| + \sum_{h=1}^{24} \sum_{p=a}^c |1 - V_{Cap}^p| + \sum_{h=1}^{24} \sum_{p=a}^c \sum_{g=1}^{Nt} |1 - V_{cSVRg}^p| \quad (4.26)$$

$$\begin{aligned} TTSC = & \sum_{h=1}^{24} |Tap_{OLTC}(h) - Tap_{OLTC}(h-1)| \\ & + \sum_{h=1}^{24} \sum_{p=a}^c \sum_{g=1}^{Nt} |Tap_{cSVRg}^p(h) - Tap_{cSVRg}^p(h-1)| \\ & + \sum_{h=1}^{24} \sum_{p=a}^c |N_{Cap}^p(h) - N_{Cap}^p(h-1)| \end{aligned} \quad (4.27)$$

$$EL = \left(\int_{h=1}^{24} P_{PV}^{mpppt} dh - \int_{h=1}^{24} P_{Inv} dh \right) \times 100 / \int_{h=1}^{24} P_{PV}^{mpppt} dh \quad (4.28)$$

The subsystem specifications for the PV plant is given in Table 4.1. The daily performance parameter comparison summary is given in Table 4.2.

Table 4.1: Subsystem specifications for the PV plant

Subsystem	Specifications
Inverter	2 MVA, Power factor limit = 0.93
Transformer	2.2 MVA, 0.48/12 KV, Y-Δ, 0.001 + j 0.0564 (pu)

Table 4.2: Daily performance parameter comparison

	Day 1	Day 2	Day 3	Day 4	Day 5	Day 6	Day 7
VMI	69.03	74.8	78.1	64.8	70.9	71.07	68.7
TTSC	23	18	11	0	10	18	19
EL (%)	1.74	3.11	3.37	0	1.56	4.43	2.76

4.5. Summary

In this paper, we discuss an optimal operation of cascaded regulators and smart inverter tied to a PV plant in order to maintain voltages within a band and minimize the over usage of regulating devices. Large scale PV on a distribution feeder can have

negative impacts on over-usage of regulating devices and can cause overvoltage issues on the feeder. A coordination strategy between the regulating devices in the feeder was introduced. This method adopts a zonal level-based centralized management of regulating devices utilizing Volt/VAR control methods. The complexity and handling of data is reduced by adopting a novel and fast multi-stage optimal coordination strategy between the regulating devices in an unbalanced distribution system. A week-long study was performed to assess the performance parameters to gather the effectiveness of the control algorithm during varying conditions of the day. By adopting the zonal voltage coordination strategy, the over-usage of regulating devices further down the feeder was reduced as the preceding regulators further up the feeder took care of voltage regulation. Active and reactive power control capabilities of the smart inverters were used effectively to aid in the voltage regulation.

CHAPTER 5 : HYBRID SYSTEM OPERATION IN MICROGRID

5.1. Introduction

The objective of this work is to demonstrate the advantages of a Battery Energy Storage System (BESS) in a simulated microgrid testbed that is characterized by photovoltaic (PV) power as the primary generation source. A PV source interfaced with BESS at the DC link has the advantage that it can emulate a conventional generator with the added attribute of providing reserve power. A microgrid test bed is designed with multiple PV/BESS systems dispersed at various locations. The presence of BESS enables the PV sources with the ability to participate in frequency and voltage regulation during grid-connected mode of operation. A droop control based power sharing scheme is employed for the purpose of regulation. A strategy for charging is also employed in the case where the power demanded is less than the PV array power.

Photovoltaic (PV) sources are becoming increasingly popular as a community owned source of energy, which is based on a local controller [52]. A community could be a university, a township, a remotely located village, a group of buildings in a downtown area etc. There have been quite a few publications on the topic of PV as a major source of power in a community. PV being intermittent in nature creates various grid integration issues that need to be resolved. A few solutions have been suggested in this case, for example, to include a battery energy storage system (BESS) as well as to dump loads in case of excess generation or to mitigate the power output from a PV array by lowering

the maximum power point [53]. There have also been quite a few publications on different configurations of BESS addition at the microgrid level in the presence of PV as the major source of energy. In [54], an inverter interfaced with the PV array behaves as a current source by injecting power to the grid when in grid-connected mode while the BESS is utilized for automatic regulation purposes by reconfiguring the inverter as a voltage source based on a droop scheme in the islanded mode. In [55], a fuel cell is interfaced with the DC link in between the PV to grid system to smoothen the power variability caused by the intermittent nature of the PV. A BESS is connected elsewhere for both grid-connected and islanded purposes to meet the peak demand and power shortages respectively. In [56], a modular based PV system along with BESS was developed to operate in different modes such as grid-connected charging, islanded discharging etc. based on the DC bus voltage level. In [57], a unified control strategy was introduced where the BESS and PV inverters operated with both active feedback compensation and droop control. In grid-connected mode, the Distributed Energy Resources (DERs) operated with set-point controls for power generation but in islanded mode, they could automatically transform its control based on droop settings. As the number of DGs like PV, wind, fuel cells etc. in a grid increase, there is a reduction in the overall grid inertia which results in improper regulation due to sudden power imbalance in the system [58]. Thus, DGs such as PV systems at the community level which are in the range of 1-10 MW would have to contribute to microgrid frequency and voltage regulation by automatically participating in the load following function based on droop control. Better voltage and frequency regulation can be achieved using enhanced power electronic control that would eventually benefit both the microgrid and the PV-owner. On

the one hand, a well-designed power electronic converter can be used for voltage and frequency conditioning, thus benefiting the grid; while on the other hand, the PV system could be made to coordinate dynamically with grid operational circumstances [59]. The benefits of inverter based DG have been discussed in terms of regulation, reactive power compensation and power factor correction in [60]. The objective of this work is to suggest a control strategy for cases during a typical day when the PV system would normally act simply as a negative load, but when included with a BESS could perform as a conventional generator. Similar to conventional generators, the PV/BESS system operation is based on droop settings in grid-connected mode that enhance the capability of such systems to instantaneously participate in power regulation at the local/microgrid level. When the demanded power dictated by the droop controller is higher than the power being produced by the PV system, the battery injects the excess power automatically. Similarly when the demanded power dictated by the droop controller is lower than the power being produced by the PV system, the battery absorbs the excess power automatically. By setting the PV systems to droop control in parallel with the conventional grid governor-based droop response, they perform in a manner similar to conventional generators in performing the tasks of frequency and voltage regulation.

5.2. Droop Controller Concept

The simulated microgrid testbed in this work is dominated by PV plants interfaced with energy storage units and embedded at different buses. As each unit consists of an energy storage unit, the PV system can behave as a dispatchable source with an enhanced capability to provide ancillary services such as frequency and voltage regulation. The sources within the microgrid take care of frequency and voltage variations automatically

based on droop controller settings in proportion to active and reactive power deviations respectively. The inverter may behave as a current source or a voltage source when operating as a grid interactive power converter. The rest of this section deals with the concept behind droop control. We consider the circuit in Figure 5.1, to study the power flow between a source and an AC bus through a transmission line or a transformer which can be represented in the form of impedance [61].

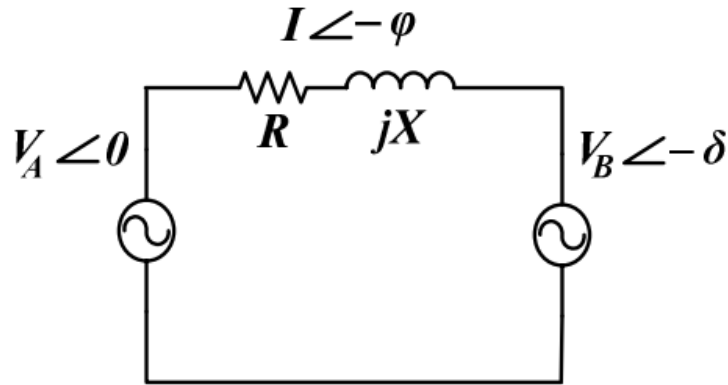


Figure 5.1: Power flow study circuit.

As can be seen from Figure 5.1, there are two independent sources that have different voltage magnitudes and are separated by an angle δ . V_A is the magnitude of voltage at the AC terminals of an electronically interfaced source such as a PV/BESS system. V_B is the magnitude of voltage at the point of common coupling (PCC) where the infinite grid is connected. The power flow equations between the two buses are given by:

$$\begin{aligned} P_A &= \frac{V_A}{R^2 + X^2} [R(V_A - V_B \cos \delta) + XV_B \sin \delta] \\ Q_A &= \frac{V_A}{R^2 + X^2} [X(V_A - V_B \cos \delta) - RV_B \sin \delta] \end{aligned} \quad (5.1)$$

where P_A and P_B are the active and reactive power flows respectively. $Z = R + jX$ is the line impedance between the two sources.

In the case of a distribution system, assuming that the network impedance is dominated by the inductive component (reactance), then $X/R > 1$, hence the power equations can be reduced further and written in the form:

$$\begin{aligned} P_A &\approx \frac{V_A}{X}(V_B \sin \delta) \Rightarrow \delta \approx \frac{XP_A}{V_A V_B} \\ Q_A &\approx \frac{V_A}{X}(V_A - V_B \cos \delta) \Rightarrow V_A - V_B \approx \frac{XQ_A}{V_A} \end{aligned} \quad (5.2)$$

From the above equations it can be inferred that the active power flow is dependent mainly on the phase angle between the two sources which in turn is proportional to the frequency changes while the reactive power is dominated by the voltage difference. The equations can be rewritten in the droop form as:

$$\begin{aligned} f - f_0 &= -k_p(P - P_0) \\ v - v_0 &= -k_q(Q - Q_0) \end{aligned} \quad (5.3)$$

where $f - f_0$ and $v - v_0$ represents the grid frequency and voltage deviations from the initial values respectively. $P - P_0$ and $Q - Q_0$ are the variations in active and reactive power to be delivered by the inverter to compensate for the frequency and voltage deviations. k_p and k_q represents the active and reactive power droop gains.

Figure 5.2 shows the droop controller curves that would be implemented on the outer loop for sensing any active or reactive power changes due to load variations, generator loss etc. Based on these changes, the frequency or voltage settings are changed for the PV/BESS system to act as a dispatchable source.

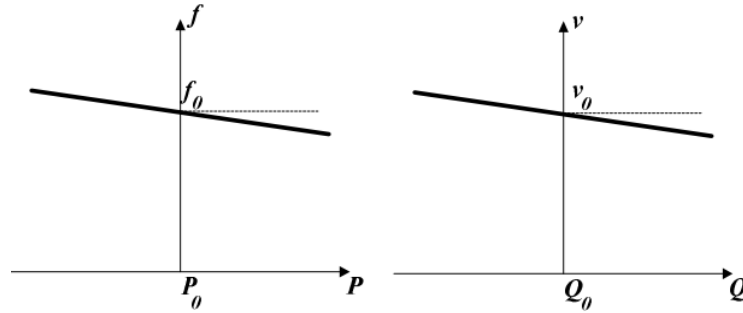


Figure 5.2: Voltage and frequency droops based on inductive network mode.

In [48], the benefit of integrating a BESS in parallel with a grid tied PV for providing frequency regulation by droop control response was discussed.

DGs connected to the grid acts as a current source when in grid connected mode while in extreme situations when the microgrid is in islanded state it could act as a voltage source in parallel with other DGs to regulate the voltage and frequency in the grid. The advantage of utilizing a droop based controller for each DER system is that the frequency and voltage can be regulated automatically without a communication based centralized controller. Though the DG/battery system can be automatically controlled there needs to be a centralized optimization controller to manage generation to supply priority based load in the secondary control loop during the islanded period. The secondary control level is where the microgrid energy management system is implemented to meet the reliable, secure and economical operation. Secondary control is the highest level of control during the islanded period essentially utilizing a centralized optimization function to determine the set points for the DERs based on a global objective and operates on a much slower time frame as compared to the primary controller. The slower time frame gives the secondary controller enough time to perform complex calculations as compared to the primary controller action which needs to be implemented on a much faster time frame. The optimization objective helps in determining the droop settings and battery

requirement for each DG/battery system to sustain the maximum number of loads with the higher priorities given to critical loads. This is critical to meet the supply-demand balance in a slower time frame. The outputs from the secondary controller are given to the primary controller as reference values to work towards second-second power balance. The centralized controller is a model based optimization problem which aids in accurate prediction of the reference values given to the primary controller. Based on predicted/forecasted generation and load data

The centralized controller has the ability to shed loads with lower priority when needed to maintain adequate power quality which includes both frequency and voltage regulation in order to sustain the maximum number of loads. As frequency and voltage regulation require both active and reactive power support from the inverter based system a complex calculation is made to allocate. The secondary controller must also ensure that the high deviations caused due to the droop control action are taken care by utilizing a PI controller to minimize the deviations to zero after a heavy unbalance between generation and load.

5.3. Controller Design

Within the PV/BESS system, there are three different kinds of controllers which will be discussed in detail in this section.

5.3.1. PV Array Control

The PV array is connected to the DC link, C_{DC} through a boost converter to step up the voltage at the PV array terminals to a higher value. An MPPT control action is implemented so as to maximize the power output from the PV array, P_{PV}^{MPPT} for a given

irradiance value. The boost converter is operated with a duty ratio such that voltage at the PV terminals is maintained at the MPPT voltage.

5.3.2. Inverter Side Control

The inverter side control action is described in Figure 5.3. In this work the inverter behaves as a voltage source when operating in a grid-interactive configuration [61]. Switches S1, S2 and S3 are embedded at different locations at the inverter side control to change selections based on different operations. In the case, when the demanded/measured power, P_{meas} is higher than the PV array power, P_{PV}^{MPPT} and the battery is able to provide the difference of the two powers, the switches trip to selection 1, if not they trip to selection 2. P_0 and Q_0 are the initial set-points for the reference active and reactive powers that are approximately equal to the expected power from the PV/BESS system based on the local loads. For selection 1, the droop controller sets the reference frequency, ω_{ref} based on active power droop and hence the reference rotation angle, θ for abc-dq/dq-abc frame conversion. The droop controller also sets the direct axis reference voltage $v_{d,ref}$ based on reactive power droop while the quadrature axis reference voltage $v_{q,ref}$ is maintained at zero. The error between the reference direct axis voltage, $v_{d,ref}$ and measured direct-axis voltage, v_d is amplified by a PI regulator to set the direct-axis reference current, i_d^* . Similarly, the error between the reference quadrature-axis voltage, $v_{q,ref}$ and measured quadrature-axis voltage, v_q is amplified by a PI regulator to set the quadrature-axis reference current, i_q^* . [61].

In the case when the demanded/measured power, P_{meas} is lower than the PV array power, P_{PV}^{MPPT} , the excess power from PV array would be absorbed by the battery to maintain the power balance. In that case the PV/BESS system inverter behaves in a grid feeding configuration while at least one source inverter has to behave in a grid forming/grid supporting configuration. For selection 2, the rotation angle, θ for abc-dq/dq-abc frame conversion is determined from a phase locked loop (PLL). Also, when tripped to selection 2, the DC link voltage, V_{DC} is maintained constant by comparing it with a reference DC link voltage, V_{DC}^{ref} . The error between the two values is sent to a PI regulator whose output determines the direct-axis reference current, i_q^* . In order to maintain a desired reactive power output, the reference reactive power, Q_{ref} is divided by the measured direct-axis voltage, v_d to obtain the quadrature-axis reference current, i_q^* [61].

The other important criterion for limiting the BESS charging and discharging amounts is the range of the state of charge (SoC). In case the BESS reaches its lower point of SoC i.e. 0.2, it must stop discharging and no power can be pumped out of the battery. Similarly, if the BESS reaches its higher point of SoC i.e. 0.8 it must not be charged further and other options such as using dump loads or reducing the MPPT point to a lower value could be explored. The power balance equation across the DC link is given by (5.4) [57].

$$\left(\frac{C_{DC}}{2\omega_b} \right) \frac{dV_{DC}^2}{dt} \approx P_{Hyb} - P_{Inv} \approx \left(P_{PV}^{MPPT} \pm P_{Bat} \right) - P_{Inv} \quad (5.4)$$

where C_{DC} is the capacitance of the DC link, ω_b is the base frequency, P_{Hyb} is the power output from the PV/battery system, P_{Bat} is the power output from the battery and P_{Inv} is the PV/Battery system active power output at the terminals of the inverter. (5.4) provides the notion behind power tracking based on V_{DC} .

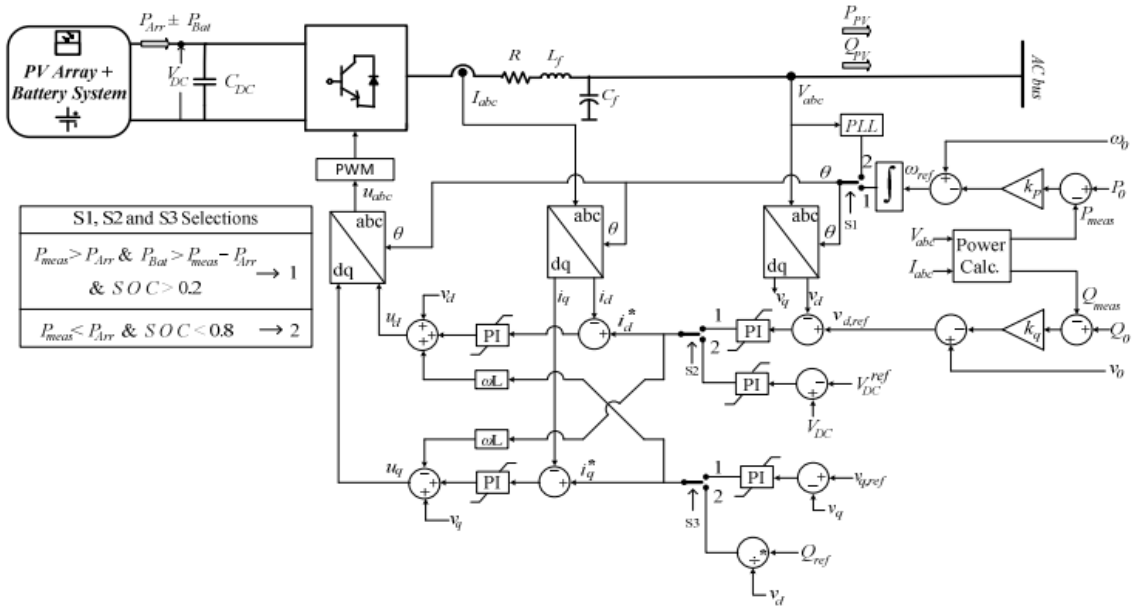


Figure 5.3: Inverter side control system.

5.3.3. Battery Side Control

The battery side control action is described in Figure 5.4. A sizable battery is interfaced at the DC link of every PV source that is connected in the microgrid. In order to take care of the charging and discharging process of the battery, a synchronous buck converter is connected in between the battery and the DC link [62]. Switches S4 and S5 of the battery side control system operate simultaneously with the inverter switches to control the discharging and charging process of the battery. When the demanded/measured power, P_{meas} is higher than the PV array power, P_{PV}^{MPPT} and the battery is able to provide the difference of the two powers, the battery switches trip to

selection 1, if not they trip to selection 2. For the discharging case, the DC link voltage is compared with a reference DC link voltage, V_{DC}^{ref} . The error between the two is amplified by a PI regulator which determines the reference discharging current, I_{dbat}^* . The regulation of discharging current, I_{dbat} to its reference value determines the duty ratio, d1 to produce the square wave, SW1 utilizing pulse width modulator, PWM 1.

In case of charging, the reference charging current, I_{cbat}^* can be computed as shown in (5.5).

$$I_{cbat}^* = \frac{P_{PV}^{MPPT} - P_{meas}}{V_{Bat}} \quad (5.5)$$

where V_{Bat} is the voltage across the battery terminals capacitor.

The regulation of charging current, I_{cbat} to its reference value determines the duty ratio, d2 to produce the square wave, SW2 utilizing pulse width modulator, PWM 2.

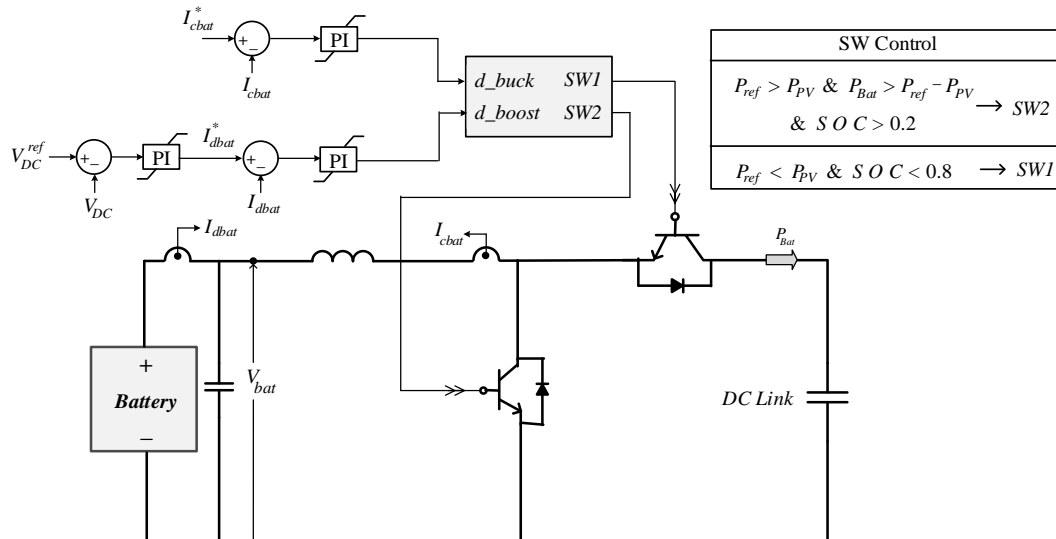


Figure 5.4: Battery side control system.

5.4. Microgrid Implementation

The microgrid architecture is shown in Figure 5.5. It can be seen that the microgrid is in grid-connected mode with three PV/BESS systems at buses 3, 5 and 12. The grid/substation is also in droop mode along with other PV/BESS systems. There is a capacitor bank near the PCC to take care of a part of the total microgrid reactive load. The PV/BESS systems take part in reactive support through voltage based droop control whenever there is a change in local loads. The architecture of the microgrid and the load details were taken from [57].

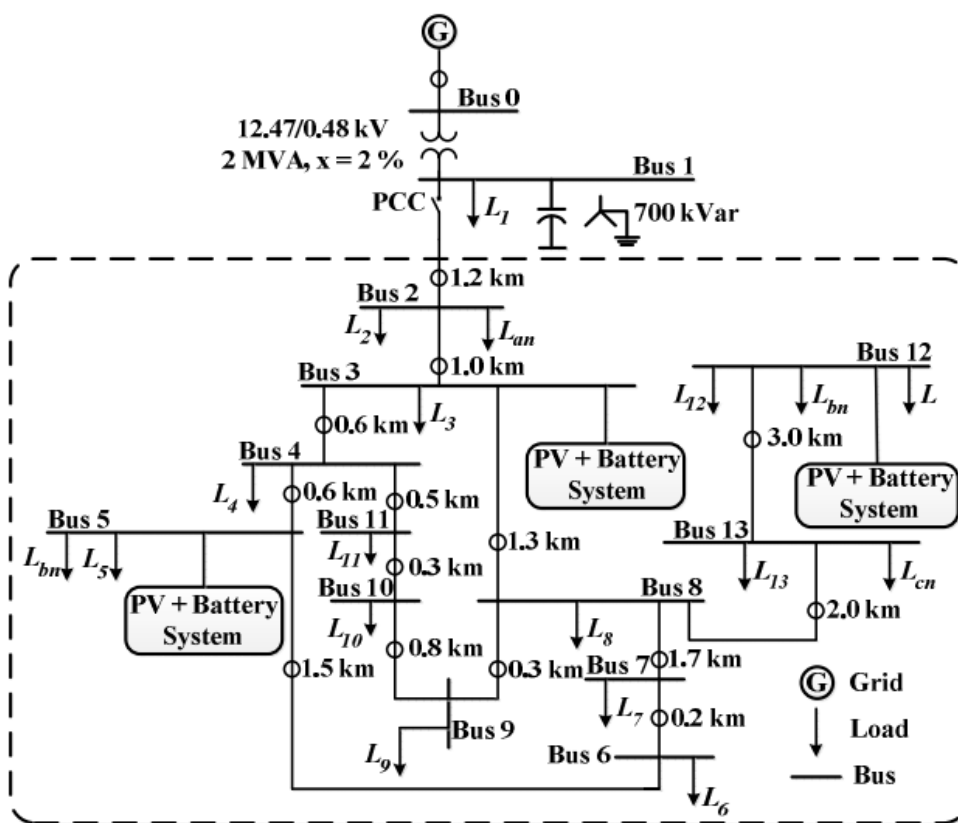


Figure 5.5: Microgrid architecture.

5.5. Results

In order to test the two conditions of BESS activity i.e. charging and discharging, two different case studies were performed. The simulations for both cases were carried out in PSCAD/EMTDC software environment.

5.5.1. BESS Discharging Case

For this case, the reference power based on droop adjustments is higher than the power produced by the PV system, hence the BESS needs to supply the excess power through automatic discharge. The irradiance within the study time was varied between 800 W/m^2 and 1000 W/m^2 for every PV array, which is the typical range of irradiance when the sun is shining. The loads were increased at time, $t = 2, 3, 5$ sec. The battery was assumed to be fully charged initially. The active power outputs from the grid and the three PV/BESS systems are shown in Figure 5.6. It can be seen that when the load is varied at different instants, the sources are able to step up their power output based on the droop settings.

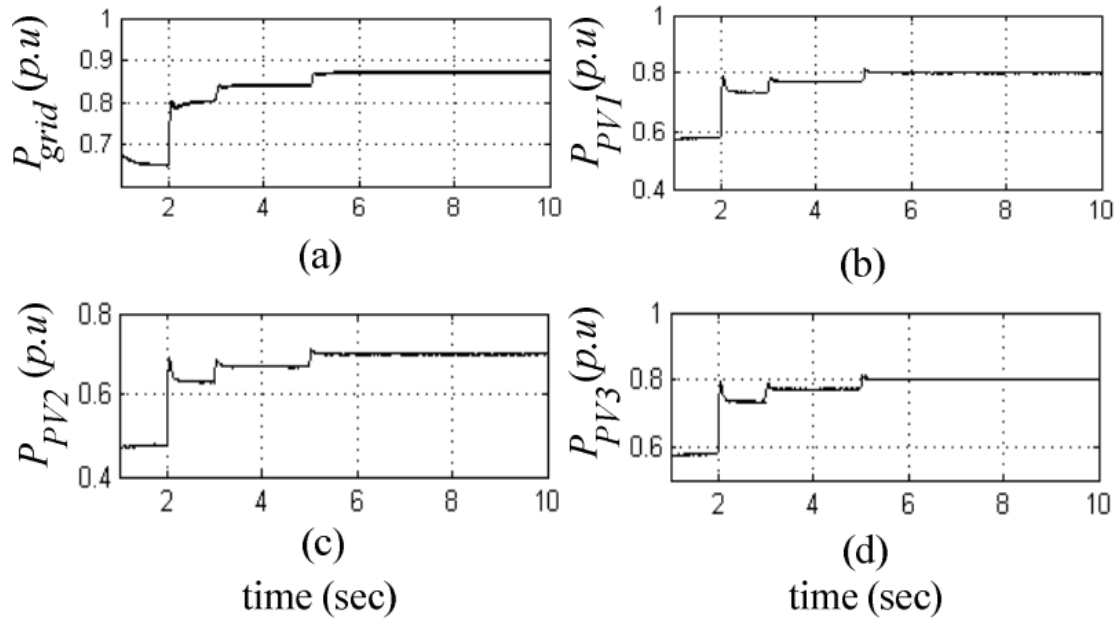


Figure 5.6: Active power outputs of 4 inverters.

The reactive power outputs from the grid and the three PV/BESS systems are shown in Figure 5.7. Similar to the active power, the reactive power outputs from the sources increase proportionately as the load increases based on the droop control setting. The reactive parts of the loads increase at the same time $t = 2, 3, 5$ sec as the active parts of the loads increase.

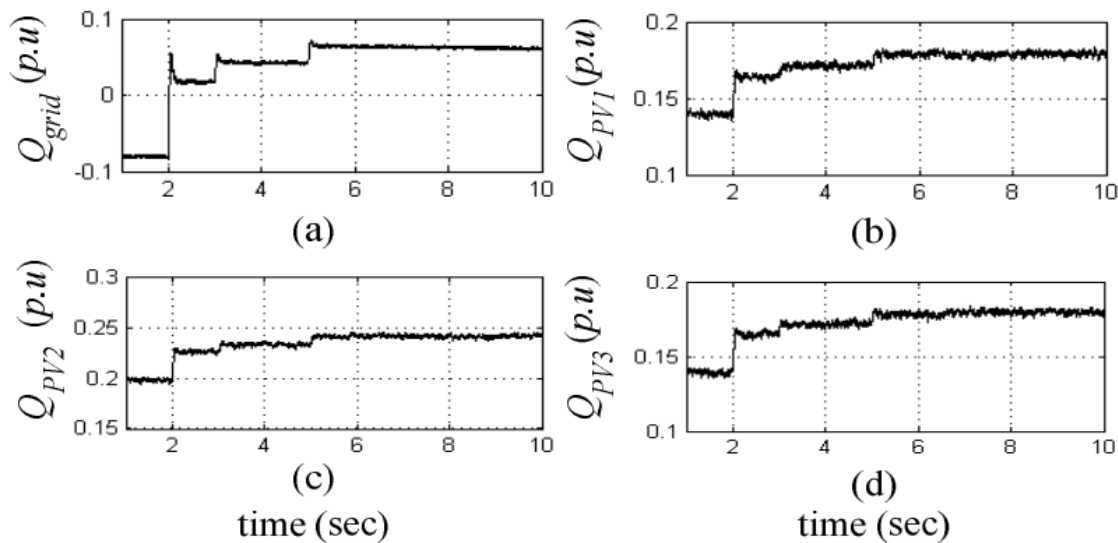


Figure 5.7: Reactive Power Outputs of 4 inverters.

The internal phenomenon within the PV/BESS system is presented in Figure 5.8. The variation in the output from the PV array due to a change in the irradiance value is shown in Figure 5.8(a). The irradiance within the study time was varied between 800 W/m^2 and 1000 W/m^2 , which is the typical range of irradiance when the sun is shining. The variation in output from the battery due to two conditions is shown in Figure 5.8(b). One of the conditions is when the power output from the PV array changes but the load may or may not remain constant. Another condition is when the PV output remains constant, but the load varies up or down. At time $t = 2, 3$ and 5 sec, the variations are due to changes in the PV array output and load changes. At time $t = 7$ sec the variation is only due to PV output change while the load remain unchanged. The variation in the DC link voltage as the power output from the PV/BESS system changes is shown in Figure 5.8(c).

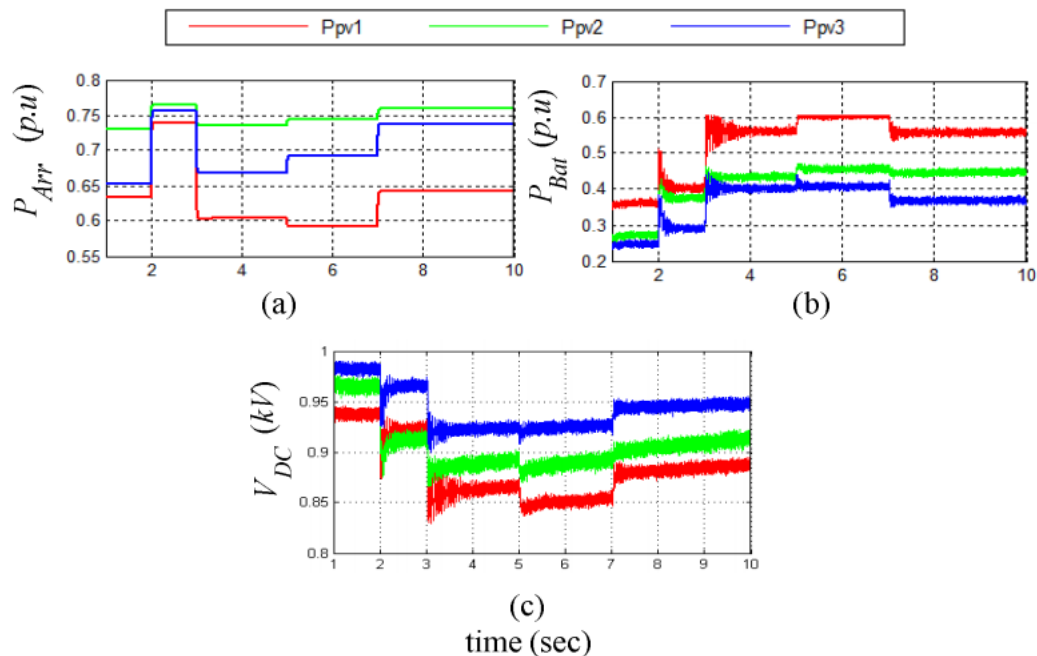


Figure 5.8: (a) PV systems internal measurements during battery discharging (b) BESS charging condition and (c) DC bus voltages.

For this case, the reference power based on droop adjustments is lower than the power produced by the PV system; hence the BESS needs to absorb (via charging) the excess

power automatically in order to maintain a power balance in the system. In this case, the charging of the BESS is studied for one of the PV/BESS systems connected to the grid. The grid acts as the source for voltage and frequency settings within the test system. The active power output from the PV/BESS system is shown in Figure 5.9(a). It can be seen that the PV/BESS system follows different reference settings in the time frame. The reference power settings change at time $t = 6, 10$ and 18 sec. The reactive power output from the PV/BESS system which is maintained at a constant reactive power reference value, $Q_{ref} = 0$ pu in this case is shown in Figure 5.9(b). Similar to the first case, the irradiance within the study time was varied between 800 W/m^2 and 1000 W/m^2 at time $t = 2.5, 9.5, 17$ and 23 sec for the PV array which can be seen in Figure 5.9(c). The power being absorbed by the BESS is shown in Figure 5.9(d). The negative sign indicates a change in the direction of the power flow signifying that a battery charging takes place. The variations in the battery absorptions are due to both reference power changes and PV output variations. The DC link voltage is maintained at 1000 V which can be seen in Figure 5.9(e). At time $t = 10$ sec the spike in DC voltage is due to the sudden increase of active power reference value from, $P_{ref} = 0.2$ to 0.5 pu. Within a few milliseconds, the voltage is brought back to its reference value.

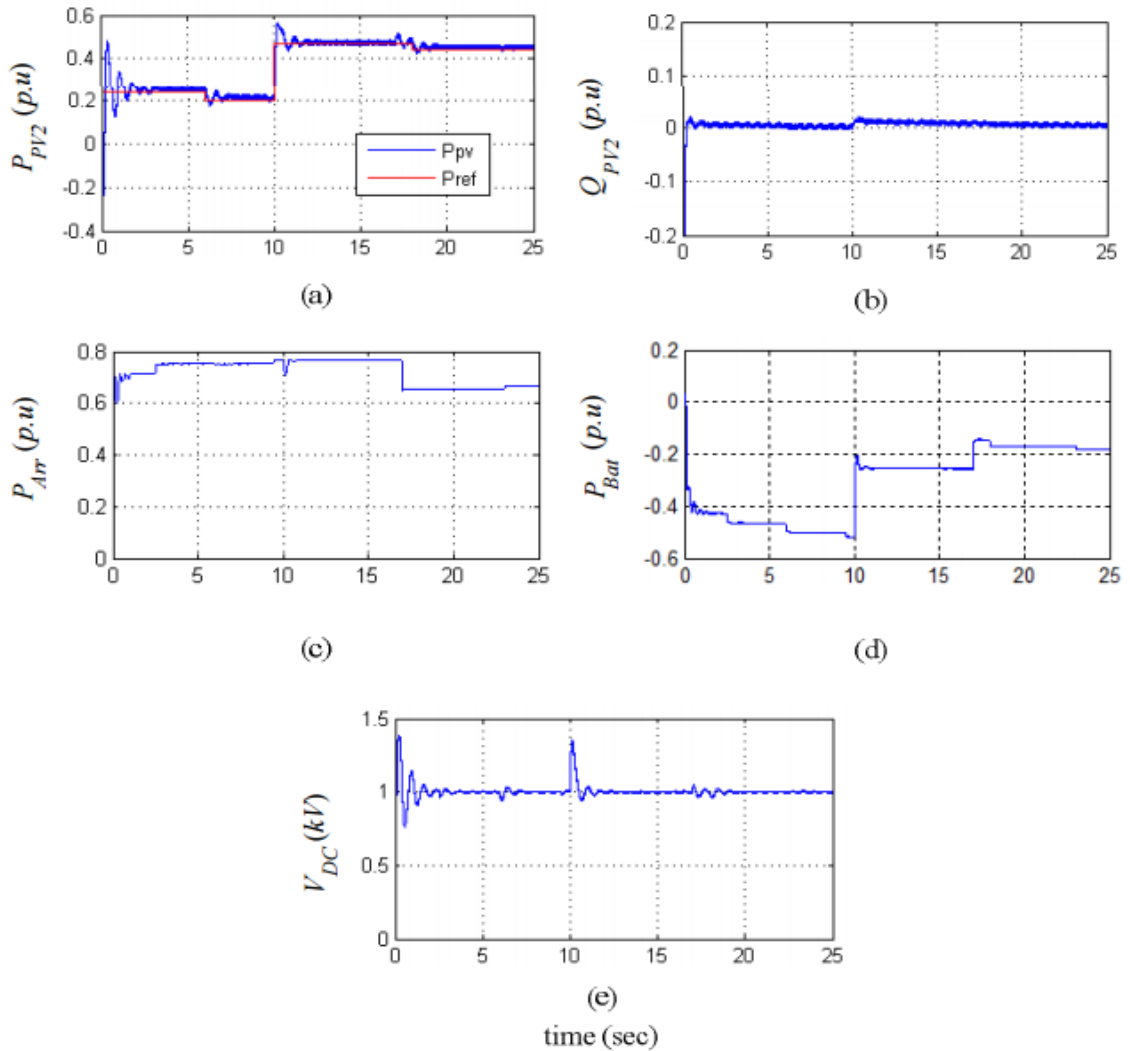


Figure 5.9: PV/BESS system measurement during battery charging condition.

5.6. Summary

In this work a control strategy for various PV based systems is proposed to actively participate in the frequency and voltage regulation within a microgrid in grid-connected mode. Each PV based systems is interfaced with a BESS at the DC link to aid for the deficiency or excess power production from each PV array source. The capability of such PV/BESS systems to smoothen the power output was demonstrated by simulations in PSCAD/EMTDC software environment for the battery discharging and charging cases. In the case when the power demanded was more than the power produced by the PV array,

the amount needed was produced by the battery. In the other case, when the power demanded was less than the power produced by the PV system, the excess power from the PV array was directed to the battery to recharge it. Automatic active and reactive power regulations were possible based on P-f and Q-V based droops when the demanded power was more than the PV array source generation. In the other case when the power demanded was less than the power produced by the PV array source, the power produced by the system were based on active and reactive power set-points.

CHAPTER 6 : MULTI-STAGE OPERATION OF DISTRIBUTED ENERGY RESOURCES IN A STANDALONE MICROGRID CONSIDERING COST AND FREQUENCY DEVIATION MINIMIZATION

6.1. Introduction

A multi-stage power regulation scheme for different distributed energy resources (DERs) in a standalone microgrid is proposed based on the time of day. For islanded mode, a two stage operation based on cost optimization and frequency regulation is suggested during the on-peak period. The microgrid energy management system (M-EMS) aims to perform an economic generation scheduling based on an overall cost minimization strategy with the help of several droop enabled sources that includes two hybrid renewable distributed generator (RDG)/battery systems and three fuel based dispatchable distributed generators (DDGs). In case a battery reaches its lower state of charge (SoC) limit, the hybrid system inverter operates as a current source by disconnecting the battery. In addition during the off-peak period, a multi-stage objective optimization strategy is suggested which includes the charging of batteries to their nominal target values while operating as a current source. Numerical results from the 33 bus distribution system that is operated as a microgrid, are used to show the effectiveness of the developed strategy. For a sustainable future with reduced dependence on conventional energy resources, renewable energy integration into the grid is necessary especially in the form of distributed generation on the distribution systems side of the grid along with other smart grid technologies. Microgrids aid in better handling and

management of DGs, battery energy sources and controllable loads in the distribution systems. Microgrid operation has become a topic of discussion in many recent works. The key feature of a microgrid is the ability to isolate itself from the main grid and behave as an island during faults, natural calamities, and lack of generation to serve important loads, etc. or indefinitely work in standalone mode by using the generation capability of the Distributed Energy Resources (DERs). It is predicted that many feeders in the distribution systems could be converted into small pockets of microgrids for more reliable operation and serve critical loads in the time of need. During the period of islanding, the management of generation becomes important to serve the loads while maintaining adequate power quality. Important businesses are given higher priority than residential loads in that case. One of the main challenges in an isolated microgrid is the scheduling of DGs to meet the demand when both have intermittent behavior. Batteries have proved to have multi-functional capabilities when it is integrated in parallel with an intermittent source in both grid-connected and islanded modes. With expected lower of battery costs it could be expected that high scale renewable DGs would be equipped with storage devices to make them more dispatchable for both control and optimal power flow. When a PV/Wind is connected in parallel with a battery they can emulate the characteristics of a conventional generator which is essential to maintain the power quality in an isolated microgrid.

The response of DERs in a microgrid can be classified into three time graded control strategies for power regulation in a microgrid. The primary response aims toward meeting the imbalance between the generated power and load for the first few seconds. In centralized generator based systems, the pre-primary response is taken care by the inertia

of the rotating mass in a synchronous generator. Many works in the past have dealt with the emulation of synthetic inertia for DGs that are not synchronized naturally with the grid frequency. As wind generators have a rotating mass it is easier to emulate inertia but for PV system with no rotating mass, fast control action need to be embedded in order to meet the instantaneous imbalance in few milliseconds. Frequency regulation becomes more important in microgrids due to their relatively low level of inertia and incremental share of renewable power generation as compared to the main grid. For primary response there is no need for communications and the inverter based DGs are able to respond to power imbalance based on measured local voltage and frequency. The adjustable droop settings of the DGs present in the microgrid help in providing power to the loads with higher priority.

6.2. Control Hierarchy for the Microgrid Test System

DGs connected to the grid acts as a current source when in grid connected mode while in extreme situations when the microgrid is in islanded state it could act as a voltage source in parallel with other DGs to regulate the voltage and frequency in the grid. The advantage of utilizing a droop based controller for each DER system is that the frequency and voltage can be regulated automatically without a communication based centralized controller. Though the DER systems can be automatically controlled there could to be a centralized optimization controller adopted, to manage generation to perform certain objectives in the secondary control loop during the grid-connected/islanded period. The secondary control level is where the microgrid energy management system is implemented to meet the reliable, secure and economic operation. Secondary control is the highest level of control during the islanded period in a particular microgrid,

essentially utilizing a centralized optimization function to determine the set points for the DERs based on a global objective and operates on a much slower time frame as compared to the primary controller. The slower time frame gives the secondary controller enough time to perform complex calculations as compared to the primary controller action which needs to be implemented on a much faster time frame. The optimization objective helps in determining the droop settings and battery requirement for each DER system to meet the economical and secure operation in this work. The outputs from the secondary controller are given to the primary controller as reference values to work towards second-second power balance. The centralized controller is a model based optimization problem which aids in accurate prediction of the reference values given to the primary controller based on predicted/forecasted renewable generation and load data.

As frequency and voltage regulation require both active and reactive power support from the inverter based system a complex calculation is made to allocate them proportionally to maintain stability in the system with operating points within limits.

The droop values are constrained by an upper and lower bound to ensure that the frequency and voltage deviations are within the required bandwidth. The secondary controller must also ensure that the high deviations caused due to the droop control action are taken care by utilizing a PI controller to minimize the deviations to zero after a heavy unbalance between generation and load.

6.3. Cost of Generation and Operation of DERs

This work incorporated the use of Li-ion battery-based energy storage systems (BESS). Li-ion batteries have the flexibility to expand its module size and discharge time,

compared to other technologies. They are widely being implemented in various areas of grid services, but their operation capacity deteriorates with time.

Battery life cycle can be defined as the number of cycles after which the battery performance has degraded to a fixed level. Hence, every charge or discharge cycle accumulates an additional cost. The additional cost, added per charge or discharge of the energy storage system, depends on the depth of discharge and the variation in frequency in the rate of charge or discharge. Thus, in addition to the \$/kW and \$/kWh, the life-cycle cost was considered. During the life of a battery there is a fixed number of charge/discharge cycles. Therefore, it should be made sure that there is only one/discharge cycle during the day by taking into consideration a two-tariff price model based on the on/off load electricity prices.

6.4. Literature Review

In [63], a distributed energy management system (EMS) for a microgrid is proposed which takes into consideration the distribution network parameters and operation constraints. Both local and central controllers worked together to perform an optimal schedule. In [34], a three stage droop based optimal power flow (OPF) scheme for islanded operation is proposed to meet both reliable and economical objectives in the presence of DGs and PEVs penetration while taking consideration of both frequency and voltage constraints which is important for the islanded operation. In [64], a rule based multi-time scale operation in a microgrid is proposed to manage generation operation costs of variable sources along with fuel based sources, demand response, storage SoC management within a single framework but did not take into consideration the network model and operating constraints. In [65], an EMS for droop enabled DGs in a microgrid

to schedule an optimized economic dispatch is proposed while taking into consideration the microgrid stability when choosing the droop parameters. The generation schedule only involved fuel based DGs without taking into consideration the variable DGs which are becoming more common these days. In [66], a multistage cost minimization operation for VSC based fuel operated generators in a microgrid is proposed while taking into consideration the small signal stability along with active and reactive power sharing to maintain frequency and voltage constraints. In [67], bids from DG sources and loads are considered in a market environment to maximize the profits while implementing a central controller in a microgrid. In [68], a network reconfiguration and economic dispatch optimization algorithm is implemented while forecasting the variable generation sources and load data. In [69], a multi-objective optimization is preferred to find a compromise between economic scheduling based fuel costs and emission reduction in a radial microgrid system while taking into consideration the system voltage constraints. In [70], a two stage hierarchical optimization is proposed for a microgrid operation where the lower level aims at optimal generation planning for DERs by maximizing the renewable generation and maintain the schedule in a day ahead planning operation whereas the upper level aims at minimizing the total cost by economically scheduling the generation.

6.5. Theory and Proposed Solution

Microgrids aid in better handling and management of DGs, battery energy sources and controllable loads in the low and medium voltage networks. The key feature of a microgrid is the ability to operate as an island by using the generation capability of the distributed energy resources (DERs). One of the main challenges in an isolated microgrid is the operation of RDGs to meet the demand, as both are intermittent in nature. In

isolated microgrids, DDGs need to be present to take care of the imbalance and maintain voltage/frequency within limits. Batteries have proved to have multi-functional capabilities when integrated in parallel with an intermittent source in islanded microgrids. With expected lower battery costs, it could be expected that high scale RDGs would be equipped with storage devices to make the hybrid system dispatchable for both control and optimal power flow. When a PV is connected in parallel with a battery they can emulate the characteristics of a conventional generator which is essential to maintain the power quality in an isolated microgrid.

6.5.1. Islanded Operation

When the microgrid is operated in the islanded mode the DERs could be operated in load sharing droop control mode. The advantage of utilizing a droop based controller for each DER system is that the frequency and voltage can be regulated automatically without communications through a centralized controller. When the microgrid is in islanded mode, parallel DERs could behave as voltage sources to share the burden of regulating the voltage and frequency. Though the hybrid systems and DDGs can be automatically controlled, a centralized optimization controller could be adopted to manage generation to supply loads in the secondary control loop during the islanded period. The secondary control level is where the M-EMS is implemented to meet the reliable, secure and economic operation. Secondary control is the highest level of control in an individual islanded microgrid, essentially utilizing a centralized optimization function to determine the set points for the DERs based on a global objective and operates on a much slower time frame as compared to the primary controller. The slower time frame gives the secondary controller enough time to perform complex calculations

as compared to the primary controller action which needs to be implemented at a much faster rate. The optimization objective helps in determining the droop settings for each DER system. The outputs from the secondary controller are given to the primary controller as reference values to work towards second-second power balance. The centralized controller is a model based optimization problem which aids in the prediction of the reference values given to the primary controller based on predicted/forecasted generation and load data. For better frequency regulation it is recommended to have all the DERs in the microgrid to participate in frequency regulation based on droop control to avoid high frequency fluctuations due to either a high load drop or high PV variations.

6.5.2. Modified Droop Operation

In microgrids that have high resistive line components, the inverter interfaced generators control system can be modified by including a virtual output resistance in the loop to emulate an inverter side resistance. This increases the stability to share linear and non-linear loads more accurately which is obtained by the provision of higher damping. In networks with higher resistive components there is a higher coupling between the active power and the grid voltage; and the reactive power and the phase angle. The voltage-based droop control for an inverter interfaced source is shown in Figure 6.1(a) [71].

In order to modify the behavior of a DDG based synchronous generator to comply with the modified droop, it is necessary to control the mechanical input of DDG synchronous generator $P_{DDG_{i,b,t}}^{\text{mech}}$ and back-emf of DDG synchronous generator field, $E_{DDG_{i,b,t}}^{\text{field}}$ indirectly. As $\omega_{\text{sys}} / \theta$ can be controlled by $P_{DDG_{i,b,t}}^{\text{mech}}$ and the terminal voltage

6.6. Microgrid Operation Constraints

In an islanded operation, the frequency and voltage deviations are dependent on the reactive and active power imbalances. The power flow equations are modified to accommodate frequency dependent terms for the DER systems to perform the power balance and indirectly maintain the frequency and voltage deviations with its limits. Hence a common frequency deviation term is added as a new state variable in the power flow equations. For an islanded microgrid, the conventional Newton Raphson (NR) method is modified to accommodate the droop based control terms to the DG buses. The mathematical formulation of the proposed power flow algorithm along with DGs and battery constraints are mentioned in the sub-sections below.

6.6.1. Droop Constraints

The drop controlled active power output of the DDG/ hybrid system represented by $P_{DDG_{i,b,t}} / P_{Hyb_{j,b,t}}$, are shown in (6.1) and (6.2). In case of the hybrid system, when the battery $SoC \geq 0.2$, the inverter is rated based on the maximum capacities of RDG and battery to control the output. When the battery $SoC \leq 0.2$, the inverter is limited to the MPP of the RDG to control the output. When the battery $SoC \leq 0.2$, the inverter is operated as a current source in the grid feeding mode operating at its maximum possible output while the rest of the DDGs fix the voltages when drooped with the active power.

$$P_{DDG_{i,b,t}} = P_{DDG_{i,b}}^0 - \left(V_{DDG_{i,b,t}} - V^0 \right) / m_{DDG_{i,b,t}}^p \quad (6.1)$$

$$P_{Hyb_{j,b,t}} = P_{Hyb_{j,b}}^0 - \left(V_{Hyb_{j,b,t}} - V^0 \right) / m_{Hyb_{j,b,t}}^p \quad (6.2)$$

where V^0 is the nominal set point of voltages. $P_{DDG_{i,b}}^0 / P_{Hyb_{i,b}}^0$ is the nominal set points of active power output of the DDG i / hybrid system j connected at bus b . $P_{DDG_{i,b,t}} / P_{Hyb_{j,b,t}}$ is the active power output of the DDG i / hybrid system j connected at bus b at time t . $V_{DDG_{i,b,t}} / V_{Hyb_{j,b,t}}$ is the voltage at the AC terminals DDG i / hybrid system j connected at bus b at time t . $m_{DDG_{i,b,t}} / m_{Hyb_{j,b,t}}$ is the active power droop gains of DDG i / hybrid system j connected at bus b at time t .

The optimization routine is initiated at time instant, t_0 and is performed for every time interval z with a spacing of Δt min as given by (6.3) and (6.4).

$$t = t_0 + z\Delta t \quad \forall z \in N_z \quad (6.3)$$

where

$$N_z = 0, 1, 2, \dots, n_z \quad (6.4)$$

where n_z is the number of z intervals. N_z is the set of time intervals z . $P_{Hyb_{j,b,t}}$ is the summation of the power output of the RDG j connected at bus b at time t , $P_{RDG_{j,b,t}}$ and power output of the battery j connected at bus b at time t , $P_{Bat_{j,b,t}}$ as shown in (6.5). They are connected in parallel to the common DC bus of the inverter input side input.

$$P_{Hyb_{j,b,t}} = P_{RGG_{j,b,t}} + P_{Bat_{j,b,t}} \quad (6.5)$$

$P_{Bat_{j,b,t}}$ could either be a discharging or charging process controlled by the discharging/charging decisions of battery j connected at bus b at time t ,

$U_{Bat_{j,b,t}}^{dis} / U_{Bat_{j,b,t}}^{ch}$. Where $U_{Bat_{j,b,t}}^{dis} / U_{Bat_{j,b,t}}^{ch} \in \{0, 1\}$. $P_{Bat_{j,b,t}}$ is represented by (6.6).

$$P_{Bat\ j,b,t} = \left(U_{Bat\ j,b,t}^{dis} \frac{P_{Bat\ j,b,t}^{dis}}{60\eta_{dis}} - U_{Bat\ j,b,t}^{ch} \frac{P_{Bat\ j,b,t}^{ch}\eta_{ch}}{60} \right) \quad (6.6)$$

where $P_{Bat\ j,b,t}^{dis} / P_{Bat\ j,b,t}^{ch}$ is the discharging/charging powers of battery j connected at bus b at time t . The limits of the summation of $U_{Bat\ j,b,t}^{dis}$ and $U_{Bat\ j,b,t}^{ch}$ is given by (6.7).

$$U_{Bat\ j,b,t}^{dis} + U_{Bat\ j,b,t}^{ch} \leq 1 \quad (6.7)$$

The active power output from the DERs can be controlled by adjusting the variable droops. The limits of the droop are given by (6.8) and (6.9).

$$-5\% \frac{|V|^{max} - |V|^{min}}{P_{DDG\ i,b}^{rated}} < m_{DDG\ i,b}^p < 5\% \frac{|V|^{max} - |V|^{min}}{P_{DDG\ i,b}^{rated}} \quad (6.8)$$

$$-5\% \frac{|V|^{max} - |V|^{min}}{P_{Hyb\ j,b}^{rated}} < m_{Hyb\ i,b,t}^p < 5\% \frac{|V|^{max} - |V|^{min}}{P_{Hyb\ j,b}^{rated}} \quad (6.9)$$

where V_{min} / V_{max} is the ANSI standard min/max voltage limit. $P_{DDG\ i,b}^{rated} / P_{Hyb\ j,b}^{rated}$ is the rated active power limit of DDG i / hybrid system j connected at bus b . The droop gains are limited between $\pm 5\%$ to avoid any voltage violation issues on the DER connected buses during the islanded operation. MPPT and droop are local control actions but to meet the centralized objective, the droop parameters can be controlled to meet the two sub-objectives that will be discussed in the next section. The variable droops are used to economically operate the generators to minimize the cost operation. The variable rated reactive power limit of DDG i / hybrid system j connected at bus b at time t , $Q_{DDG\ i,b,t}^{rated} / Q_{Hyb\ j,b,t}^{rated}$ are evaluated by (6.10) and (6.11). The drop controlled reactive power output of the DDG i / hybrid system j connected at bus b at time t , represented by $Q_{DDG\ i,b,t} /$

$Q_{Hybi,b,t}$, are shown in (6.12) and (6.13). The limits of the droop are given by (6.14) and (6.15).

$$Q_{DDGi,b,t}^{rated} = \sqrt{(S_{DDGi,b}^{rated})^2 - (P_{DDGi,b,t})^2} \quad (6.10)$$

$$Q_{Hybj,b,t}^{rated} = \sqrt{(S_{Hybj,b}^{rated})^2 - (P_{Hybj,b,t})^2} \quad (6.11)$$

$$Q_{DDGi,b,t} = Q_{DDGi,b}^0 + (\omega_{sys,t} - \omega^0) / n_{DDGi,b,t}^q \quad (6.12)$$

$$Q_{Hybj,b,t} = Q_{Hybj,b}^0 + (\omega_{sys,t} - \omega^0) / n_{Hybj,b,t}^q \quad (6.13)$$

$$-1\% \frac{\omega^{ub} - \omega^{lb}}{Q_{DDGi,b,t}^{rated}} < n_{DDGi,b,t}^q < 1\% \frac{\omega^{ub} - \omega^{lb}}{Q_{DDGi,b,t}^{rated}} \quad (6.14)$$

$$-1\% \frac{\omega^{ub} - \omega^{lb}}{Q_{Hybj,b,t}^{rated}} < n_{Hybj,b,t}^q < 1\% \frac{\omega^{ub} - \omega^{lb}}{Q_{Hybj,b,t}^{rated}} \quad (6.15)$$

where $S_{DDGi,b}^{rated} / S_{Hybj,b}^{rated}$ is the rated apparent power limit of DDG i / hybrid system j connected at bus b . $Q_{DDGi,b}^0 / Q_{Hybj,b}^0$ is the nominal set points of reactive power output of the DDG i / hybrid system j connected at bus b . ω^0 is the nominal set point of frequency. $\omega_{sys,t}$ is the system frequency at time t . $n_{DDGi,b,t}^q / n_{Hybj,b,t}^q$ is reactive power droop gains of DDG i / hybrid system j connected at bus b at time t . $\omega^{ub} / \omega^{lb}$ is the frequency lower/upper bound. Similar to the voltage, the frequency is limited between $\pm 1\%$ to avoid any synchronization issues among the DERs during islanded operation. The droop values are constrained by $\omega^{ub} / \omega^{lb}$ and $Q_{DDGi,b,t}^{rated}$ to ensure that the frequency deviations are within the required bandwidth.

6.6.2. Battery Constraints

This work incorporated the use of Li-ion battery for RDGs. Li-ion batteries are versatile in module size and discharge time, compared to other technologies. The operation capacity of batteries deteriorates with time. This process occurs due to cumulative changes of the structure and composition of key battery cell components caused by the charge/discharge cycle. Thus, battery life cycle can be defined as the number of cycles after which the battery performance has degraded to a predetermined level. Hence, every charge or discharge cycle accumulates an additional cost. The additional cost, added per charge or discharge of the energy storage system, depends much on the frequency in variation of the rate of charge or discharge while the depth of discharge has little or no effect. Thus, in addition to the discharging/charging rate cost in \$/kWh, the life-cycle cost should be considered. The size of the battery, $Size_{Batb,j}$ is evaluated as the absolute difference between the maximum and the minimum battery energy over the maximum DOD ($DoD_{Batb,j}^{\max} = 0.8$) as given by (6.16).

$$Size_{Batb,j} = \frac{|E_{Batb,j}^{\max} - E_{Batb,j}^{\min}|}{DoD_{Batb,j}^{\max}} \quad (6.16)$$

where $E_{Batb,j}^{\min} / E_{Batb,j}^{\max}$ is the minimum/maximum energy levels of battery j connected at bus b . The daily cycles, $Cycle_{Bat}$ and life in years, $Year_{Bat}$ can be evaluated from (6.17), (6.18) and (6.19).

$$Cycle_{Bat} = \frac{1}{2} \frac{\sum_{t=1}^{144} |E_{Batj,b,t}^{act}|}{DoD_{Batb,j,t} \cdot Size_{Batb,j}} \quad (6.17)$$

where

$$E_{Bat\ j,b,t}^{act} = P_{Bat\ j,b,t} \Delta t \quad (6.18)$$

where is the energy dissipate or absorbed by the battery j at bus b at the end of time t for interval Δt .

$$Year_{Bat} = \frac{CycLife_{Bat}}{Cycle_{Bat} \cdot OpDays_{Bat}} \quad (6.19)$$

where $E_{Bat\ j,b,t}^{act}$ number of operating days, $OpDays_{Bat} = 300$ days and nominal cycle life of battery, $CycLife_{Bat} = 3000$ cycles. The degradation cost of battery j at bus b at the end of time t , $C_{Bat\ j,b,t}^{deg}$ associated with either a charging or discharging cycle with either $P_{Bat\ j,b}^{dis} \Delta t$ dissipated or $P_{Bat\ j,b}^{ch} \Delta t$ absorbed energy is given by (6.20).

$$C_{Bat\ j,b,t}^{deg} = \left| \frac{x_{Bat\ j,b}}{100} \right| \cdot C_{Bat\ j,b}^{UC} \cdot \left(U_{Bat\ j,b,t}^{dis} \frac{P_{Bat\ j,b,t}^{dis}}{60\eta_{dis}} + U_{Bat\ j,b,t}^{ch} \frac{P_{Bat\ j,b,t}^{ch} \eta_{ch}}{60} \right) \cdot \Delta t \quad (6.20)$$

where $x_{Bat\ j,b}$ is the inverse proportionality factor of the battery life with respect to the cycles and $C_{Bat\ j,b,t}^{UC}$ is the unit cost of battery j at bus b at time t . $C_{Bat\ j,b,t}^{UC}$ is the ratio of total cost (\$) over the battery size (kWhr). η_{dis} / η_{ch} is the battery discharging/charging efficiency. The degradation curve is obtained with the assumption that the battery undergoes a round trip cycle by discharging to its $DoD_{Bat,b,j}^{\max}$ point and then charged back to its upper SoC level. The SoC of each battery connected in parallel with the DG at the hybrid system bus at any time t , depends on its SoC at the previous time step and its discharging/charging rate given by (6.21) [72].

$$SoC_{Bat\ j,b,t} = SoC_{Bat\ j,b,t-\Delta t} - \frac{E_{Bat\ j,b,t}^{act}}{Size_{Bat\ b,j,t}} \quad (6.21)$$

where $SoC_{Bat\ j,b,t-\Delta t}$ and $SoC_{Bat\ j,b,t}$ are the previous and current SoCs of the battery j at bus b at time $t-\Delta t$ and t respectively. $SoC_{Bat\ j,b,t}$ is limited by the minimum state of charge (SoC) level of the battery, SoC^{\min} and maximum state of charge (SoC) level of the battery, SoC^{\max} as shown in **Error! Reference source not found.**

$$SoC^{\min} < SoC_{Bat,i} < SoC^{\max} \quad (6.22)$$

For added security to ensure that battery power or energy does not exceed their boundary limits during charge/discharge management, the battery constraints are established as shown in (6.23), (6.24) and (6.25).

$$P_{Bat\ j,b,t}^{dis} < U_{Bat\ j,b,t}^{dis} P_{Bat\ j,b}^{rated} \quad (6.23)$$

$$P_{Bat\ j,b,t}^{ch} < U_{Bat\ j,b,t}^{ch} P_{Bat\ j,b}^{rated} \quad (6.24)$$

$$E_{Bat\ j,b}^{\min} < E_{Bat\ j,b,t}^{act} < E_{Bat\ j,b}^{\max} \quad (6.25)$$

where $P_{Bat\ j,b}^{rated}$ is the rated power limit of battery j connected at bus b . $E_{Bat\ b,j}^{\min} / E_{Bat\ b,j}^{\max}$ is the minimum/maximum energy levels of battery j connected at bus b at time t .

6.6.3. Power Flow

For the islanded microgrid, the 5 DGs are considered as negative loads. The active and reactive powers are functions of voltage and frequency deviations respectively [73]. The power flow balance at each bus is dictated by the Newton Raphson (NR) steady state power balance equations as shown in (6.26) and (6.27).

$$\begin{aligned}
\Delta P_{b,t} \{ \Delta \omega, \delta, V \} &= \sum_{k=1}^{n_k} V_{b,t} V_{k,t} Y_{bk} \cos(\delta_{b,t} - \delta_{k,t} - \theta_{bk}) \\
&\quad - \left(P_{DDG_{i,b,t}} \{ \Delta V \} - P_{Hyb_{j,b,t}} \{ \Delta V \} - P_{L_{b,t}} \{ V, \Delta \omega \} \right) \\
&= P_{S_{b,t}} - \left(P_{DDG_{i,b,t}} - P_{Hyb_{j,b,t}} - P_{L_{b,t}} \right)
\end{aligned} \tag{6.26}$$

$$\begin{aligned}
\Delta Q_{b,t} \{ \Delta \omega, \delta, V \} &= \sum_{k=1}^{n_k} V_b V_k Y_{bk} \sin(\delta_b - \delta_k - \theta_{bk}) \\
&\quad - \left(Q_{DDG_{i,b,t}} \{ \Delta \omega \} - Q_{Hyb_{j,b,t}} \{ \Delta \omega \} - Q_{L_{b,t}} \{ V, \Delta \omega \} \right) \\
&= Q_{S_{b,t}} - \left(Q_{DDG_{i,b,t}} - Q_{Hyb_{j,b,t}} - Q_{L_{b,t}} \right)
\end{aligned} \tag{6.27}$$

where Y_{bk} and θ_{bk} are the magnitude and the angle of the Y-bus admittance matrix of the buses bk , $V_{b,t}/V_{k,t}$ is the voltage and $\delta_{b,t}/\delta_{k,t}$ is the voltage angle at bus b/k at time t . n_k is the number of buses in the microgrid system. $\Delta P_{b,t}/\Delta Q_{b,t}$ is the active/reactive power mismatch at bus b at time t . P_{S_b}/Q_{S_b} is the active/reactive powers injected at the bus b at time t .

6.7. Multi-Period Optimization Procedure

The optimization routines are divided based on the on-peak and off-peak periods. Usually on-load periods are given higher priority as it is the period when major businesses operate and a higher reliability is anticipated. Off-peak periods are low loading periods that require lesser generation to serve loads and batteries could be ideally charged during this period.

6.7.1. On-Peak Period Regulation

The first stage, Stage (I) deals with performing an OPF to reduce the overall microgrid cost by committing the droop controlled DER units accordingly. The economic operation includes reducing the cost of generation of fuel based DDGs and reducing the cost of operation of the batteries. After scheduling the generators based on an economic

operation, the next stage, Stage (II) deals with minimizing the deviation index (i.e., frequency deviation index (FDI)). The on-peak optimization routine is shown in Figure 6.2. N_{Bat} is the set of battery j , N_{BL} is the set of batteries located at bus b . N_{DDG} is the set of DDG i , N_{DL} is the set of DDGs located at bus b . $st1$ and $st2$ are the indices of the stages I and II, respectively.

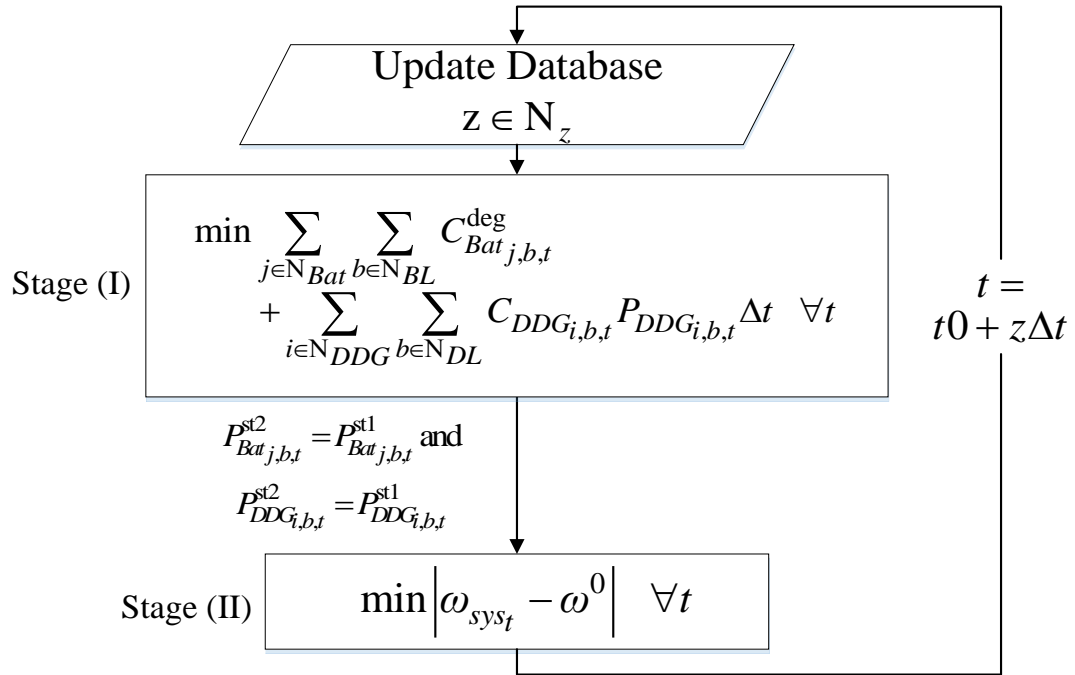


Figure 6.2: On-peak optimization routine flowchart.

6.7.2. Off-Peak Period Regulation

The second optimization routine i.e. off-peak regulation deals with an additional stage of performing a sub-objective function to charge the BESS back to its target SoC levels. This operation prepares the two BESSs for the next day on-peak operation cycle. As batteries are usually drained during the islanded operation a charging scheme for batteries could be performed during the off-peak period when the number of loads that switched on are low. For the charging purpose, the energy could be drawn from the DDGs or

RDGs that operate during the off-peak period. SoC^{target} is the target state of charge for each battery which could be chosen as 70%.

After the microgrid was switched from on-peak to off-peak regulation mode, all the sub-problem minimization objectives, should satisfy the power flow constraints for each bus at each time t . The off-peak period optimization routine is shown in Figure 6.3. st1, st2 and st3 are the indices of the stages I, II and III, receptively.

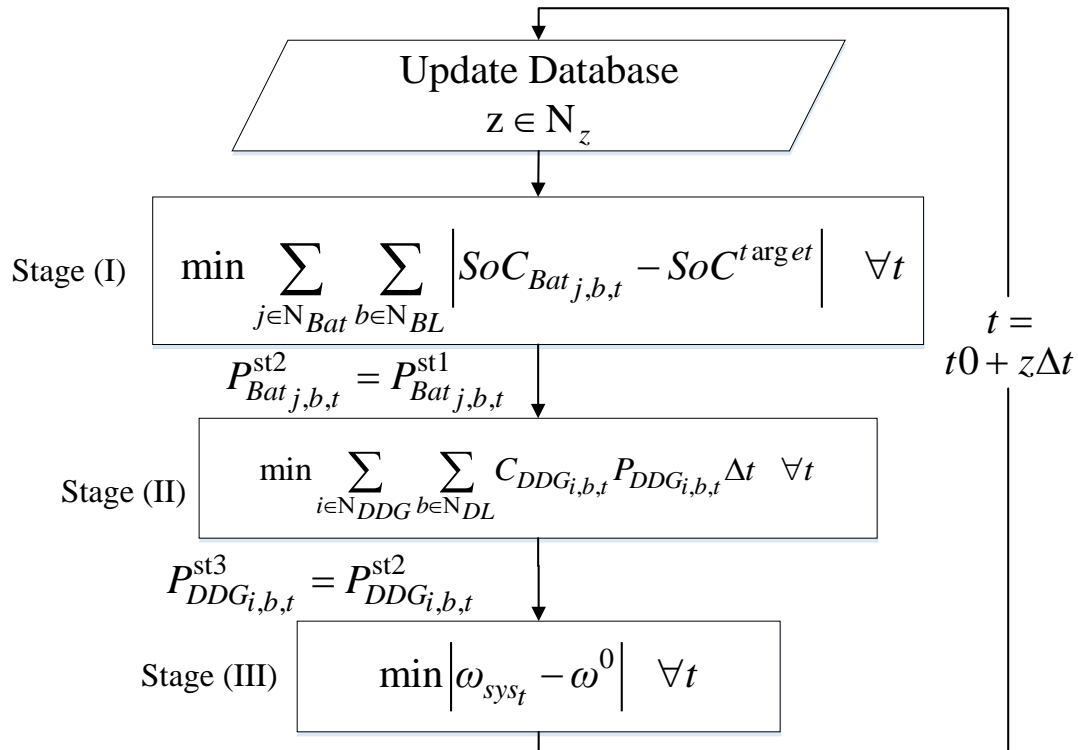


Figure 6.3: Off-peak optimization routine flowchart.

6.8. Case Studies

The system used for performing case studies and showing the effectiveness of the proposed technique is the 33 bus system dealt in many paper. The details of the system can be found in [74]. The schematic of the distribution system is shown in Figure 6.4(a). Figure 6.4(b) shows the solar and wind profiles and Figure 6.4(c) shows the load profiles for residential, commercial and industrial customers. The cost of operation of each fuel

based DDG is shown in the Table 6.1 and the unit cost of batteries of each hybrid system is shown in Table 6.2. It is assumed the cost of operation (\$/kWhr) values are constant for a particular day. The cost of generation is due to different technologies, installation cost, year of installation, life cycle of storage etc. The optimization was performed using MATLAB on a PC using Intel Core I7 CPU and 8 GB RAM and it took a maximum of 47.23 sec to complete the two stage optimization routine. The case studies are performed for the islanded operation during on-peak and off-peak periods.

- 1) To sustain the loads, the rated DDG, forecasted RDG generation and available battery outputs are utilized.
- 2) A generation cost minimization operation is run by following the modified droop enabled generators followed by maintaining frequency regulation operation.
- 3) Whenever a battery that is tied to a DG gets reaches its lower SoC it gets disconnected and the DG is operated as a current source
- 4) In case the two batteries reach the lower SoC and the microgrid operating in islanded mode would require the
- 5) DDGs to operate as voltage and frequency sources to maintain regular operation.
- 6) In case both the RDGs and batteries lose their ability to produce any more outputs the burden to maintain stability and sustain the loads falls on the DDGs.
- 7) During off-peak period when the batteries are drained out, they need to be charged back to their target levels for the next day on-peak operation. A multi-stage optimization is run with an additional objective to minimize the gap between current SoC and target SoC.

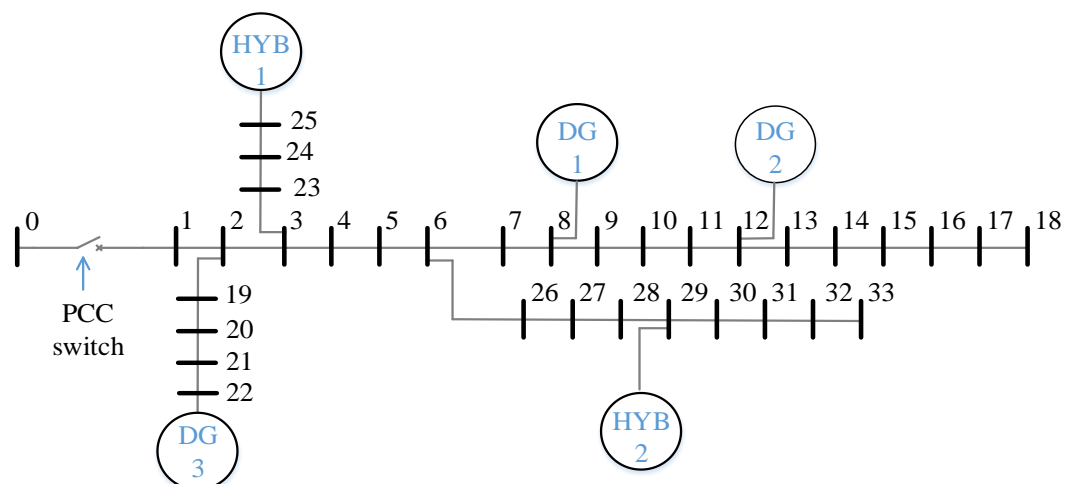
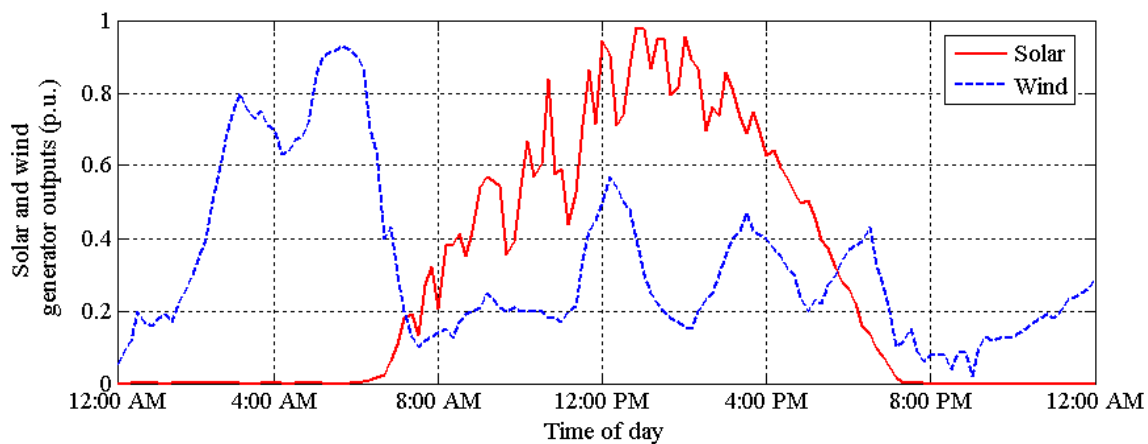


Figure 6.4: 33-bus test system operating as a microgrid in both grid-connected and islanded mode. Data about system loads and line impedances can be found in [74].

Figure 6.5(a) shows the solar and wind generator outputs and Figure 6.5(b) shows the load profiles for residential, commercial and industrial customers.



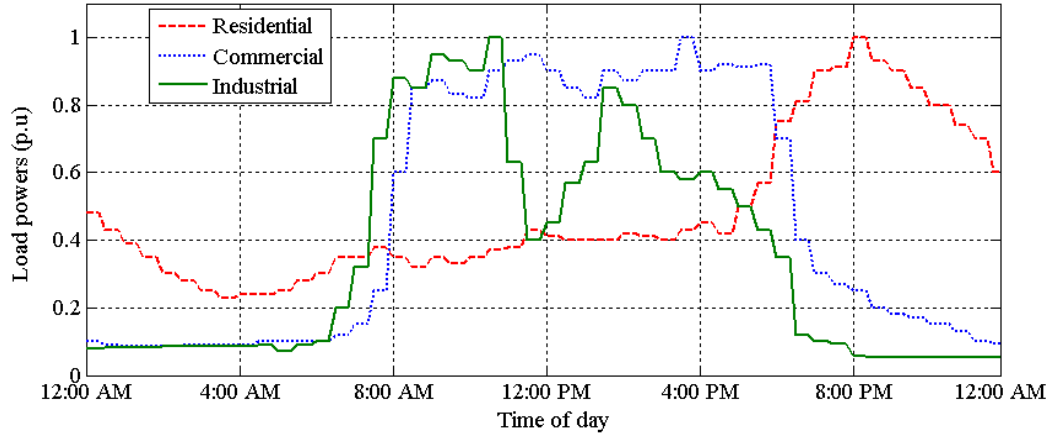


Figure 6.5: (a) Solar and wind source profiles, (b) Load profiles.

Table 6.1: Droop-Controlled DDGs: locations, ratings and cost of operation

DDG#	Bus #	S_{Gmax} (MVA)	$C_{DDG_{i,b,t}}$ (\$/kWhr)
1	8	1.5	0.02
2	12	2	0.024
3	22	1	0.029

Table 6.2: Droop-Controlled RDG/battery hybrid systems: locations, type, ratings, and battery unit cost.

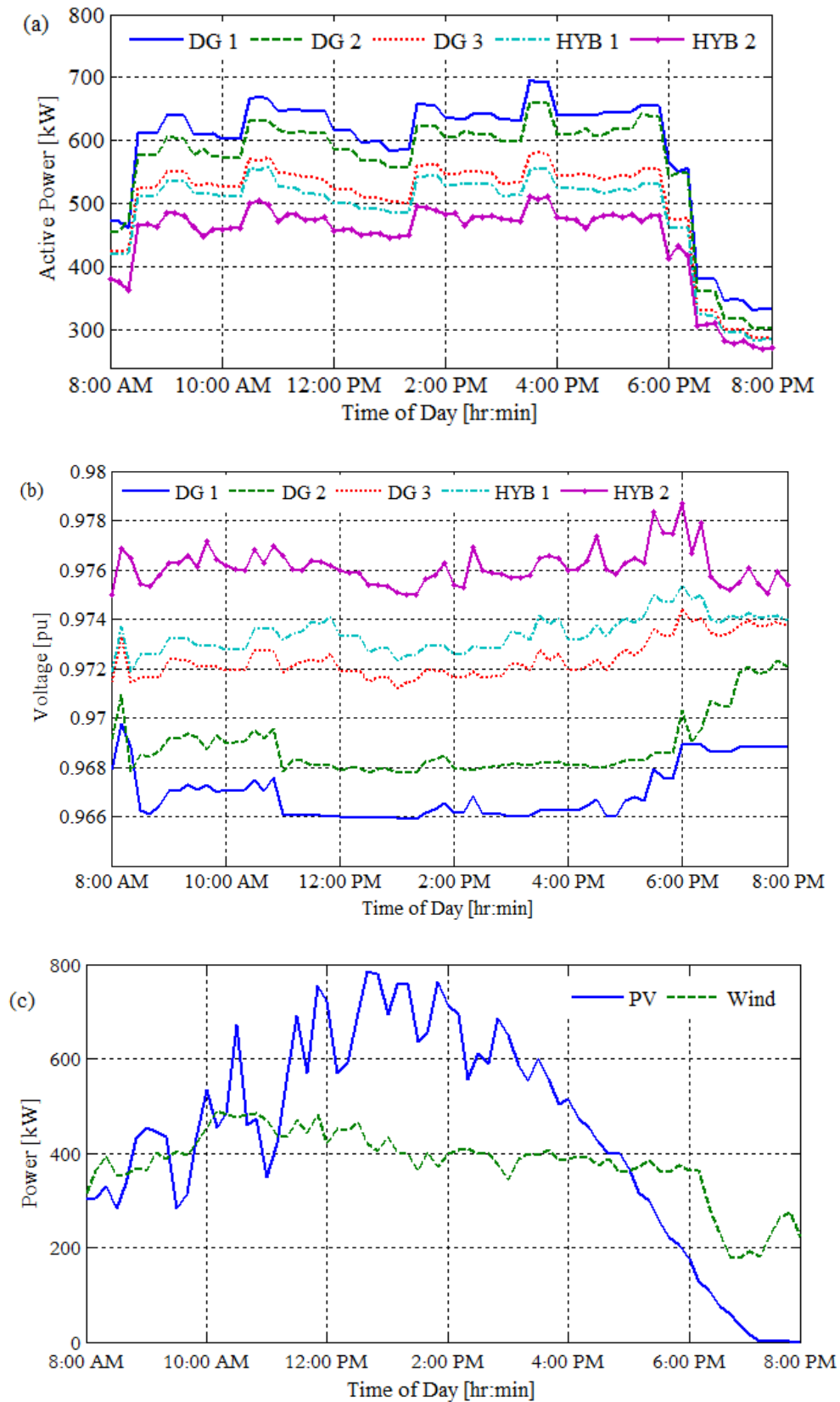
Hyb#	Bus #	RDG type	RDG (MW)/ Battery (MWhr)	$C_{Bat_{j,b}}^{UC}$ (\$/kWhr)
1	25	PV	0.8 /0.4	250
2	28	Wind	0.9 /0.45	310

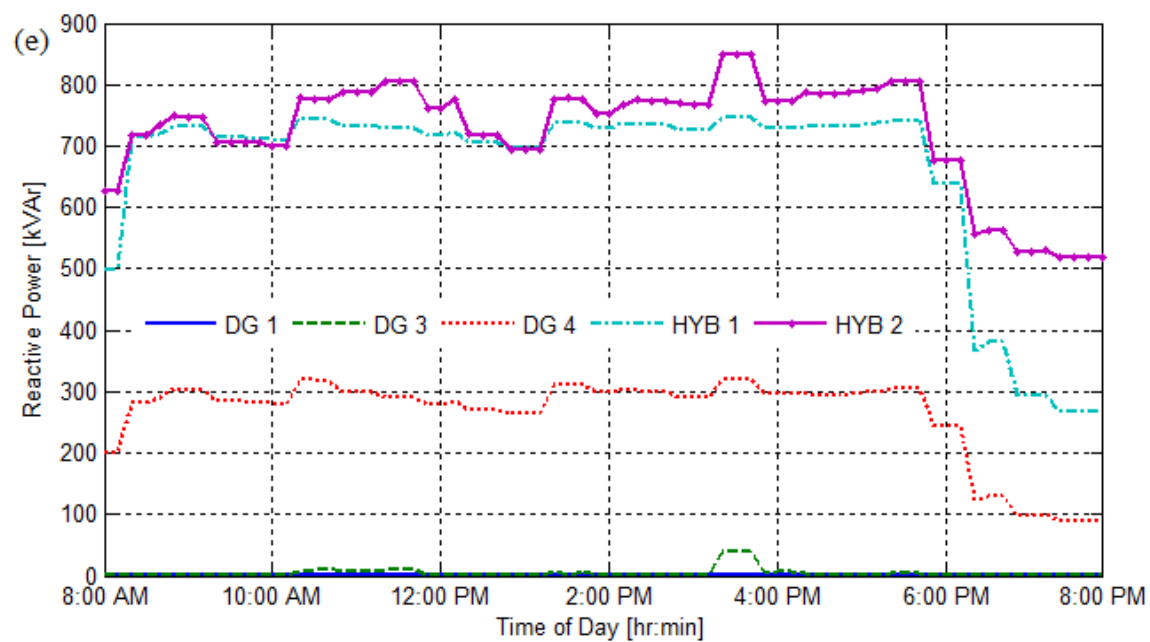
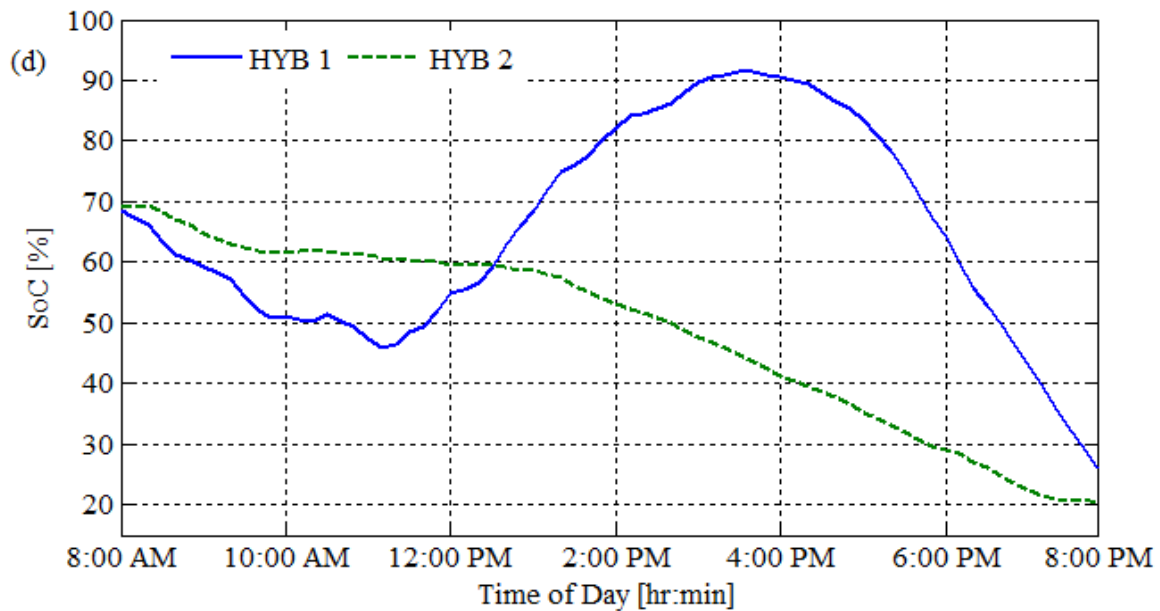
6.8.1. On-Peak Period Operation

The microgrid operation studies were performed first during the on-peak period time for an islanded mode operation, where all the distributed generators along with the hybrid systems are operated in droop mode to mimic synchronous generator in the main grid. The batteries are all assumed to be charged at nominal values which give the battery the ability to either charge or discharge based on the total forecasted loads in the system. The on-peak period operation of the islanded system begins at 8:00 AM. For the first level of the operation, an economical operation is performed with the forecasted generation and

load as inputs to the database which is subjected to constraints as mentioned above. Figure 6.6(a) shows the scheduled active power outputs from the three distributed generators and the two hybrid systems. It can be seen from the results that the DGs are scheduled according to their cost of operation while the batteries are scheduled to minimize their usage to increase their lifetime. The voltages are drooped with DER active power injection. The voltages are not regulated directly but must be maintained within the ANSI standards. The power outputs of the forecasted PV and wind generators operating at their respective maximum power points are shown in Figure 6.6 (b). The forecasted PV and wind outputs operating at their respective maximum power points are shown in Figure 6.6(c). The SoCs of the batteries tied to the hybrid systems are shown in Figure 6.6(d). At around 3:40 PM the battery tied to the PV system reaches its maximum SoC level while at around 8:00 PM both the batteries reach low SoC level which causes the hybrid system to operate in droop mode.

For the second level the scheduled distributed generation active power along with the scheduled battery information is transferred from stage I. The transferred information remains fixed while trying to minimize the frequency deviation by controlling the reactive power support. Figure 6.6(e) shows the reactive power support from the distributed generation and the hybrid systems. Figure 6.6(f) shows a comparison between the uncontrolled frequency in the first level and the controlled frequency in the second level. It can be seen that the frequency deviation is minimized to negligible levels in the second stage.





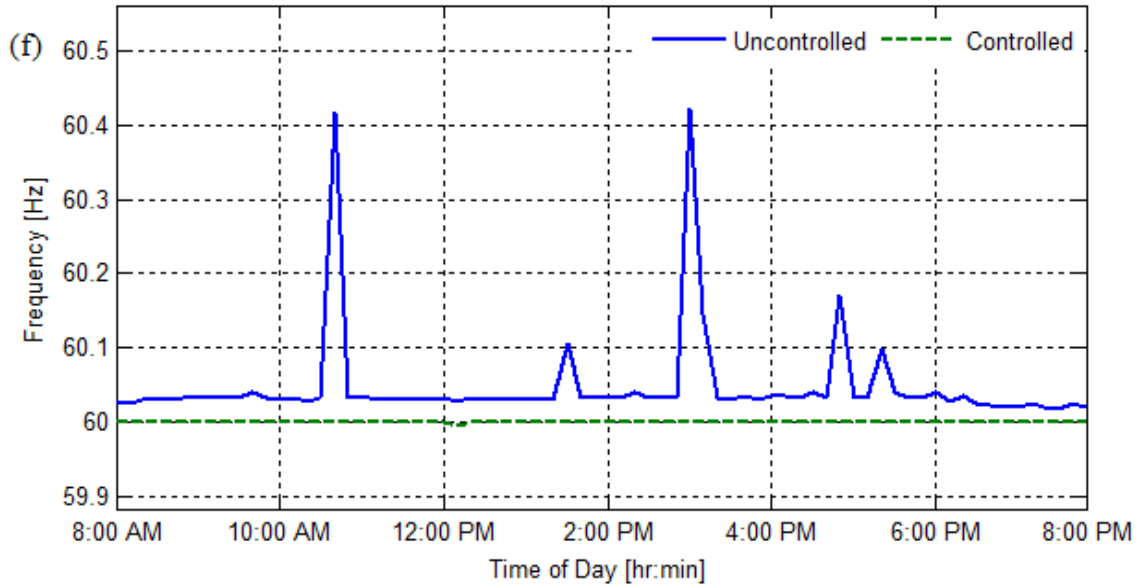


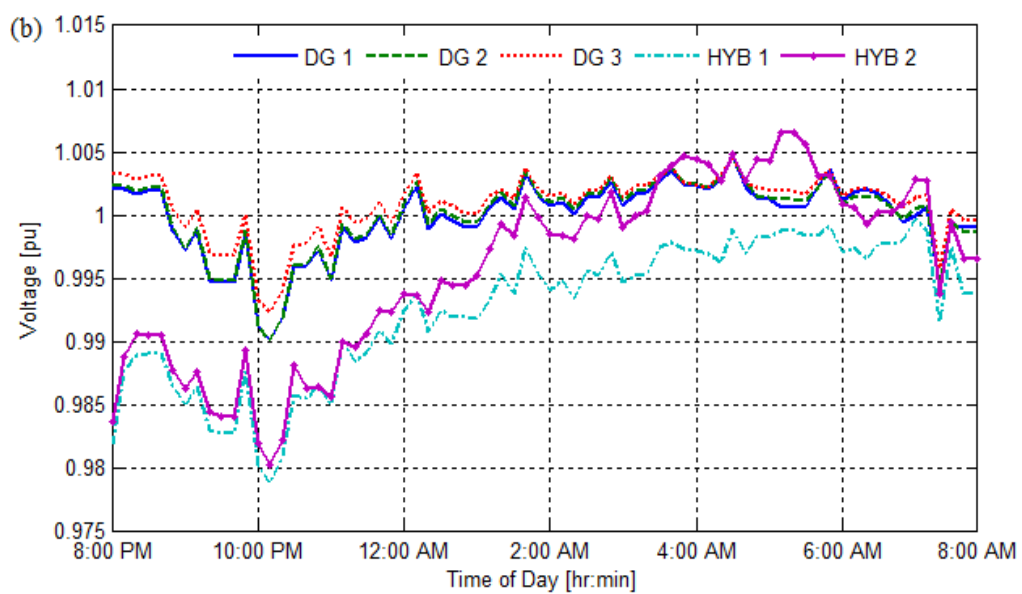
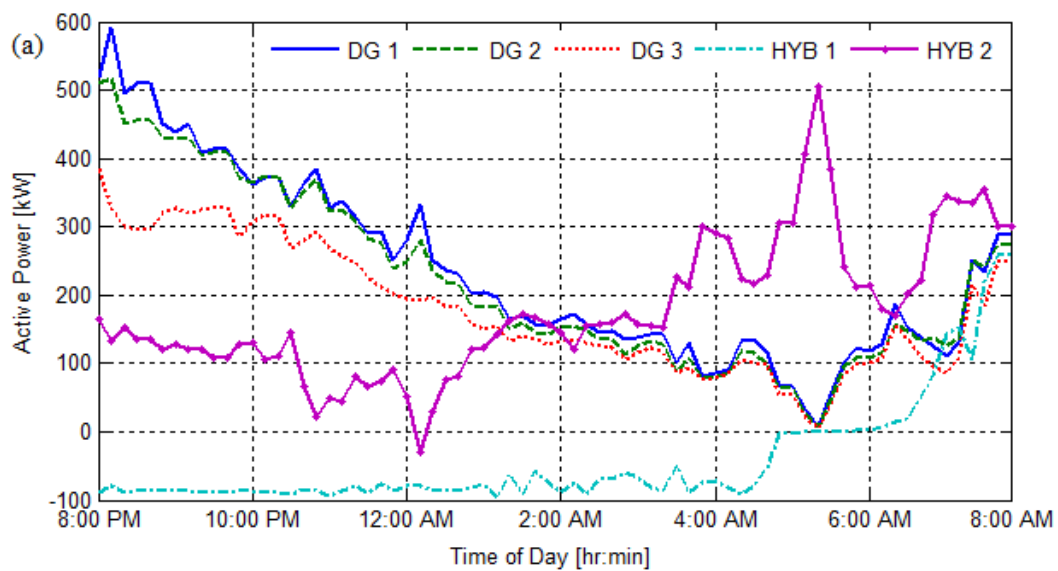
Figure 6.6: On-peak period operation (a) Active power outputs (b) Voltages at the source nodes (c) PV and wind maximum power point outputs (d) SoCs of the batteries (e) Reactive power outputs and (f) frequency comparison of uncontrolled and controlled operation.

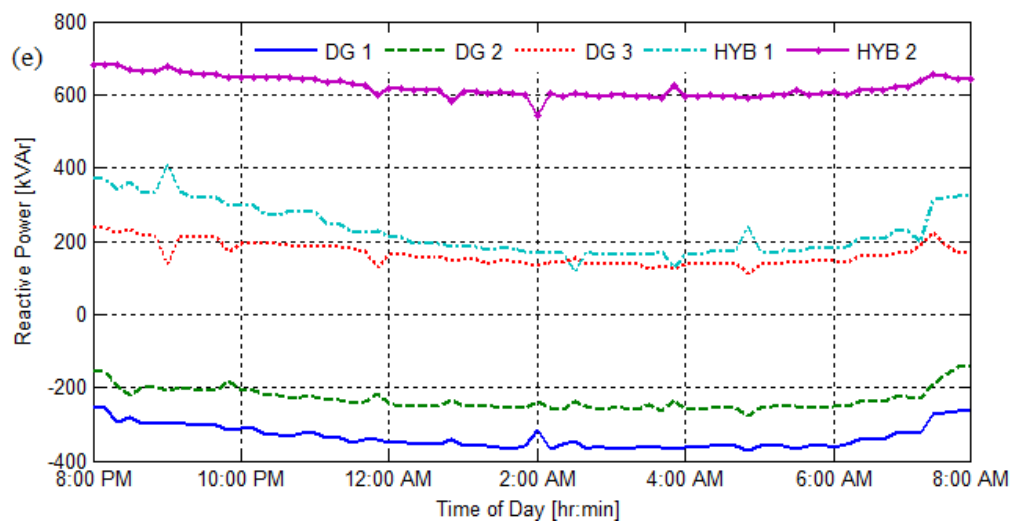
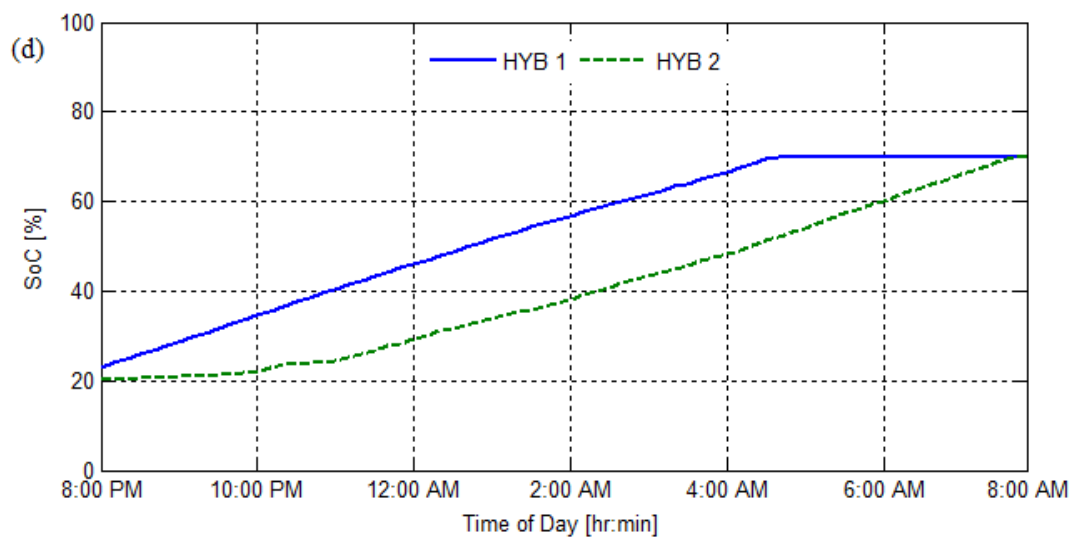
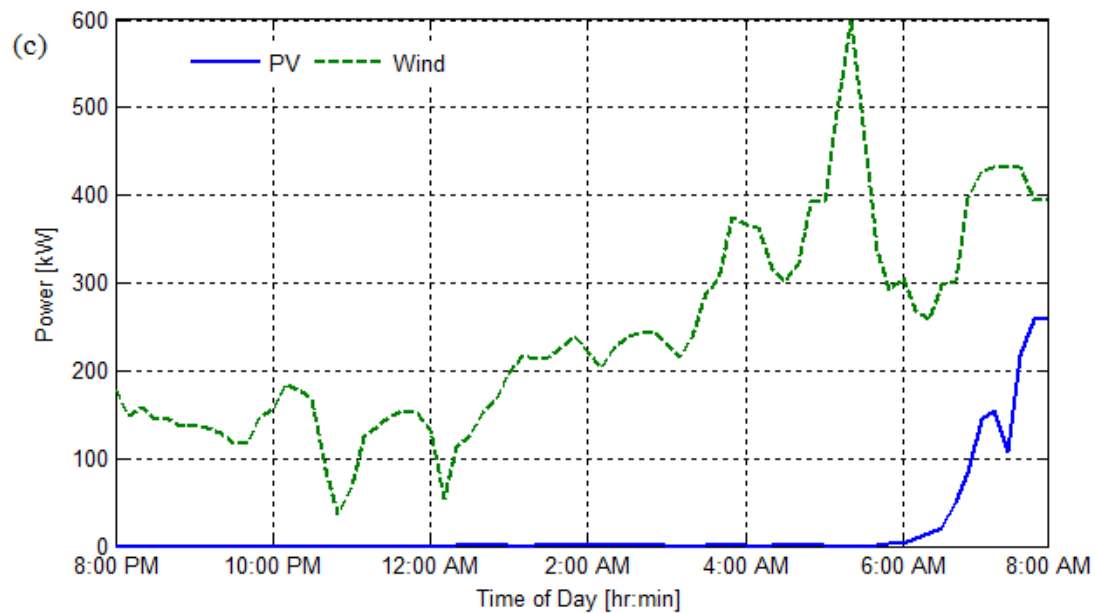
6.8.2. Off-Peak Period Operation

The microgrid operation studies were performed next during the off-peak period for an islanded mode operation, where the distributed generators are operated in droop mode to mimic synchronous generator in the main grid while the hybrid systems are operated in grid feeding mode to charge the batteries back to nominal levels for on-peak period operation. The batteries are all assumed to reach low levels of SoC. Battery charging during the off-peak period is ideal as the number of loads are low along with the lower retail rates. The off-peak period operation of the islanded system begins at 8:00 PM. For the first level of the operation, the deviation between the current SoC and the nominal SoC level is minimized. The scheduled battery levels are transferred to the next level. In the second level, an economical operation is performed with the forecasted generation and load as inputs to the database which is subjected to constraints as mentioned above. Figure 6.7(a) shows the scheduled active power outputs from the three distributed

generators and the two hybrid systems. It can be seen from the results that the DGs are scheduled according to their cost of operation while the hybrid system active power outputs is the summation of the renewable maximum power points and the batteries at the charging level. The voltages are drooped with DER active power injection. The voltages are not regulated directly but must be maintained within the ANSI standards. The power outputs of the forecasted PV and wind generators operating at their respective maximum power points are shown in Figure 6.7(b). The forecasted PV and wind outputs operating at their respective maximum power points are shown in Figure 6.7(c). The SoCs of the batteries tied to the hybrid systems are shown in Figure 6.7(d). The battery tied to the HYB 1 reaches its nominal SoC level at around 4:30 AM while the battery tied to the HYB 2 reaches its nominal SoC level at around 8:00 AM.

For the third level the scheduled distributed generation active power along with the scheduled battery information is transferred from stages I and II. The transferred information remain fixed while trying to minimize the frequency deviation by controlling the reactive power support. Figure 6.7(e) shows the reactive power support from the distributed generation and the hybrid systems. Figure 6.7(f) shows a comparison between the uncontrolled frequency in the first level and the controlled frequency in the second level. It can be seen that the frequency deviation is minimized to negligible levels in the second stage.





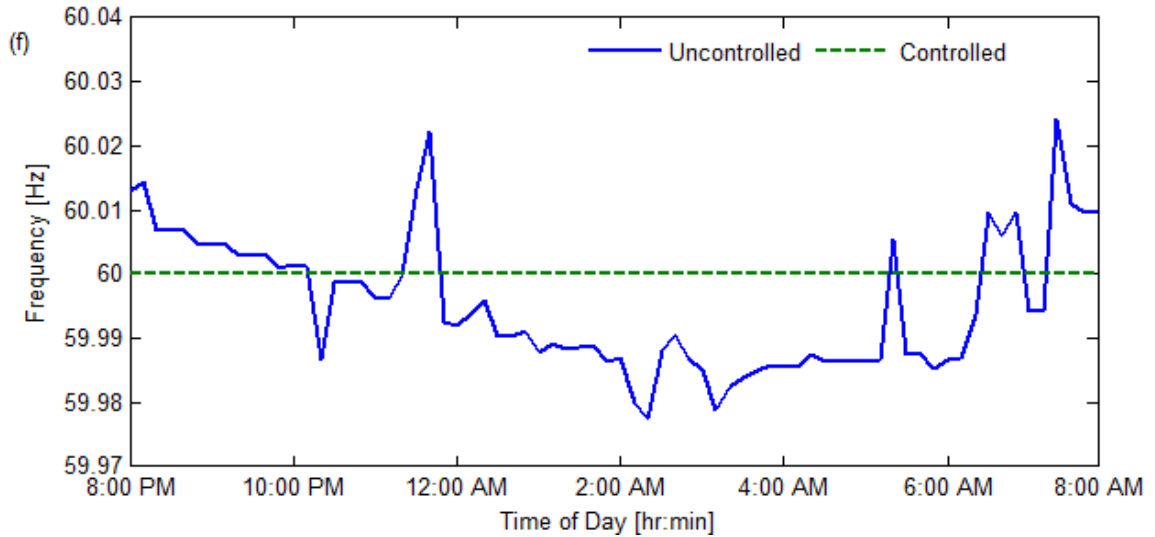


Figure 6.7: Off-peak period operation (a) Active power outputs (b) Voltages at the source nodes (c) PV and wind maximum power point outputs (d) SoCs of the batteries (e) Reactive power outputs and (f) frequency comparison of uncontrolled and controlled operation.

6.9. Summary

A microgrid operation for power regulation was discussed for an islanded operation based on the period of day. For on-peak period, a two stage optimization strategy based on economic and frequency deviation objectives was developed. The microgrid energy management system (M-EMS) sustained the loads and then performed an economic generation scheduling based on a secondary optimization control strategy with the help of several droop enabled DDGs and hybrid systems. When the batteries reached their minimum SoC, the batteries got disconnected, allowing the inverters to operate in grid feeding mode to supply power based on the MPPT of RDGs. During the off-peak period, a multi-stage optimization strategy is suggested to charge the batteries back to their nominal values and perform regular operation. The BESS utilization was leveraged based on the time of day and usage patterns, as the charging was performed during lower load periods and power supply operation was performed during the high load periods. Results

showed the proposed scheduling strategy based on the microgrid system characteristics would benefit in scheduling distributed generation efficiently.

CHAPTER 7 : FINAL CONCLUSIONS, CONTRIBUTIONS AND FUTURE WORK

The motivation behind this dissertation work is the large scale renewable distributed generator (RDG) installations on the distribution feeders. This work contributes towards the ongoing research in implementing advanced control features to large inverters when tied with renewable generation sources on the distribution networks and microgrids where the application is more prevalent, to solve power quality and economic operation challenges by applying a number of directed management strategies. The general topics included in this work were unbalanced distribution networks, use of battery energy storage with large scale PV farms, microgrid operation, distributed and centralized optimization control strategies.

7.1. Concluding Remarks

For *Task 1*, the smart inverter capability of controlling both active and reactive power was discussed, to take care of the high ramp rate issues arising from transient cloud movement which causes overvoltage and flicker issues. *Task 1* was described in **Chapters 2 and 3**. In **Chapter 2**, the conventional voltage regulators and dynamically operated smart inverter were utilized locally to deal with over-voltage and regulator high tap changes. When a dynamic VAr regulator (DVR) was utilized, it proved insufficient to mitigate the high voltage swings that caused voltage violations along with excessive tap changes. A novel local ramp-rate control strategy was utilized based on a battery SoC dependent dynamically varying ramp threshold, to control the active power locally. The

local control strategy to control the active power did not utilize the voltage measurements and simply delayed the rate of rise of active power, giving enough time for the voltage regulators to react in time based on their time delays. The strategy proved to be an effective solution for minimizing voltage fluctuation as the coupling between active power injections and nodal voltages was significantly high. In **Chapter 3**, a novel distributed voltage control (DVC) strategy was discussed, that utilized smart inverter along with other conventional voltage regulating devices on the same MV system. The DVC scheme where both dynamic active and reactive power control was performed to mitigate the high ramp rate issues, proved to be a better solution with regards to voltage regulation and usage of conventional voltage regulators as compared to the other cases. The DVC scheme utilized the feeder sensitivity information database along with forecasted PV/load inputs to perform the online control of inverter when the voltage violations were observed. A novel ramp thresholding technique was utilized to minimize the rate of rise/drop of power as well as maintain battery SOC's within bounds by controlling the charging/discharging rate indirectly. The DVC scheme is a better strategy to involve all the regulators through communications while working on local objectives. It reduced the over-utilization of conventional voltage regulators, which in turn reduces the wear and tear. For **Task 1**, the capability of the smart inverter was applied to a radial MV distribution feeder in a California utility service territory.

For **Task 2**, an offline centralized management strategy was utilized to meet the different objectives on the same MV distribution system as used in **Task 1** and described in **Chapter 4**. The smart inverter capability of reactive power control and active power curtailment was utilized to run multi-objective functions at different stages based on

cascaded regulator time delay operation. The novelty in this planning strategy is the reduced utilization of regulators that are downstream, as typically the voltage regulation performed by regulators upstream is enough to maintain the node voltages within the safe band across the feeder. It is a better solution for large feeders with large scale DG penetration.

For *Task 3*, the smart inverter control aiding in power regulation of renewable distributed generators (RDGs) was described in **Chapters 5 and 6**. In **Chapter 5**, a number of inverter interfaced hybrid RDG/battery systems were integrated into a microgrid to allow RDGs to more flexible in power regulation. Tests performed with hybrid systems validates the utilization of RDGs as dispatchable generators that could react to set-points. In **Chapter 6**, the 33 bus system was utilized as a microgrid to implement various smart inverter capabilities while operating in islanded mode. The droop controls were modified from the conventional P-f/V-Q to P-V/Q-f droop controls, to allow active power regulation to be performed based on cost minimization and reactive power regulation based on frequency deviation minimization optimization strategies. The coupling of P-V and Q-f droop controls along with multi-stage optimization makes sure there is no interference of one objective with another objective. While in islanded mode, the droop-based DERs were controlled based on generation cost and battery utilization by following a centralized multi-objective optimization based management strategy. The operations were divided into on-peak and off-peak periods. The batteries were typically utilized for power supply during the on-peak period and charged during the off-peak period. This management strategy improves the reliability in a microgrid for regular operation. After performing the offline multi-stage optimization algorithm at the

secondary level within the planning horizon, the optimal DG droop set-points are transferred to the primary level for real time fast-acting local DER operation while taking care of any mismatches.

7.2. Directions for Future Work

A few general directions which the future research could follow are provided below.

- For **Tasks 1 and 2**, a large power plant interfaced with a central smart inverter was considered in a MV system, along with voltage regulators to maintain the power quality by utilizing both distributed and centralized management schemes. Most of the residential loads are connected to the low-voltage (LV) networks that are connected to the MV system. The work could be extended to large scale implementation of distributed rooftop solar at the LV level. The battery utilized to mitigate the ramp rate was located next to the plant. A strategy to control a battery such as a community storage located elsewhere could be considered to mitigate high ramp rate issues and schedule in case of centralized planning. For small scale DGs, ultra-capacitors/fast-acting battery could be utilized to mitigate high ramp rate issues such as flicker that could be more severe locally.
- The optimization for **Tasks 2 and 3** was performed by utilizing commercially available software and relied predominantly on the modeling of the distribution systems. For larger systems performing NLP optimization becomes a daunting task. Therefore, the mathematical modeling could be modified to reduce the search space to reach the optimal setting in lesser time.
- In **Chapter 2**, the proposed DVC scheme was implemented in Matlab/Simulink environment that works on phasor domain time step simulation. The work could be

extended to prove the online power control strategy by utilizing real-time simulators such as RTDS and Opal-RT.

- In **Chapter 6**, a large battery was utilized to support the power generation during on-peak period power regulation. A strategy to optimally size the battery based on multiple loads and renewable power profiles can be performed in future studies.

REFERENCES

- [1] B. Mather et al., *NREL/SCE High Penetration PV Integration Project: FY13 Annual Report*, National Renewable Energy Laboratory, Golden, CO, 2014.
- [2] T. A. Short, "Distributed Generation," *Electric Power Distribution Handbook*: CRC Press, 2003.
- [3] Y. S. Lim, and J. H. Tang, *Creating a Dynamic Load Controller to Mitigate Flickers Caused by Photovoltaic Systems in Cloudy Regions*, University Tunku Abdul Rahman
- [4] *Common Functions of Smart Inverters*, Electric Power Research Institute (EPRI), 2011.
- [5] *Lazard's Levelized Cost of Energy Aanalysis — Version 8.0*, 8.0.
- [6] F. Olivier, P. Aristidou, D. Ernst, and T. Van Cutsem, "Active Management of Low-Voltage Networks for Mitigating Overvoltages Due to Photovoltaic Units," *Smart Grid, IEEE Transactions on*, vol. PP, no. 99, pp. 1-1, 2015.
- [7] D. E. Olivares, A. Mehrizi-Sani, A. H. Etemadi, C. A. Canizares, R. Iravani, M. Kazerani, A. H. Hajimiragha, O. Gomis-Bellmunt, M. Saeedifard, R. Palma-Behnke, G. A. Jimenez-Estevez, and N. D. Hatziargyriou, "Trends in Microgrid Control," *IEEE Transactions on Smart Grid*, vol. 5, no. 4, pp. 1905-1919, 2014.
- [8] J. Bank, B. Mather, J. Keller, and M. Coddington, *High Penetration Photovoltaic Case Study Report*, National Renewable Energy Lab, 2013.
- [9] *A Pathway to the Distributed Grid Solar City: Grid Integration*, 2016.
- [10] B. Mather, *NREL/SCE High-Penetration PV Integration Project: Report o Field Demonstration of Advanced Inverter Functionality in Fontana, CA*, 2014
- [11] Z. Chmiel, and S. C. Bhattacharyya, "Analysis of off-grid electricity system at Isle of Eigg (Scotland): Lessons for developing countries," *Renewable Energy*, vol. 81, pp. 578-588, 9//, 2015.
- [12] I. Mazhari, M. Chamana, B. H. Chowdhury, and B. Parkhideh, "Distributed PV-battery architectures with reconfigurable power conversion units." pp. 691-698.
- [13] N. Kakimoto, H. Satoh, S. Takayama, and K. Nakamura, "Ramp-Rate Control of Photovoltaic Generator With Electric Double-Layer Capacitor," *Energy Conversion, IEEE Transactions on*, vol. 24, no. 2, pp. 465-473, 2009.

- [14] Y. Ruifeng, and T. K. Saha, "Voltage Variation Sensitivity Analysis for Unbalanced Distribution Networks Due to Photovoltaic Power Fluctuations," *Power Systems, IEEE Transactions on*, vol. 27, no. 2, pp. 1078-1089, 2012.
- [15] M. J. E. Alam, K. M. Muttaqi, and D. Sutanto, "A Multi-Mode Control Strategy for VAr Support by Solar PV Inverters in Distribution Networks," *Power Systems, IEEE Transactions on*, vol. 30, no. 3, pp. 1316-1326, 2015.
- [16] A. Samadi, R. Eriksson, So, x, L. der, B. G. Rawn, and J. C. Boemer, "Coordinated Active Power-Dependent Voltage Regulation in Distribution Grids With PV Systems," *Power Delivery, IEEE Transactions on*, vol. 29, no. 3, pp. 1454-1464, 2014.
- [17] Y. Ueda, K. Kurokawa, T. Tanabe, K. Kitamura, and H. Sugihara, "Analysis Results of Output Power Loss Due to the Grid Voltage Rise in Grid-Connected Photovoltaic Power Generation Systems," *Industrial Electronics, IEEE Transactions on*, vol. 55, no. 7, pp. 2744-2751, 2008.
- [18] M. J. E. Alam, K. M. Muttaqi, and D. Sutanto, "A Novel Approach for Ramp-Rate Control of Solar PV Using Energy Storage to Mitigate Output Fluctuations Caused by Cloud Passing," *Energy Conversion, IEEE Transactions on*, vol. 29, no. 2, pp. 507-518, 2014.
- [19] V. Gevorgian, and D. Corbus, *Ramping Performance Analysis of the Kahuku Wind-Energy Battery Storage System*.
- [20] N. Mendis, K. M. Muttaqi, and S. Perera, "Management of Battery-Supercapacitor Hybrid Energy Storage and Synchronous Condenser for Isolated Operation of PMSG Based Variable-Speed Wind Turbine Generating Systems," *Smart Grid, IEEE Transactions on*, vol. 5, no. 2, pp. 944-953, 2014.
- [21] R. Aghatehrani, and R. Kavasseri, "Reactive Power Management of a DFIG Wind System in Microgrids Based on Voltage Sensitivity Analysis," *Sustainable Energy, IEEE Transactions on*, vol. 2, no. 4, pp. 451-458, 2011.
- [22] T. Senjyu, Y. Miyazato, A. Yona, N. Urasaki, and T. Funabashi, "Optimal Distribution Voltage Control and Coordination With Distributed Generation," *Power Delivery, IEEE Transactions on*, vol. 23, no. 2, pp. 1236-1242, 2008.
- [23] S. Toma, T. Senjyu, Y. Miyazato, A. Yona, K. Tanaka, and K. Chul-Hwan, "Decentralized voltage control in distribution system using neural network." pp. 1557-1562.
- [24] F. Marra, Y. Guangya, C. Traeholt, J. Ostergaard, and E. Larsen, "A Decentralized Storage Strategy for Residential Feeders With Photovoltaics," *Smart Grid, IEEE Transactions on*, vol. 5, no. 2, pp. 974-981, 2014.

- [25] M. S. El Moursi, H. H. Zeineldin, J. L. Kirtley, and K. Alobeidli, "A Dynamic Master/Slave Reactive Power-Management Scheme for Smart Grids With Distributed Generation," *Power Delivery, IEEE Transactions on*, vol. 29, no. 3, pp. 1157-1167, 2014.
- [26] N. Yorino, Y. Zoka, M. Watanabe, and T. Kurushima, "An Optimal Autonomous Decentralized Control Method for Voltage Control Devices by Using a Multi-Agent System," *Power Systems, IEEE Transactions on*, vol. 30, no. 5, pp. 2225-2233, 2015.
- [27] S. Alyami, W. Yang, W. Caisheng, Z. Junhui, and Z. Bo, "Adaptive Real Power Capping Method for Fair Overvoltage Regulation of Distribution Networks With High Penetration of PV Systems," *Smart Grid, IEEE Transactions on*, vol. 5, no. 6, pp. 2729-2738, 2014.
- [28] W. H. Kersting, *Distribution System Modeling and Analysis*, 3rd ed.: CRC Press, 2012.
- [29] T. Stetz, F. Marten, and M. Braun, "Improved Low Voltage Grid-Integration of Photovoltaic Systems in Germany," *Sustainable Energy, IEEE Transactions on*, vol. 4, no. 2, pp. 534-542, 2013.
- [30] M. Chamana, F. Jahanbakhsh, B. H. Chowdhury, and B. Parkhideh, "Dynamic ramp rate control for voltage regulation in distribution systems with high penetration photovoltaic power generations." pp. 1-5.
- [31] W. Guishi, M. Ciobotaru, and V. G. Agelidis, "Power Smoothing of Large Solar PV Plant Using Hybrid Energy Storage," *Sustainable Energy, IEEE Transactions on*, vol. 5, no. 3, pp. 834-842, 2014.
- [32] Z. Zhixue, W. Xiaoyu, and L. Yongdong, "A control method for grid-friendly photovoltaic systems with hybrid energy storage units." pp. 1437-1440.
- [33] L. Xiaohu, A. Aichhorn, L. Liming, and L. Hui, "Coordinated Control of Distributed Energy Storage System With Tap Changer Transformers for Voltage Rise Mitigation Under High Photovoltaic Penetration," *Smart Grid, IEEE Transactions on*, vol. 3, no. 2, pp. 897-906, 2012.
- [34] M. M. A. Abdelaziz, M. F. Shaaban, H. E. Farag, and E. F. El-Saadany, "A Multistage Centralized Control Scheme for Islanded Microgrids With PEVs," *Sustainable Energy, IEEE Transactions on*, vol. 5, no. 3, pp. 927-937, 2014.
- [35] H. E. Z. Farag, and E. F. El-Saadany, "A Novel Cooperative Protocol for Distributed Voltage Control in Active Distribution Systems," *Power Systems, IEEE Transactions on*, vol. 28, no. 2, pp. 1645-1656, 2013.

- [36] J. Barr, and R. Majumder, "Integration of Distributed Generation in the Volt/VAR Management System for Active Distribution Networks," *Smart Grid, IEEE Transactions on*, vol. 6, no. 2, pp. 576-586, 2015.
- [37] P. N. Vovos, A. E. Kiprakis, A. R. Wallace, and G. P. Harrison, "Centralized and Distributed Voltage Control: Impact on Distributed Generation Penetration," *Power Systems, IEEE Transactions on*, vol. 22, no. 1, pp. 476-483, 2007.
- [38] Y. Li, D. Czarkowski, and F. de Leon, "Optimal Distributed Voltage Regulation for Secondary Networks With DGs," *Smart Grid, IEEE Transactions on*, vol. 3, no. 2, pp. 959-967, 2012.
- [39] Y. P. Agalgaonkar, B. C. Pal, and R. A. Jabr, "Distribution Voltage Control Considering the Impact of PV Generation on Tap Changers and Autonomous Regulators," *Power Systems, IEEE Transactions on*, vol. 29, no. 1, pp. 182-192, 2014.
- [40] F. A. Viawan, and D. Karlsson, "Voltage and Reactive Power Control in Systems With Synchronous Machine-Based Distributed Generation," *Power Delivery, IEEE Transactions on*, vol. 23, no. 2, pp. 1079-1087, 2008.
- [41] N. Daratha, B. Das, and J. Sharma, "Coordination Between OLTC and SVC for Voltage Regulation in Unbalanced Distribution System Distributed Generation," *Power Systems, IEEE Transactions on*, vol. 29, no. 1, pp. 289-299, 2014.
- [42] K. M. Rogers, R. Klump, H. Khurana, and T. J. Overbye, "Smart-Grid -enabled load and distributed generation as a reactive resource." pp. 1-8.
- [43] S. Deshmukh, B. Natarajan, and A. Pahwa, "Voltage/VAR Control in Distribution Networks via Reactive Power Injection Through Distributed Generators," *Smart Grid, IEEE Transactions on*, vol. 3, no. 3, pp. 1226-1234, 2012.
- [44] F. Capitanescu, I. Bilibin, and E. Romero Ramos, "A Comprehensive Centralized Approach for Voltage Constraints Management in Active Distribution Grid," *Power Systems, IEEE Transactions on*, vol. 29, no. 2, pp. 933-942, 2014.
- [45] M. A. Azzouz, M. F. Shaaban, and E. F. El-Saadany, "Real-Time Optimal Voltage Regulation for Distribution Networks Incorporating High Penetration of PEVs," *Power Systems, IEEE Transactions on*, vol. 30, no. 6, pp. 3234-3245, 2015.
- [46] S. Xiangjing, M. A. S. Masoum, and P. J. Wolfs, "Optimal PV Inverter Reactive Power Control and Real Power Curtailment to Improve Performance of Unbalanced Four-Wire LV Distribution Networks," *Sustainable Energy, IEEE Transactions on*, vol. 5, no. 3, pp. 967-977, 2014.

- [47] J. H. Harlow, "Step-Voltage Regulators," *Electric Power Transformer Engineering*, pp. 8-23, Boca Raton: CRC Press 2012.
- [48] *PV Grid Integration - SMA Solar Technology AG*, 2012.
- [49] A. Wächter, and L. T. Biegler, "On the implementation of a primal dual interior point filter line search algorithm for large-scale nonlinear programming," *Math. Progr.*, vol. 106, no. 1, pp. 25-27, Apr. 2006.
- [50] P. R. Amestoy, A. Guermouche, J.-Y. L'Excellent, and S. Pralet, "Hybrid scheduling for the parallel solution of linear syst," *Parallel Computing*, vol. 32, no. 2, pp. 136-156, 2006.
- [51] J. Currie, and D. I. Wilson, *OPTI: Lowering the Barrier Between Open Source Optimizers and the Industrial MATLAB User*, Georgia, USA, 2012.
- [52] R. Bhatt, and B. Chowdhury, "Grid frequency and voltage support using PV systems with energy storage." pp. 1-6.
- [53] W. A. Omran, M. Kazerani, and M. M. A. Salama, "Investigation of Methods for Reduction of Power Fluctuations Generated From Large Grid-Connected Photovoltaic Systems," *Energy Conversion, IEEE Transactions on*, vol. 26, no. 1, pp. 318-327, 2011.
- [54] D. Velasco de la Fuente, Rodri, x, C. L. T. guez, Garcera, x, G., E. Figueres, and R. O. Gonzalez, "Photovoltaic Power System With Battery Backup With Grid-Connection and Islanded Operation Capabilities," *Industrial Electronics, IEEE Transactions on*, vol. 60, no. 4, pp. 1571-1581, 2013.
- [55] K. T. Tan, P. L. So, Y. C. Chu, and M. Z. Q. Chen, "Coordinated Control and Energy Management of Distributed Generation Inverters in a Microgrid," *Power Delivery, IEEE Transactions on*, vol. 28, no. 2, pp. 704-713, 2013.
- [56] S. Kai, Z. Li, X. Yan, and J. M. Guerrero, "A Distributed Control Strategy Based on DC Bus Signaling for Modular Photovoltaic Generation Systems With Battery Energy Storage," *Power Electronics, IEEE Transactions on*, vol. 26, no. 10, pp. 3032-3045, 2011.
- [57] M. B. Delghavi, and A. Yazdani, "A Unified Control Strategy for Electronically Interfaced Distributed Energy Resources," *Power Delivery, IEEE Transactions on*, vol. 27, no. 2, pp. 803-812, 2012.
- [58] G. Delille, B. Francois, and G. Malarange, "Dynamic Frequency Control Support by Energy Storage to Reduce the Impact of Wind and Solar Generation on Isolated Power System's Inertia," *Sustainable Energy, IEEE Transactions on*, vol. 3, no. 4, pp. 931-939, 2012.

- [59] Y. Xiaoyan, and L. M. Tolbert, "Ancillary services provided from DER with power electronics interface." p. 8 pp.
- [60] J. D. Kueck, B. J. Kirby, L. M. Tolbert, and D. T. Rzy, "Voltage Regulation-Tapping Distributed Energy Resources," *Fortnightly*, 2004.
- [61] C. A. Hill, M. C. Such, C. Dongmei, J. Gonzalez, and W. M. Grady, "Battery Energy Storage for Enabling Integration of Distributed Solar Power Generation," *Smart Grid, IEEE Transactions on*, vol. 3, no. 2, pp. 850-857, 2012.
- [62] M. Bragard, N. Soltan, R. W. De Doncker, and A. Schmiegel, "Design and implementation of a 5 kW photovoltaic system with li-ion battery and additional DC-DC converter." pp. 2944-2949.
- [63] S. Wenbo, X. Xiaorong, C. Chi-Cheng, and R. Gadh, "Distributed Optimal Energy Management in Microgrids," *Smart Grid, IEEE Transactions on*, vol. 6, no. 3, pp. 1137-1146, 2015.
- [64] S. A. Pourmousavi, M. H. Nehrir, and R. K. Sharma, "Multi-Timescale Power Management for Islanded Microgrids Including Storage and Demand Response," *Smart Grid, IEEE Transactions on*, vol. 6, no. 3, pp. 1185-1195, 2015.
- [65] E. Barklund, N. Pogaku, M. Prodanovic, C. Hernandez-Aramburo, and T. C. Green, "Energy Management in Autonomous Microgrid Using Stability-Constrained Droop Control of Inverters," *Power Electronics, IEEE Transactions on*, vol. 23, no. 5, pp. 2346-2352, 2008.
- [66] P. H. Divshali, S. H. Hosseinian, and M. Abedi, "A novel multi-stage fuel cost minimization in a VSC-based microgrid considering stability, frequency, and voltage constraints," *Power Systems, IEEE Transactions on*, vol. 28, no. 2, pp. 931-939, 2013.
- [67] A. G. Tsikalakis, and N. D. Hatziargyriou, "Centralized Control for Optimizing Microgrids Operation," *Energy Conversion, IEEE Transactions on*, vol. 23, no. 1, pp. 241-248, 2008.
- [68] T. Sicong, X. Jian-Xin, and S. K. Panda, "Optimization of Distribution Network Incorporating Distributed Generators: An Integrated Approach," *Power Systems, IEEE Transactions on*, vol. 28, no. 3, pp. 2421-2432, 2013.
- [69] A. K. Basu, A. Bhattacharya, S. Chowdhury, and S. P. Chowdhury, "Planned Scheduling for Economic Power Sharing in a CHP-Based Micro-Grid," *Power Systems, IEEE Transactions on*, vol. 27, no. 1, pp. 30-38, 2012.
- [70] W. Xiong, W. Xiuli, and Q. Chong, "A Hierarchical Framework for Generation Scheduling of Microgrids," *Power Delivery, IEEE Transactions on*, vol. 29, no. 6, pp. 2448-2457, 2014.

- [71] T. L. Vandoorn, B. Meersman, J. D. M. D. Kooning, and L. Vandeveldel, "Directly-Coupled Synchronous Generators With Converter Behavior in Islanded Microgrids," *IEEE Transactions on Power Systems*, vol. 27, no. 3, pp. 1395-1406, 2012.
- [72] A. A. Eajal, M. F. Shaaban, K. Ponnambalam, and E. F. El-Saadany, "Stochastic Centralized Dispatch Scheme for AC/DC Hybrid Smart Distribution Systems," *IEEE Transactions on Sustainable Energy*, vol. 7, no. 3, pp. 1046-1059, 2016.
- [73] M. Bayat, K. Sheshyekani, M. Hamzeh, and A. Rezazadeh, "Coordination of Distributed Energy Resources and Demand Response for Voltage and Frequency Support of MV Microgrids," *IEEE Transactions on Power Systems*, vol. 31, no. 2, pp. 1506-1516, 2016.
- [74] M. E. Baran, and F. F. Wu, "Network reconfiguration in distribution systems for loss reduction and load balancing," *Power Delivery, IEEE Transactions on*, vol. 4, no. 2, pp. 1401-1407, 1989.